Technische Universität München

Institut für Nanoelektronik

Hybrid Organic/Inorganic Optical Sensors

Armin Theodor Exner

Vollständiger Abdruck der von der Fakultät für Elektrotechnik und Informationstechnik der Technischen Universität München zur Erlangung des akademischen Grades eines
Doktors Ingenieurs
genehmigten Dissertation.

Vorsitzende(r):	Univ.-Prof. Dr.-Ing. habil. Dr. h.c. Alexander W. Koch
Prüfer der Dissertation:	
	1. Univ.-Prof. Paolo Lugli, Ph.D.
	2. Univ.-Prof. Dr. Bettina V. Lotsch, Ludwig-Maximilians-Universität München

Die Dissertation wurde am 01.10.2013 bei der Technischen Universität München eingereicht und durch die Fakultät für Elektrotechnik und Informationstechnik am 12.02.2014 angenommen.

Abstract

The response of a photonic crystal (PC) to heat and chemical exposure opens a promising field of a new sensing principle. These new sensors use the photonic changes of the PC, to sense the presence of an analyte or heat. For computer aided processing, the optical response has to be translated into an electric current, which raises the demand of an opto-electric translation platform that is scalable and cheap in production.

In this thesis, the gap between optical response and electric readout is closed by employing an organic light emitting diode (OLED) as a light source and a common light detector to determine the optical properties of a PC. The OLED, build from the PDY-132 (Merck) polymer, was characterized in the response to heat under different driving conditions. The sensitivity of the porous PCs, which where made of SiO_2 and TiO_2, was demonstrated with respect to moisture, ethanol vapor and temperature. The light source and the PC have been assembled, for the detection of infrared (IR) radiation and a charge-coupled device (CCD) camera has been used to record the IR picture. A platform the opto-electric translation of the PC for the chemical detection has been created using an OLED and an organic photodetector.

The thermo-optic response of the OLED and the PC has been found to be $1.5\,\mathrm{cd\,m^{-2}}$ for the OLED alone and $3.8\,\mathrm{cd\,m^{-2}}$ for both, the OLED together with the PC. The IR imaging has been demonstrated with the proposed setup on a 1.5 $\times$ $1.5\,\mathrm{cm^2}$ wide chip on different IR pattern. The chemical detection was demonstrated showing a response time of approximately 2 s and detection limit of 10 parts per million (ppm) for ethanol in nitrogen at room temperature.

Contents

1 Introduction

The investigation of versatile sensing principles broadens the field of application, for sensors and for all digital devices requiring an interaction with the physical world. A sensor converts a physical quantity into a signal that can either be sensed by humans or can be processed using modern data processing techniques. The conversion to a signal of human recognition extends the perception abilities to physical signals that are "invisible" and small quantities that could not be recognized otherwise. A sensor which converts the physical quantity into an electrical signal, that can be processed using computer technologies, enables an innumerable amount of applications, as it is the essential interface between the "real" world and the digital world.
One of these interfaces is the temperature detection, which can be measured contact free. Remote temperature measurement has in the past been restricted to expensive infrared (IR) cameras using microbolometer arrays or photo-electric low band-gap sensors. The very high price of IR cameras, more than 23.000 Euros for a camera with a resolution of 640 × 480 pixels (FLIR T-620), excludes the use to very few cost insensitive applications. However, a huge number of possible applications is waiting for affordable IR sensors, for instance as an on-line temperature tracker of technical components, or as an intelligent IR motion sensors which can distinguish between animals and human beings. In this thesis we follow up a promising approach towards the fabrication of low-cost IR detectors which employ the concept of thermo-optic imaging. Thermo-optic IR detectors promise to be less difficult to construct than bolometer arrays and do not require cryogenic cooling as do photo-electric detectors. The integration of thermo-optic detectors with cameras working in the visible light region promises lower development and fabrication costs.
We present the development of sensors based on tunable photonic crystals (PCs) which are responsive to external stimuli by either (i) local heat changes, or alternatively, (ii) ad- and desorption of molecules. The detection of (i) local heat changes

on a plane can be utilized for an innovative detection principle for IR radiation. The IR signal is converted either to an optical signal which can be seen by the bare eye or recorded by a camera for later processing.
The major goal of this thesis is the assembly and demonstration of the proposed IR sensing principle and gather a basis of information to assist in research and optimization of the sensor.
A quite different field of application features (ii) the detection of molecules either in gas phase or liquids by adsorption of the analyte into a porous PC structure. The adsorption alters the optical properties which changes the color of the PC. The color change of the PC is translated into an electrical current by measuring the transmission of an organic light emitting diode (OLED) light with a photodetector. Research has been done at the Institute for Nanoelectronics. Investigations on tunable optical filters for the proposed application of IR sensing have been carried out by Piedro Regoliosi who investigated the thermal tunability of a photonic microcavity between two Bragg mirrors [Reg08]. A patent has been assigned on the proposed IR sensor and the fabrication technique [Sca08].

This Project was carried out in cooperation with the *Department Chemie und Pharmazie* with Prof. Bettina V. Lotsch at the *Ludwigs-Maximilians-Universität München (LMU)*. Responsible for the fabricaton of PCs was Markus Guehl from april 2010 to october 2010. From October 2010 on, Ida Pavlichenko was responsible for the fabrication of the PCs. The organic photodetectors (OPDs) that have been used where fabricated in house, at the institute by Daniela Baierl. A Bachelor thesis on the fabrication and characterization of OLEDs has been written by Stefan Menacher at the institute.

In Chapter 1 a general introduction and motivation to the proposed sensor concept is given. Previous work and cooperation partners are introduced.
Chapter 2 gives a general overview over the field of study. Each component, as well as the assembled devices, are described in their principle of operation, a theoretical background and presentation of the state of the art is given in this chapter. A fundamental explanation of the two proposed sensors is given in the end of this chapter as well.

The experimental setups and fabrication methods are presented in Chapter 3 chapter. If not stated differently, the experiments have been conducted as stated in this chapter. Standard calculation methods are introduced.

In the following chapter the investion of the single components is presented. Section 4.1 presents a detailed characterization and optimization of the OLED. Different electrode materials for the anode, as well as for the cathode, have been tested in order to find the best suited setup for the proposed sensor. The degradation phenomena are investigated and improved by different encapsulation methods. Two different colors of OLED polymers have been investigated, namely the yellow emitting PDY-132 and the blue emitting SPB-02T and their suitability for the proposed IR sensor is analyzed. The thermal tuning of the OLED fabricated from PDY-132 is investigated in detail, which delivers important knowledge for a good design of an IR detector based on the integration of an OLED and a PC.

In Section 4.2 we present a comprehensive study of porous 1-dimensional photonic crystals (1DPCs) consisting of thin films of TiO_2 and SiO_2. The porosity and its effect to the tunability is discussed and three different grades of porosity are presented: i) porosity from nano-particle voids, ii) macroscopic porosity from precursors and iii) dense films without significant porosity. The fabrication via solution processed spin-coating and sputtered PCs are presented and compared in therms of their thermal tunability and ad- and desorption behavior of analytes. The response speed has been measured and the stop-band shift has been successfully simulated. Single layer characterization gives insight into the kinetics and the diffusion characteristics of porous PCs.

In Section 4.3 the OPD on the basis of the photo-active polymers P3HT/PCBM is presented. The performance of the OPD has been measured under different temperature conditions. The gained insight into the conductivity behavior at different temperatures of the photo-active polymer is of great importance for the understanding and prediction of the two proposed integrated sensors, the electro-photonic sensing platform and the IR sensor. Conclusions and limitations for the application in an IR sensor are obtained in this section.

In Chapter 5 the two different hybrid sensing concepts are introduced. In Section 5.1 the previously discussed OLED and the PC are joint on a single glass substrate on opposing sites and the IR sensitivity is demonstrated. Our quantitative analysis of

the IR sensor shows that the contribution of both elements, the OLED and the PC, constructively cooperate, as it was predicted by the respective study of the components alone. We demonstrate the visualization of a heat gradient in a $3 \times 3\,\mathrm{mm}^2$ sensor using a microscope camera where the hot areas are brighter than the cold areas. Finally we present an IR image, obtained by the projection of an IR pattern onto a $15 \times 15\,\mathrm{mm}^2$ sensor, using an IR lamp as a beam source and a shadow mask to pattern the IR beam. Limitations of the current sensor design are discussed and improvements of the sensor speed, sensitivity, and resolution are addressed.
Section 5.2 is dedicated to the chemical sensor platform that allows the optical response measurement to a chemical analyte of different PCs using an OLED as light source and an OPD as a detector in a miniaturized setup. Ethanol concentrations of 10 parts per million (ppm) in nitrogen have been measured which corresponds to a stop-band shift of 10 ppm. This resolution exceeds the capabilities of our spectrometer while at the same time it is less expensive and less power consuming, which enables the setup for various applications. We present the study of the devices sensitivity, response speed and stop-band shift.
The last chapter concludes the major achievements and a résumé on the knowledge that can be abstracted. We identify upcoming challenges and an outlook is presented.
A general overview on the thesis is shown graphical in Figure 1.1.

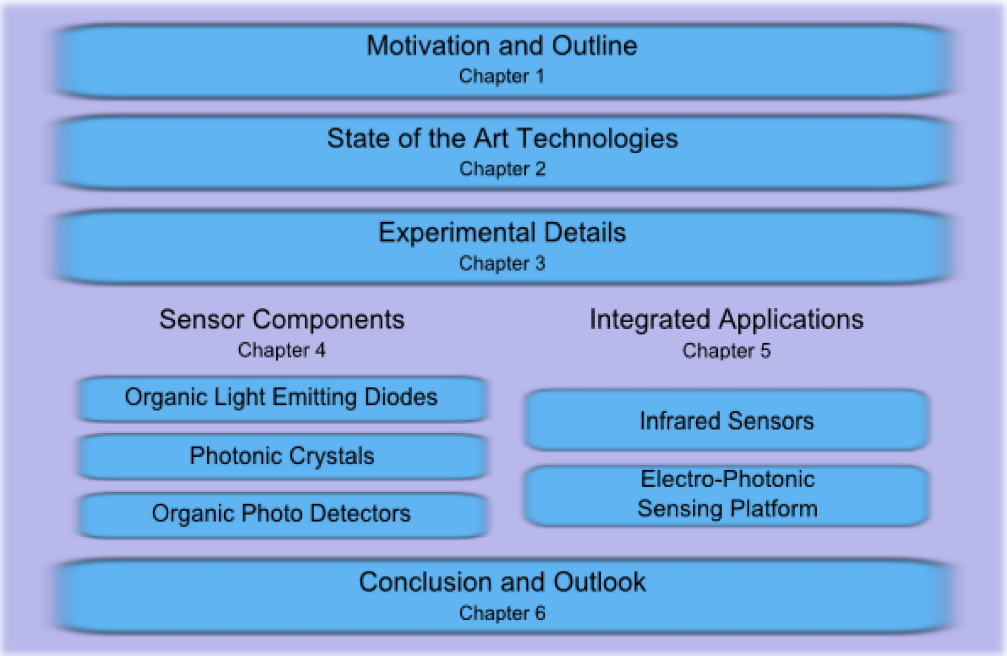

Figure 1.1: Graphical overview of the thesis.

2 State of the Art Technologies

This chapter provides a general overview of the technologies that have been utilized in this thesis. Each single component of the proposed sensor is discussed in the corresponding section, OLED 2.1, PC 2.2 and OPD 2.3. The theoretical background and the principle of operation of the IR sensor in Section 2.4 and for the chemical sensing platform in Section 2.5.

2.1 Organic Light Emitting Diode

In this thesis a new field of OLED application, as a component in a multifunctional sensing platform on the basis of a PC, is discovered. We explain the working principle and introduce the state of the art technologies, together with numerous applications in order to demonstrate the versatility of the OLED and the suitability for this particular project. The results of experimental work with OLEDs is collected in the experimental part, Section 4.1.

The first organic electroluminescence (EL) cell dates back to 1953 where A. Bernanose presented an AC driven anthracene cell showing EL at a voltage of 2000 V and a cell thickness of 100 to 200 µm [Ber55]. Almost one decade later in 1963 Pope et al. came up with the first DC driven EL organic crystals at a voltage of 400 V [Pop63]. From this time on, the fascination for EL devices grew continuously with the knowledge that was discovered. Their inherent small size, weight and thickness was ever since their first demonstration, a key feature for many potential applications. Nevertheless many years passed until several issues, such as the driving voltage, efficiency, stability and fabrication issues where solved in order to compete with actual technologies [Bao99, Dod97]. OLEDs made a steady progress to high resolution color displays with the best technical performance in display tech-

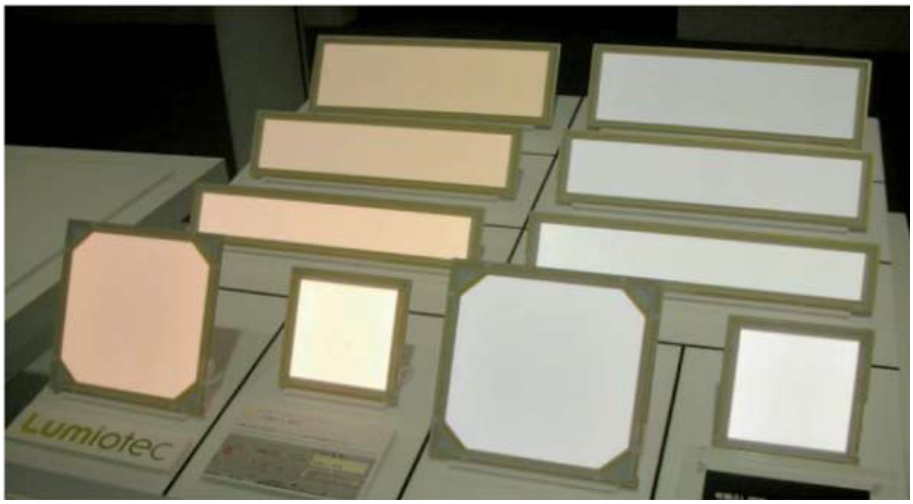

Figure 2.1: White emitting OLED panels commercially available from Lumiotec (©2012, Lumiotec, http://www.lumiotec.com).

nology. The thin devices, that can be fabricated on bendable plastic substrates, are suitable for flexible displays [Zho06]. Now, as OLEDs also employ multi-emission layer techniques and white emitting diodes can be fabricated, a huge field of lighting applications opens up [Shi03, p.18]. White emitting diodes typically comprise three layers, emitting red, green and blue light. The colors are mixed according to Grassmann's law and the impression of white light appears. The good energy efficiency, low fabrication costs and long lifetime up to 10^5 hours promises to globally reduce lighting costs and CO_2 emissions [Hum08]. The OLED efficiency recently exceeded the performance of fluorescent tubes, with phosphorescent polymer at an efficiency of 102.7 lm W^{-1}, at a luminous intensity of 1000 cd m^2 and is expected to rise further [Sas13, Han12]. A recent publication about high light output of more than 10 000 cd m^{-2} by Mulani et al. promises the improvement of important performance parameters for display technology, as well as for solid state lightning [Mul13]. Research interests also include nanoscale OLEDs, as they are the smallest light emitting devices known, reported already in 2005 by Yamamoto et al. demonstrating an MEH-PPV based OLED with a diameter of only 60 nm at a power consumption as low as 144 pW [Yam05].

The difference between an LED and an OLED lies in the materials that are used. The LED is build using inorganic direct band-gap materials, whereas the OLED is

build from semi-conducting polymer materials. The advantages of the OLED can mainly be found in the fabrication procedures that these materials require. Conventional LEDs are grown by complex chemical vapor deposition (CVD) processes on exotic waver materials. Besides the fact that these fabrication methods are more expensive than the OLED fabrication, which will be described in detail further below, the requirements to the substrate materials are pretty strict. Free choice of substrate material is very important for the proposed sensors, as it might be necessary to use an IR transparent material, or to employ flexible or thin film materials. The potential of fully solution processability renders the OLED ideal for our propose sensing devices [Zho11]. When considering the light out-coupling efficiency, the OLED bears one inherent advantage: the low refractive index (RI) of the active material minimizes interface reflections and decreases the angle of total reflection, which would prevent the generated photon from escaping the device.

An overview on OLEDs technologies, including historical and theoretical aspects in detail, can be found in "Organic Light-Emitting Devices" by Joseph Shinar [Shi03]. The book also delivers information about novel OLED concepts such as white emitting, multilayer and small molecule OLEDs. Furthermore, the book "Organic Light-Emitting Devices" by Klaus Müllen and Ullrich Scherf covers the field, with the addition of hybrid devices and dendrimer polymers [Mue06].

2.1.1 Working Principle

In a most general way, the working principle of an OLED is a recombination of charge-carriers from an exited state under emission of a photon. Charge-carriers are injected into a photo-active material, electrons from the cathode and holes from the anode. As the conductivity of the conductive polymer is rather low, vertical device structures, where the layer thickness can precisely controlled to be in the range of 100 nm, are desired. The basic structure is depicted in Figure 2.2, which indicates the required layers. The emission layer is located between the two electrodes, where the anode is transparent for light out-coupling. In the following section, each layer of the OLED is introduced along with an overview about the employed materials.

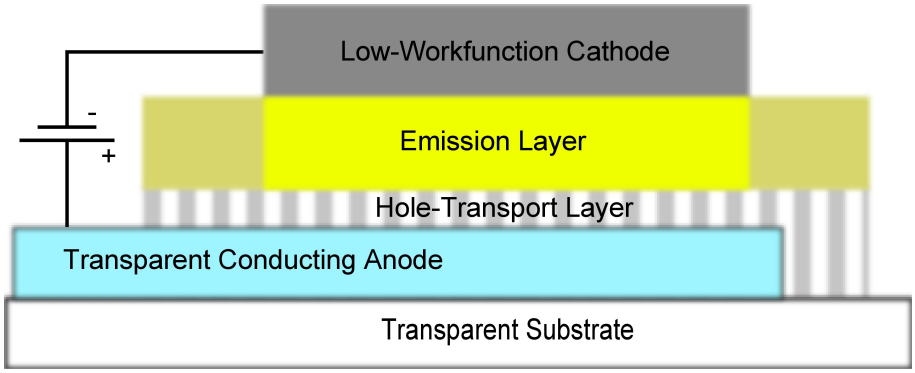

Figure 2.2: Basic structure of the OLED comprising one emission layer

2.1.2 Materials

This Section introduces state-of-the-art materials, which are used to build nowadays OLEDs as depicted in Figure 2.2.

The Substrate

The substrate of the OLED has the two mayor functions to protect the thin and fragile OLED and at the same time allowing the light out-coupling which requires the substrate to be transparent. Additional requirements can be the shielding of harmful radiation, such as ultra-violet (UV) light and the protection from aggressive atmospheric content, such as oxygen. Glass delivers the best performance for OLEDs, because of the low roughness, hardness, good diffusion barrier and simple handling during fabrication. Plastic substrates exhibit novel features such as flexibility and fabrication on ultra-thin foils. Additionally, plastic bears the inherent advantage of a lower RI and thus less reflection at the interface to the atmosphere and, in case of a polymer electrode, the good matching with the OLED polymer which provides an almost lossless interface to the polymer.

The Anode

The transparent anode can be made of either (i) indium-tin-oxide (ITO) [Ngu03], (ii) of the solution processable polymer poly(3,4-ethylenedioxythiophene) (PEDOT) [Lop08] or (iii) of a transparent graphene based electrode [Agu06]. Important anode parameters are: the transparency, electrical resistance, and the chemical stability.

The transparency consists of an absorption component which depends on the absorption coefficient and thickness of the film and a reflective component which is determined by the RI contrast to the neighboring layers. The electrical resistance for thin films is typically given as the sheet resistance in ohm per square [$\Omega\square^{-1}$]. The sheet resistance is a measure of resistance in a 2 dimensional thin film for the current flowing in plane. To accurately measure the sheet resistance without the out of plan resistance and contact resistance a four point probe is typically used, where the distance between the electrodes is much higher than the film thickness.

(i) ITO The most common material is nowadays ITO, which is commercially available for more than a decade. The low roughness and the low resistance of down to $15\,\Omega\square^{-1}$ for commercially available films at a transparancy of approximately 85% renders it suitable as a transparent anode [Kim99]. However, ITO electrodes have two mayor drawbacks: 1) ITO is too brittle to be used on flexible substrates, only a few bending events would brake the electrode and prohibit the conduction and 2) it has been shown that ITO degrades by electro-migration of indium which in turn diffuses through the device degrades the OLED polymer [Lee99].

(ii) PEDOT An upcoming alternative to ITO anodes are thin polymer films of highly conductive PEDOT:PSS which is a blend of PEDOT and poly(styrene sulfonate) (PSS). The material is soluble in water and features an excellent solution processability, since it is absolute indissoluble in any organic solvent the subsequent deposition of dissolved polymers is possible. PEDOT electrodes can be coated via any solution processing technique such as spin-coating and spray coating on any substrate material and does not necessarily require any temperature treatment. The room-temperature fabrication renders it also an ideal candidate for inverted structures, since the layer can be deposited on top of an organic layer. However, the fabrication of PEDOT:PSS films on top of organic layers requires a hydrophilic surface, typically achieved by a short oxygen-plasma treatment [Bai11a]. Highly conductive PEDOT:PSS is commercially available i.e. under the brand name *PH1000* by Clevios™, obtaining sheet resistance values down to $100\,\Omega\square^{-1}$ at a thickness of 100 nm [Cle13]. Recently published results by Alemu et al. demonstrate even a con-

ductivity of 25 $\Omega\square^{-1}$ at a transmittance of 85% after applying a methanol treatment, which makes PEDOT:PSS electrodes fairly compatible with ITO electrodes [Ale12]. For OLEDs with a very high power consumption further enhancement of the anode conductivity might be required, an innovative concept has been demonstrated by Choi et al. by introducing metal grid fingers under the PEDOT layer [Cho11]. The main advantage of the PEDOT electrode with respect to flexible OLEDs, is its good bending performance. Additionally, the chemical stability of PEDOT:PSS is far better than the ITO stability and causes less device degradation.

(iii) Graphene Based Materials The use of graphene based materials fabricated from a single layer of carbon atoms aligned in a periodic lattice have the stunning characteristics that electrons move nearly unimpeded through the two-dimensional material. Its discovery was awarded with the Nobel Prize in Physics to Andre Geim and Kostya Novoselov in 2010. The high electron mobility renders them a good candidate for an extreme well conducting electrode, while due to only one layer of carbon atoms maintaining a high transparency [Wu10]. The fabrication of OLEDs on graphene electrodes was recently reported by Han et al. showing a record luminous efficiency of more than 100 lm W^{-1} [Han12]. The closely related carbon nano-tubes, in principle, rolled up graphene sheets, have been demonstrated as OLED electrodes [Hu10, Chi10].

Hole Transport Layer

The hole transport and injection layer is an important layer for the tuning of the hole – electron balance. It typically also improves the band matching between the OLED and the anode material. It introduces a hole barrier which confines the holes for a locally controlled recombination in the active layer as graphically demonstrated in Figure 2.4. The most common hole transport layer (HTL) material is PEDOT:PSS which can be purchased for solution processing in an aqueous solution with a blend ratio PEDOT:PSS of 1:6 (by weight) as can be obtained from the data sheet of *P VP AI 4083* by Clevios™. The film thickness tunes the hole injection and the conductivity of the device, the films are applied with a typical thickness of 20 nm.

OLED Polymers

The OLED polymer is the emitting material in the device. Its responsibility is the efficient recombination of electron-hole pairs and the out-coupling of the generated photon. OLED polymers can be subdivided in three groups, (i) small molecules, (ii) conjugated polymers and (iii) dendrimer polymers.

(i) Small Molecules Small molecules are typically defined by their low molecular weight of less than $800\,\mathrm{g\,mol^{-1}}$ which usually comes with a bad solubility in all solvents. Thin-film fabrication of small molecules can be realized by thermal physical vapor deposition (PVD) in ultra high vacuum with a precise control of the temperature in order to meet the point where the molecules evaporate already, but do not break or degrade by the high temperature. Alternatively, small molecules can be deposited from the organic vapor phase (OVPD), also in vacuum. The big advantage that comes with the named two deposition methods is the almost unconstrained number of layers, that can be grown on the substrate, i.e. injection and blocking layers, which contributes to the efficiency. Multiple-layer systems can involve several light emitting layers, emitting different colors and, with a good combination, appearing as white light. The lack of solution processability makes the fabrication rather expensive, since vacuum equipment is required, which generally also implies strict size limitations. However, small molecules are currently the leading technology for display applications, due to their long lifetime and color constancy combined with a good resistance against oxygen and water. Small molecule devices exhibit extremely high brightnesses, values up to $95\,800\,\mathrm{cd\ m^{-2}}$ and a maximum efficiency of $46\,\mathrm{lm\ W^{-1}}$ have been reported [Wan11].

(ii) Conjugated Polymers In principle, a conjugated polymer is a chain of carbon atoms with overlapping molecular electron-orbitals, known as π-electron bonding, which is responsible for the conductivity of the molecule. A comprehensive study of EL in conjugated polymers has been published more than 10 years ago by Friend et al. reviewing the research activities in the filed [Fri99]. The chains of the molecule can be very long, which also include soluble groups, so that the polymer can be dissolved in organic solvents. The solution processability comes with many advantages

and possibly low costs – large area production like spray coating and ink-jet printing [Abd12]. The solution processability bears another crucial advantage, namely the possibility to blend several polymers, in order to produce new composites and improve the performance of opto-electronic polymer devices [Moo02]. The inherent problem that comes along with the solution processing is the challenge to fabricate a stack of several emission layers i.e. for color tuning. A number of possibilities have been exploited, namely: i) the use of orthogonal solvents as it is done for the deposition of the PEDOT, which serves as a hole injection layer, ii) changing the solubility by thermal curing [Bur90] and iii) the use of chemical precursors which can be polymerized after deposition [Jia00]. The general trend and most promising approach for efficient, stable and cheap devices are the group of dendrimer polymers, which are a logical combination of soluble conjugated polymers and the advantages of small molecule OLEDs.

(iii) Dendrimer Polymers [from ancient Greek: *Dendron* - the tree] Dendrimer polymers are macromolecular molecules with a branching geometry, which is radially growing from the core, as depicted in Figure 2.3. The main advantage is that the core molecule can be separated from the environment using functional branches for instance to take an indissoluble molecule and attach some functional polymer chains to make it soluble in the desired solvent. This innovative concept leads to the fusion of the well developed small molecule OLEDs with the cheaper and faster solution processable conjugated polymers technology, since the required functional groups are attached to the molecule [Li09]. Additionally, the separation of the functional core and the solubility allows an individual optimization of the light emitting core, in order to i.e. tune the emission spectrum of the OLED [Hal99]. The exceptional tree like geometry bears a major advantage: as injected charge-carriers must cross the center molecule, if they travel to the other side of the dendrimer, that leads to an unique confinement of electrons and holes at the functional group in the center of the molecule [Mue06, p.266].

One thing these three polymers do have in common is the conduction mechanism of charge-carriers via π-orbitals and delocalized electrons as discussed in Section 2.1.3. All these polymers are more or less sensitive to impurities, first during processing but also in the ready build device, which causes degradation of the polymer,

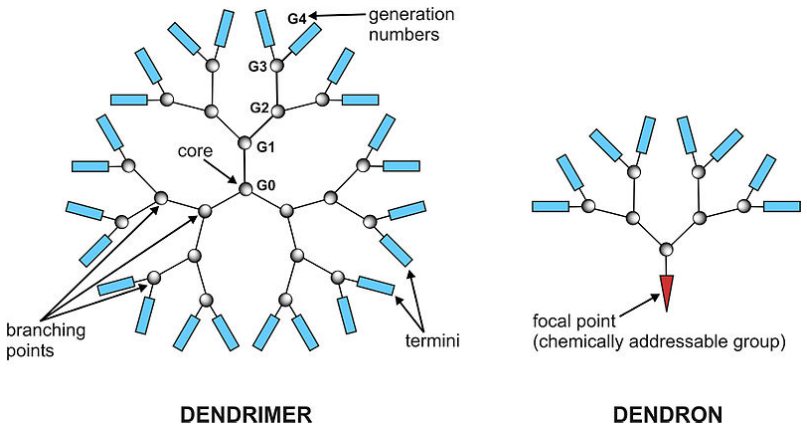

Figure 2.3: Dendimer and Dendron molecule. The tree like structure forces electrons to pass through the molecular core. Picture - [Wik13b]

decrease of the conductivity and light efficiency. The biggest threats are oxygen and water, which can harm the polymer directly, i.e. by breaking the conductive chains, but can also lead to a decomposition of the ITO anode or metal cathode, and indirectly harm the device and lower the performance [Lee99].

The Cathode

The OLEDs cathode has two major tasks: the efficient conduction of electrons for homogenous distribution over the whole device and the injection of electrons in the LUMO of the active polymer. Best conductance, mechanical and chemical stability is typically provided by noble metals such as gold (Au) and silver (Ag). For OLEDs the most common material is Ag since it is much more cost efficient compared to Au. The second task of the cathode is the electron injection, which requires a low work function metal, such as calcium (Ca), magnesium (Mg) or Barium (Ba). As these metals are too brittle and unstable to work as an electrode alone, therefore a second conducting layer is applied on top for stabilization and conduction. The films can easily be evaporated via physical-vapor-deposition (PVD). Care, however, must be taken when selecting the materials, as corrosion and gas evolution of the metals has shown to harm the active material and gas evolution delaminates the cathode layer and form non-emitting spots [Azi98].

Encapsulation

In principle, OLED can operate at ambient air atmosphere for some minutes. However, if one desires lifetimes towards the above mentioned 10^5 hours, the encapsulation becomes a crucial aspect. The encapsulation protects the polymer and the electrodes from ambient water, oxygen and mechanical stress. A common encapsulation technique is to glue a glass plate on top of the OLED structure. The glue that is used typically an UV-curing epoxy or a two component glue. More advanced encapsulation methods are based on a glass plate with a cave on the inside, where getter materials can be deposited. Getter materials aim at the binding of oxygen and water before they diffuse into the OLED. Current trends are ultra-thin barrier films for the encapsulation of large area displays, including flexible – bendable – encapsulation for flexible devices.

2.1.3 Chrage Carrier Dynamics in Conductive Polymers

The discovery of electrical conduction in polymer films in the late 1950s triggered the field of organic electronics. For their work on conductive polymers Alan J. Heeger, Alan G. MacDiarmid and Hideki Shirakawa received the Nobel price of chemistry in 2000. The topic has been intensively investigated starting in the 70s [Pfi77] reaching to nowadays knowledge as it is documented by, among others, Kalinowski [Kal04]. This section explains the mechanics of the injection, conduction and recombination of charge-carriers.

Injection of Charge Carriers

Under electric bias, charge carriers are injected into the organic layers. Under forward bias, the anode contributes holes and the cathode injects electrons as depicted in Figure 2.4. For an efficient injection, the work function of the cathode must be matched to the polymer by introducing thin doping layers of low workfunction metals. The charge carrier balance is maintained by an additional polymeric HTL at the Anode site. The interface of the HTL to the active polymer forms a hole barrier, which can only be overcome by thermionic emission, tunneling or holes transported into the photo active polymer by hopping among localized states [Shi03, p.23].

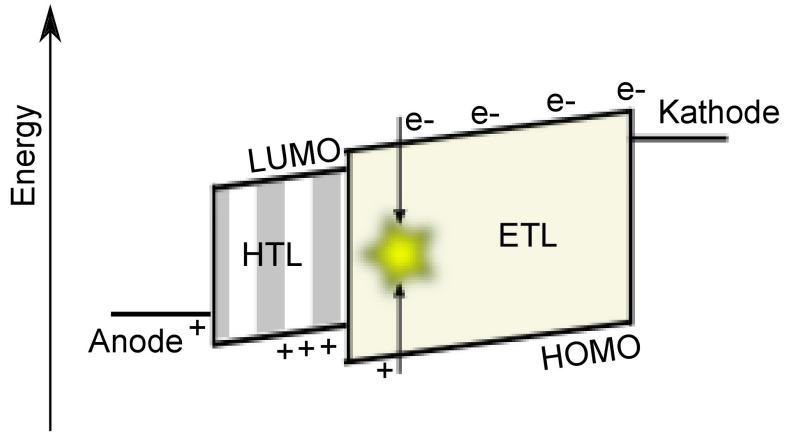

Figure 2.4: General band diagram of an OLED under forward bias, showing a high work function anode, a thin HTL and the photo-active electron transport layer (ETL) where the radiative recombination takes place.

Charge Carrier Transport

Electric conductive polymers obtain their conductivity from delocalized electrons in the polymer molecular chains. Delocalized electrons emerge from double and triple bonds between carbon atoms, so called π-bonds. Figure 2.5 illustrates the π-orbitals, where electrons are delocalized, π-bondings always form their orbitals out of plane of the molecule. The hole conductivity in conjugated polymers for the most OLEDs, lies in the order of $1 \times 10^{-7}\,\mathrm{cm^2\,V^{-1}\,s^{-1}}$ to $1 \times 10^{-3}\,\mathrm{cm^2\,V^{-1}\,s^{-1}}$ while the electron mobility is between one and two orders of magnitude lower [Shi08b, p.23]. Holes in a conjugated polymer are not only more mobile than their counterpart, the electron, furthermore the carrier injection into the emitting OLED polymer works much better for holes. The problem of this unbalanced mobility is that the majority of holes migrates all the way to the cathode, without recombining with an electron. The insufficient electron injection and conduction in the LUMO leads to a general depletion of electrons in the polymer. A general approach to overcome this problem was the invention of the HTL, which aims at slowing down the hole injection by an additional barrier, as depicted in Figure 2.4, and by that re-balance the charge-carriers. The barrier is realized by a polymer material between the anode and the active layer, which has a HOMO slightly lower than the active polymer –

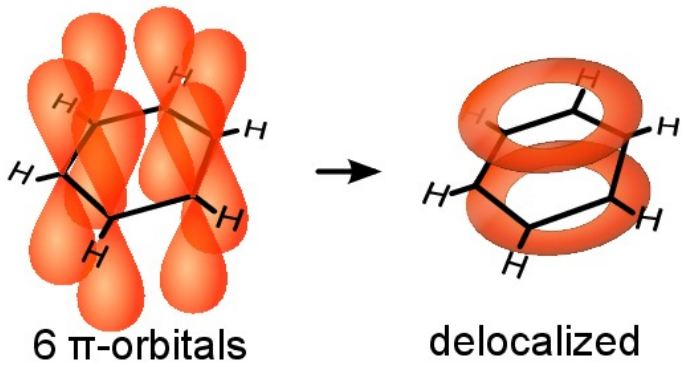

Figure 2.5: Benzene orbitals created by delocalized electrons [Wik13a].

PEDOT:PSS. The improvement of the electron injection is difficult, since chemical bonds between the organic layer and the metal, carrier migration and band-bending changes the work function. However, there is a rule of thumb, which says that the work function should be a little lower than the LUMO so that tunneling and thermal-activated injection are the dominant mechanisms. It is additionally favorable if the material is resistant against oxygen and water. The more stable the materials, the longer the lifetime and the less critical the encapsulation.

Charge Transport Model Charge transport models of conjugated polymers are in contrast to inorganic semiconductors not based on a continuous conduction and valence band, but on discrete states, the lowest unoccupied molecular orbital (LUMO) and the highest occupied molecular orbital (HOMO). The LUMO can be best compared with the conduction band in inorganic semiconductors, hence it is the conductor for injected electrons. The HOMO is the hole conducting band of the polymer and can therefore best be compared to with the valence band. The discrete states are formed by the molecules and the charge transport is dominated by intermolecular charge hopping processes, as depicted in Figure 2.6. Within a molecule, the charge transfer works much faster because of the delocalized electrons, as discussed in Section 2.1.3. However, the intermolecular charge exchange requires a phonon of the right magnitude to induce the hopping process. Additionally, the spin of the electron can not be changed during the hopping event and thus, the destination of the electron must support its spin, i.e. there can not be two electrons of the

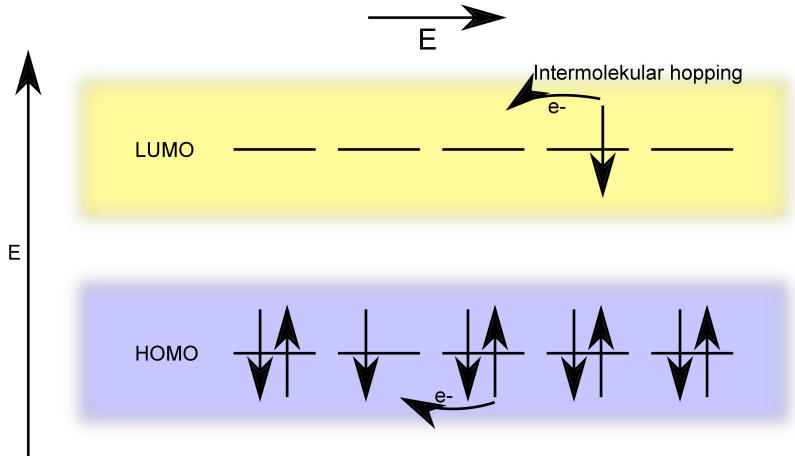

Figure 2.6: Illustration of the hopping states model showing one electron (e-) in the LUMO and one hole in the HOMO, moving towards each other under an electric field. For a hopping transport the electron spin-condition must be satisfied, two electrons in a π-orbital must have an opposing spin. Graph inspired by [Tsc06].

same spin on the same orbital. Electrons and holes are delocalized within one single molecule, but there is no continuity of states through the bulk polymer, in contrast to inorganic semiconductors. The mobility is, as in every semiconductor, dependent on the electric field and the temperature [Tsc06, p.58].

Temperature Influence on the Charge Carrier Mobility A theoretical discussion and simulations on the influence of temperature on the charge carriers can be found in literature. An extensive discussion on the hole mobility in conductive polymers has been published by H. Bässler [Bäs93]. Further work, with a focus on OLEDs has been done by C. Tschamber, who investigated the conductivity and injection barrier with respect to temperature [Tsc06]. It has been demonstrated, that the charge carrier mobility and the injection at barrier interfaces i.e. at the cathode side are, as assumed in theory, temperature dependent. The dominating effect was found to be the hole mobility, which is space charge limited in the conducting region of the device [Baj10]. One can say that in general the conduction improves with rising temperature and the efficiency decreases at the same time. However, the effect of increased mobility is significant stronger than the changes on efficiency.

Recombination of Electrons and Holes

The recombination of electrons and holes is the light emitting process in an OLED. It starts with the injection of the charge carriers, is followed by the formation of an exciton and the emission of light, upon the exciton decay. The injection of charge carriers has been discussed formerly in this section. Charge carriers, electrons which are traveling in the LUMO to the anode and holes traveling in the HOMO to the cathode, can be trapped at the polymer dopant [Gon02]. It has been shown, that it is mostly holes which are trapped, while electrons continue the travel towards anode along the molecular states [Lam01a]. As soon as the electron comes into the field of Coulomb interaction with a trapped hole, electron and hole are bound and form an exciton, which is neutrally charged. From theory, we know that there are four exciton states, which depend on the spin of the electron and on the allowed spin condition of the hole. These exciton states can be divided into the singlet state which emits a photon upon decay, and three triplet states which do not emit photons. It should be mentioned at this point, that triplet states can also be used for light emission, but only under certain conditions and using certain tricks, a field of active research [Su12]. The decay of the singlet exciton results in the emission of a photon with the wavelength corresponding to the band gap energy.

2.1.4 Resonant Cavity OLEDs

A resonant cavity OLED partially confines the emitted light of the active polymer within two mirrors. The setup is similar to a resonant cavity LASER and, similar to the LASER, stimulated emission can be observed. The mirrors are ideally fabricated as Bragg mirrors, however also less ideal mirrors, i.e. a plain metal surface, can also be sufficient. The fabrication of resonant cavity OLEDs has been demonstrated to improve the color purity, or spectral width, and efficiency of OLEDs. Qui et al. for instance fabricated a resonant cavity OLED with a spectral width of 8 nm and 12 nm, using a polymer with a typical emission spectrum of 85 nm and 70 nm width [Qiu06]. The sharpening of the spectral emission peak could be an important issue for the photonic sensing platform, as the best tuning performance of a PC is achieved, when a narrow light source is used. The width of the light spectrum is further discussed in detail in Section 2.4 and 2.5. Micro-cavity devices are fabricated as vertical

resonant cavities between two mirrors, which also serve as electrodes [Puz11]. One of the electrodes should be semi-transparent in order to define light out-coupling of the device and the distance between both mirrors should be in the order of half the emission wavelength. Using this assembly the micro-cavity modes are amplified, whereas other modes are effectively suppressed. Intensity amplification of the cavity, which is attributed to the spatial redistribution of the photon density of states, has been demonstrated and a peak amplification up to 6x is observed [Qiu06].

2.2 Tunable Photonic Crystals

This section introduces the state-of-the-art techniques for the PCss that are used for the photonic sensing platforms proposed in Chapter 5. A PC is an assembly of materials with a different optical RI which can vary in one, two or three dimensions. The optical lattice exhibits a photonic stop-band, which describes the wavelength and direction of light, which can propagate in the material. The proposed sensor uses 1DPCs, also known as Bragg stacks (BSs) to modulate the light in the direction orthogonal to the surface. The used PC consists of a set of alternating porous layers of TiO_2 and SiO_2, that can change their optical properties and thus tune the optical properties of the PC. The tuning can be induced by thermal or chemical stimulation leading to a shift of the photonic stop-band. The basic theory of operation and tuning mechanisms are discussed in this Section.
For a detailed explanation of PCs, the construction of interference and also the calculation and simulation the book "Thin-Film Optical Filters" by H. A. Macelod is recommended at this point [Mac86]. For a very detailed discussion of diverse 1-,2- and 3 dimensional PC structures, including application aspects and the design of PCs, the book "Molding The Flow Of Light" by John D. Joannopoulos shall be recommended [Joa08].
The potential of PCs in sensing applications has been discovered and patents have been given to Arsenault et al. for a tunable BS [Ars11]. A patent is assigned for an imaging device for IR detection based on a tunable PC to Scarpa et al. [Sca08].
PC research has witnessed rapid progress over the past years, materializing in the development of PC building blocks for various optical systems, for example, in fiber-optic communication networks as wavelength-division and add-drop multiplexers,

micro-electro-mechanical systems (MEMS), IR spectrometers, and color displays [Bec07, Yu05, Lam01b, Hoh04]. "Smart" PCs further extend the range of applications toward environmentally responsive sensors, as they are able to dynamically respond to external stimuli through optical thickness changes. An emerging area of applications of stimuli-responsive PCs is the development of label-free biological, chemical, and physical sensors [Nai10, Ge07]. The sensing approach is based on the utilization of PCs as tunable optical filters capable of changing their refractive properties, when in contact with the analyte of interest or when exposed to external stimuli, such as electric and magnetic fields, pH value, etc.. Thermo- and hygroresponsive PCs are of particular interest because of the increasing demand for compact, low-cost, and label-free temperature and humidity sensors [vF12, Kim12].

A PC is a set of alternating materials with different RIs, that can be manufactured in one dimension, meaning a set of alternating layers of high and low RIs also known as a Bragg mirror [Col08], in two dimensions, typically achieved by etching holes into an i.e. silicon substrate [Cho00], or in three dimensions by producing inverted opals [Ren07]. The different concepts are illustrated in Figure 2.7, showing the schematic view on the upper line and a scanning electron microscope (SEM) image below. In

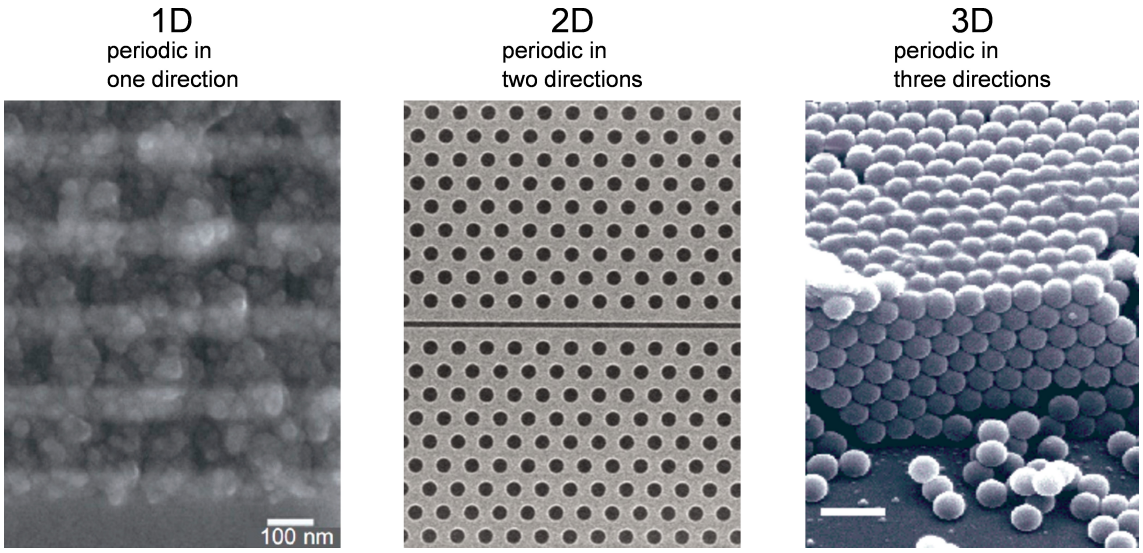

Figure 2.7: SEM pictures of different PCs with a lattice in 1D, 2D and 3D. PC SEMs from numerous sources, 1DPC SEM [Pav12a], 2DPC SEM [SN10] and 3DPC SEM [Col01] Adapted reproduced with permission ©2013.

this work, the focus lies on 1DPCs. The wavelength of maximum reflection can be calculated by the Bragg-Snell law for normal incidence from the formula given in Equation 2.1 where m is the diffraction order of the center wavelength λ and n_H, n_L, t_H, and t_L are the respective RIs (n) and thicknesses (t) of the high- (H) and low- (L) RI materials.

$$m\lambda_{Bragg} = 2(n_H t_H + n_L t_L) \tag{2.1}$$

Therefore, the position of the stop-band can be modulated by varying the optical thickness (the product of RI and physical thickness) of the layers [Bon09].

2.2.1 Stop-Band Tuning by Refractive Index Changes

One possible mechanism of color tuning is based on the thermo-optic effect (TOE), i.e., the dependence of the RI of a material on temperature. Herein the focus lies on silicon dioxide (SiO_2) and (TiO_2), which both are excellent coating materials, because of their high transparency in optical wavelength and their rigidity. The thermo-optic coefficient (TOC), which describes the change of RI due to heating, of TiO_2 measured for coatings deposited by electron beam PVD is negative and equal to -1.77 10^{-4} K^{-1} between 18 °C and 120 °C and $-3.04 \times 10^{-4}\,K^{-1}$ between 220 °C and 325 °C at 800 nm [Gül02]. Xie et al. compared the TOC of TiO_2 films obtained by magnetron sputtering [Xie09]. The TOC of non-annealed films was found to be $-1.21 \times 10^{-4}\,K^{-1}$, while values around $-2.14 \times 10^{-4}\,K^{-1}$ were reported for an annealed sample in the temperature range between 31 °C and 105 °C at 632 nm. In contrast, the TOC of SiO_2 is positive and ranges between $0.88 \times 10^{-5}\,K^{-1}$ and $1.34 \times 10^{-5}\,K^{-1}$ [Gho95]. A change in RI due to the change of thickness is negligible since the thermal expansion coefficient (TEC) for both materials is on the order of $1 \times 10^{-6}\,K^{-1}$. The tuning mechanism based on the TOE has already been demonstrated on optical filters produced mainly by expensive deposition techniques, such as sputtering, electron beam evaporation, or plasma-enhanced PVD. The tuning efficiency of a single amorphous Si cavity arranged between Si_3N_4/SiO_2 distributed Bragg reflectors (DBRs) was measured to be 0.05 nm K^{-1},[Hoh04] whereas that of a polycrystalline (poly-)Si cavity in poly-Si/SiO_2 DBRs was reported to be 0.07 nm/K [Hoh03]. A similar approach demonstrated thermal tunability of the emission of conjugated polymers embedded in a microcavity between DBRs deposited by reactive

electron beam evaporation [Reg08]. The photoluminescence spectra of the polymers inside the cavity were tuned with an efficiency of -0.2 nm/K. A wavelength shift of 0.01 nm/K was verified for external-cavity DBR laser with a silica fiber Bragg grating [Ber98].

In the following, the tuning mechanisms (i) pore infiltration, (ii) thermal expansion and (iii) swelling, which can be used for versatile sensing applications, are presented. It should be noted that one often observes a mixture of the mentioned effects and that it might be difficult to separate the effects or distinguish between analytes by the response alone.

Pore Infiltration Besides the thermal tuning the RI can be changed by the infiltration of voids in the BS if the filling material has a RI > 1. The voids can be intended by using porous materials or occur as a defect, such as cracks in the crystal [Cal11]. The infiltration can also be observed, when a thermal tuning is performed due to water removal from the BS upon heating in ambient conditions [Pel88, Sax84, Mac76, Gib83]. The named groups observed the influence of humidity as a parasitic effect, that occurred in cracked films, which made the PC accessible to ambient water vapor. The potential of porous PCs as sensitive elements has been identified and there is a huge interest in structures that can be reversibly infiltrated by an analyte [vF12, Cal11].These rigid structures that do not change there dimensions, however, change their optical thickness, due to RI change of the respective materials, which causes the shift of the photonic stop-band. For the case of small pores - pore size << layer-thickness – the RI change can be estimated using the Bruggeman equation 2.2 [Cal11]. Where n is the RI and ff the filling factor, the subscripts s and p stand for solid phase of the material and pores, respectively.

$$\frac{n_s^2 - n^2}{n_s^2 + 2n^2} ff_s + \frac{n_p^2 - n^2}{n_p^2 + 2n^2} ff_p = 0 \tag{2.2}$$

Equation 2.2 shows the two factors, that can influence the change of RI, which is the grade of porosity of the material itself and the RI of the infiltrator. Obviously, if the BS is infiltrated by a material with a RI that equals the RI of the pores before infiltration, no change can be observed.

2.2.2 Stop-Band Tuning by Expansion

The stop-band tunes according to the Bragg-Snell law according to Equation 2.1 with the change of optical thickness. As the optical thickness is the product of the physical thickness and the RI, a change of thickness by expansion can lead to an increased optical thickness. However, care must be taken as both effects, thickness change and RI change, can coexist and even correlate - in fact the two phenomena can have a counteracting effect on the optical thickness [Zha06, Kan02]. Thermal expansion is generally described by the TEC which lies in the order of $1 \times 10^{-6}\,\mathrm{K}^{-1}$ for solid optical materials and between $1.7 \times 10^{-4}\,\mathrm{K}^{-1}$ to $7.2 \times 10^{-4}\,\mathrm{K}^{-1}$ for polymers [Zha06].

Swelling Polymers The swelling of polymers is another form of expansion, which occurs upon adsorption of chemicals. Examples for swelling polymers are: Tian et al. who fabricated a PC of acrylamide infiltrated latex spheres which showed a stop-band shift of up to 240 nm when exposed to a relative humidity between 20% and 100% [Tia08]. A similar approach has been followed by Arsenault et al. who fabricated polyferrocenylsilane gel PCs and demonstrated a tunability by dichloromethane of more than 100 nm [Ars05]. The response speed of swelling polymers lies in the order of seconds or minutes, depending on the solvent, the polymer and its thickness [Tia08, Ars05].

The sensitivity for the above mentioned tuning mechanism is generally broad, since the infiltration process works for every molecule, that is small enough to fit in the pores. Approaches to high selectivity have been demonstrated by Burgess et al. and Raymond et al. using surface-modification to selectively detect e.g. alcohols, aliphatic compounds and different grades of gasoline [Bur12, Bur11, Ray12]. Alternative approaches have been demonstrated with the metal-organic framework ZIF-8,[Hin12] and by the time domain analysis of the PC response [Kel11].

2.3 Organic Photodetector

The basic working principle of an OPD follows the processes of the OLED in a reversed order. Light is captured and leads to the excitation of an electron hole

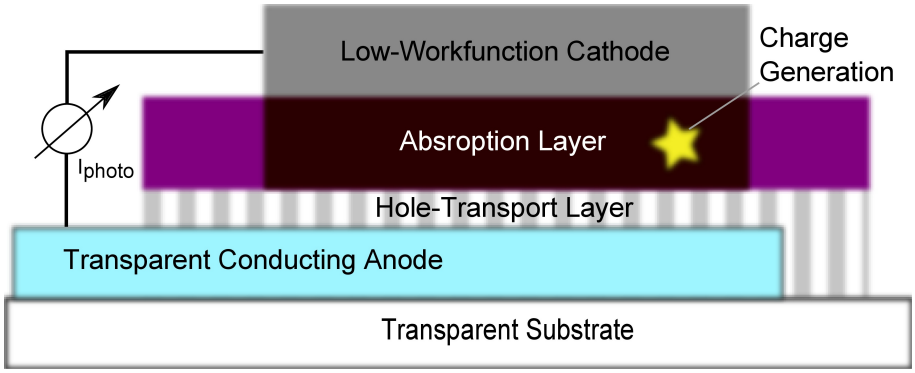

Figure 2.8: Schematic view of the ODP. Light is coupled in through the transparent substrate and absorbed in the absorption layer. The generated charge is than extracted to the anode and cathode. I_{photon} indicates the light induced current.

pair. The electron hole pair is seperated in the active polymer and extracted via the electrodes. The scheme in Figure 2.8 illustrates the structure of the OPD used in this work. The major challenge of the OPD is the efficient separation of the excited electron hole pair since the pair is uncharged and requires very high field strength to be separated. The separation is achieved by the use of a polymer blend of e.g. P3HT and PCBM, which forms a poly crystalline inner structure with very high field strength at the crystal boundaries [Moo02]. The high field strength at the interface between the P3HT and PCBM grains induces the separation of the electron hole pair and can subsequently be extracted by an applied voltage in reverse bias. The OPDs in this thesis have been fabricated by Daniela Baierl and the fabrication and necessary background is explained in the corresponding PhD thesis [Bai12a]. As well as in numerous journal publications [Bai11a, Bai11b, Bai12b].

2.4 Infrared Detectors

This section gives an introduction to IR sensors along with a literature overview for existing IR sensors and characterization techniques. A new concept, IR detection via the TOE, is presented using a 1DPC as a temperature tuned light valve. We published the proof of concept as a journal article and most of the following text can be found there [Exn13].

So far, many approaches have been made to realize small, cheap and precise infrared(IR) sensors [Rog03]. Two subcategories have won major recognition [Rog02]: (i) photo electric detectors and (ii) thermal detectors. Photoelectric detectors convert the incident IR photons into electrical charge by the internal photoelectric effect. Photon detectors exhibit the best IR sensitivity but require cryogenic cooling due to their small band gap which makes them bulky, heavy and expensive [Rog03, Rog05, Der96]. Typical semiconductor materials for photo electric IR sensors are HgCdTe, PbS and PbSe [Emm75]. These materials require epitaxial growth, vacuum processes, and photo-lithographic masking and etching which makes fabrication difficult and expensive [Smi01]. The second category, the thermal detectors, absorb the IR-radiation which produces a corresponding change of one of the material parameters, which can be the resistance, reflectance phase shift etc.. In the case of a resistive bolometer the absorbed IR radiation locally heats the sensor, which changes the electric resistance. Thermal detector technology takes advantage of semiconducting materials [Ish00] or thermally sensitive resistors, that exhibit a temperature coefficient of about $4\,\%\,\mathrm{K}^{-1}$ [El 00]. Typical materials are vanadium compounds [El 00, Che01, Woo01], compounds of manganese oxide, nickel oxide and cobalt oxide[Uma02], polycrystalline silicon-germanium alloy[Sed98] or micro machined bimetallic cantilevers[Lav06]. Thermal detectors do not reqtiuire cryogenic cooling, which makes them easy to use and reduces the system costs [Emm75, Smi68]. However, thermo-resistive detectors require complicated etching techniques and membrane transfer bonding techniques, which requires many processing steps that are known to have a low fabrication yield [Nik01]. The sensitivity of IR detectors is limited by the response of the material and noise of the measurement. A general formula for the sensitivity is the noise-equivalent temperature difference(NETD)[Der96]

$$NETD = \Delta T/(v_s/v_n) \tag{2.3}$$

ΔT is the temperature change, v_s the corresponding signal difference and v_n the noise of the setup. From Equation 2.3 we see the NETD can be reduced by increasing the signal difference v_s while keeping the noise low. Therefore, we need

materials with at least one characteristic that is strongly temperature dependent [Kru80]. The changing characteristic has in the past often been electric since electric properties can easily be measured by integrated electronics [Kru01]. However, one is restricted to the electrical characteristics of the material. Our approach is the design of a novel detector which allows to measure optical parameters like the RI of the material. This approach opens a whole palette of materials, namely all optical transparent materials with a response to temperature change. In a previous publication we have shown that the RI is a good candidate of the optical parameters because of the possible high sensitivity [Pav12a]. The RI readout can be simplified by assembling the materials in a BS, which consists of a set of high and low RI materials. The assembly offers a stop-band according to classic multilayer interference theory [Mac86]. The stop-band can be tuned by the optical thickness, which is described in the corresponding section 2.2.
For further reading on the topic of IR sensors the book "Electro-Optical Systems Design, Analysis, and Testing" by Michael Dudzik can be recommended for insights on bolometric IR sensors [Acc96]. For different characterization methods the journal article "Laboratory Measurement of Sampled Infrared Imaging System Performance" introduces characterization methods for IR detectors that have become common [Dri99]. Furthermore, another work with the focus on the main performance parameter of IR detectors, the minimum resolvable temperature difference, shall be recommended here [Kra02].

2.4.1 IR Detection via the Thermo-Optic Effect

The sensors working principle is based on the TOE of the materials in the PC, which exhibit a change of RI upon heating by the absorption of IR light. Small changes of the RI can be measured with an elipsometer or a refractometer. However, the measurement of the RI in a low-cost or even portable, battery driven way is a major challenge, therefore it is a good to assemble the material in a PC. In a PC, the RI change causes the stop-band of the PC to shift according to the change of optical thickness. The shift of the photonic stop-band is far easier to detect, as it corresponds to a change of transmittance at a fixed wavelength, see Figure 2.9. The transmission can be detected with a light source, which must be monochromatic, or

at least posses a distinct color and an optical detector. The focus of this thesis is to deliver an optical platform which measures the transmission, the proposed sensors are explained in the corresponding Chapter 5.

2.5 Chemical Sensors

The field of application for gas sensors for the detection of selected air components is inherently broad. Applications ranges from environmental monitoring (CO and CO_2) to medical diagnostics (Ethanol and NH_3) and to air conditioning (humidity). Current research aims for sensors with a high sensitivity to only certain gases while at the same time being able to detect a high concentration range. Presently the best performing sensors employ capacitive and semiconducting sensitive elements and measure the electric response. The best performance is achieved when sensors based semiconducting oxides like In_2O_3, SnO_2, ZnO, TiO_2, and CuO are fabricated with a nano-structured surface [Che08, Hon10]. As the surface area generally increases the sensitivity the attempts also range to the fabrication of 3D like SnO_2 sensors [Mei12]. Besides the generally poor selectivity the semiconducting sensors also posses a strong hysteresis and sensors often must be heated. Our approach utilizes the chemical and optical properties of a porous PC for the detection of gasses. Various analytes can alter the PC in the sense of colorimetric changes, the colorimetric changes can be electrically read out via the photonic sensing platform proposed in Section 5.2. This section describes the working principle of tunable PCs for chemical sensing applications.

Colorimetric sensors are well known ever since the litmus pH paper, glucose, and pregnancy color tests where broadly available at a reasonable low price. In literature a color change of the PC is usually proposed to be read out by a bulky spectrometer, or by the naked eye, which in turn may give rise to ambiguities. First approaches to a simplification have been demonstrated by several groups, who used a laser and measured the change of reflected power upon exposure to acetone, chlorobencene and water vapor [Sno99, Shi08a]. A very versatile principle for the detection of the photonic stop-band position has been demonstrated by Fang et al. using a color sensitive complementary metal oxide semiconductor (CMOS) detector, which holds

the advantage of detecting the stop-band position in a broad wavelength range from 425 nm to 700 nm [Hsi06]. A further step towards low-cost integration has been provided by Nazirizadeh et al. who detected the polarization rotation of a bio-sensor by a simple LED and an photodetector and two polarizers [Naz10]. The above named sensors are all gas sensors, however also sensors for fluids have been investigated [Kus07].

2.5.1 Chemical Sensor Based on a Porous PC

The underlying principle of the proposed sensor is the adsorption of molecules into the porous structure of a PC. The adsorption of molecules into the PC increases the RI. The optical lattice of the PC increases proportional to the RI changes and by that the stop-band is shifted to longer wavelength as depicted in Figure 2.9. This shift can be detected with a spectrometer or a monochromator. However, a far simpler approach is the measurement of the transmission at a single wavelength. The transmission for green light (550 nm) changes roughly by the factor 5 in Figure 2.9. This change can be visualized when a green light source, i.e. an OLED is used. The transmitted light can be recorded by a photodetector, for instance an OPD.

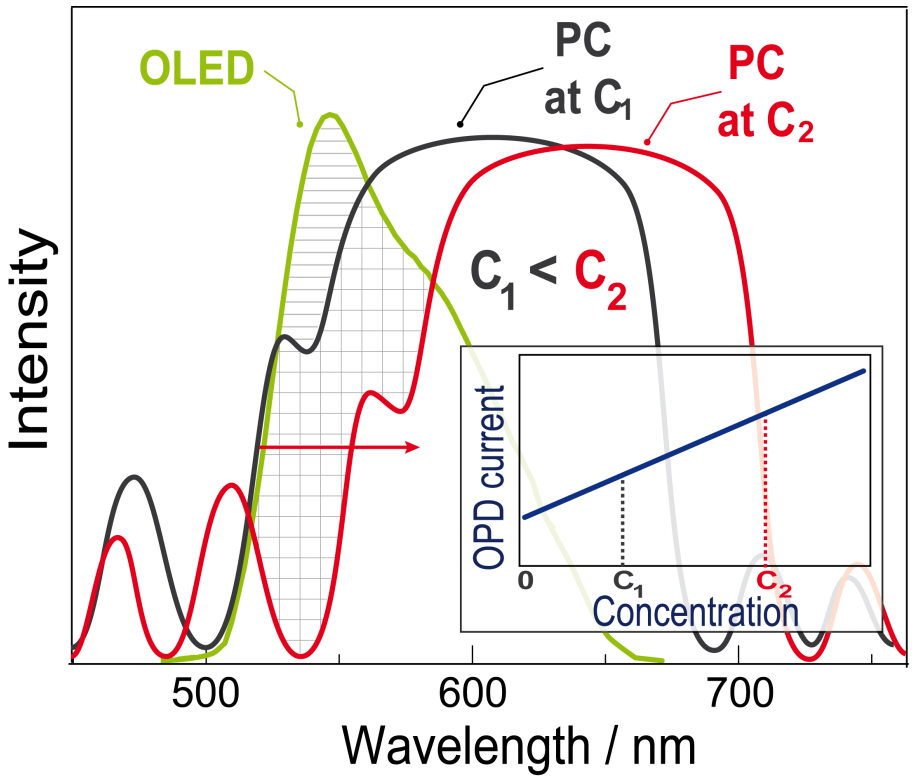

Figure 2.9: Demonstration how the photonic stop-band tuning affects the light intensity of the transmitted light. The adsorption of molecules shifts the photonic stop-band to the red, due to the change of RI. The blue shift effects the transmitted light at the emission wavelength of the OLED. The tuned light is recorded by the OPD and a concentration changes can be seen in the change of the photo-current delivered. Image courtesy of Ida Pavlichenko.

3 Experimental Details

In this chapter, the experimental methods that were used for the fabrication and characterization are documented. The methods described in this chapter are used throughout the thesis, if not stated differently.

3.1 Device Fabrication

Herein, the fabrication of the used devices is described step by step. All processes, even if not explicitly stated in the methods, were done in a generally clean environment and extra care has been taken so that only a minimum number of particles and impurities contaminated the samples. Standard inspection gloves were used during every step of the process. Glasses, containers and magnetic stirrers for the solution were cleaned prior first use.

3.1.1 OLED Fabrication

OLEDs were fabricated on a glass substrate covered with a structured ITO transparent electrode. The substrates were cleaned in an ultrasonic bath, in propanol and acetone and subsequently in an oxygen plasma. Then, the samples were transfered into a glovebox with N_2 atmosphere, where the OLED fabrication was performed. First, a 20 nm thick PEDOT:PSS layer was deposited using the spin-coating technique to improve the injection of holes into the active polymer. Subsequently, the poly(para-phenylene vinylene) copolymer solution, Super Yellow (Merck PDY-132) dissolved at a concentration of 0.5 wt% in toluene, was spin-coated onto the sample at 1500 rpm giving a layer thickness of approximately 80 nm. Subsequently, the samples were transfered into a high vacuum chamber (Leybold) at a pressure of approximately 1×10^{-6} mbar to deposit the top electrodes. The electrodes were

evaporated by means of the thermal PVD method in the following sequence: first, a 25 nm Calcium layer, and second a 125 nm Silver layer. The OLEDs were encapsulated with a microscope glass cover-glass glued (Araldite2011, Huntsman) on top of the device. The OLED size is a $3 \times 3\,\mathrm{mm}^2$, if not stated differently.

Solution Preparation In this thesis, two different polymers have been used. The Yellow emitting PDY-132 and the blue emitting SPB-02T. The preparation of the PDY-132 solution was done by mixing PDY-132 polymer from solid phase with toluene in a concentration of 0.5 % by weight in a glass bottle with Teflon lock. The SPB-02T was also dissolved at a concentration of 1 wt% in toluene. The solution was stirred using a magnetic stirrer at low speed and room temperature for 24 h. The shelf life of the polymer solution is at least one year without significant degradation.

Process Parameters

- Cleaning in ultrasonic bath of first, acetone and second propanol for 10 min, respectively
- Surface activation in oxygen plasma (Diener) at 100% for 1 min.
- Spin-coating of PEDOT:PSS (4083, Clevios) at 6000 rpm with maximum acceleration in pure N_2 atmosphere (Glovebox).
- Spin-coating of the OLED polymer PDY-132 at 1500 rpm with acceleration "2", resulting in a layer-thickness of approximately 80 nm in pure N_2 atmosphere (Glovebox).
- Evaporation of 25 nm Calcium at a rate of minimum $0.5\,\mathrm{Å\,s^{-1}}$ at the beginning of the evaporation and increased to $1\,\mathrm{Å\,s^{-1}}$. The rate of $0.5\,\mathrm{Å\,s^{-1}}$ was stabilized before the substrate shutter was opened (rate establish function).
- Evaporation of 125 nm Silver at a rate of minimum $1\,\mathrm{Å\,s^{-1}}$ at the beginning of the evaporation and increased to $3\,\mathrm{Å\,s^{-1}}$.
- Encapsulation with a microscope cover-glass glued on top by a two component epoxy (Araldite2011, Huntsman). A short heat treatment (80 °C, 30 s) after

the glue application is required to decrease the viscosity. Subsequently, 24 h curing at room temperature in N_2 atmosphere is recommended.

- The contact pads should be reinforced with silver conductive paste before connecting the electrodes.

3.1.2 OPD Fabrication

The OPDs were fabricated on the same ITO structured transparent electrodes as the OLEDs, giving a diode size of $3 \times 3\,mm^2$. The ITO was covered with a thin layer approximately 20 nm of PEDOT4083 (Clevios) and followed by a 300 nm thick layer of the active polymer. The active polymer was a blend of P3HT and PCBM with the weight ratio of 1:1 dissolved in dichlorobenzene. Subsequently a 150 nm thick aluminum electrode has been evaporated by CVD. All polymer processing steps have been done in a glove-box, containing pure nitrogen. Before the release of the device, an encapsulation glass has been glued on top of the device. The devices have a shelf life, which defines the time the devices can be stored without operation, of more than one year, however during operation at reverse bias they show stronger degradation. Especially the initial degradation drop during the first hour has to be taken care of. Herein we applied a reverse bias of −4 V for one hour to stabilize the device before the first measurement.

The OPDs for this thesis have been fabricated by Daniela Baierl during her PhD studies, detailed fabrication processes are documented in the corresponding thesis [Bai12a].

3.1.3 Porous PC Fabrication from Suspension

The PCs were fabricated via spin-coating from a nanoparticle (NP) suspension. The suspension was prepared in advance and has a shelf life of more than one year. It is important for reproducible layer properties to fabricate the suspension once, in a huge amount and than always use the same solution. After the spin-coating the layers were calcined in an oven.

Preparation of TiO_2 Suspension The suspension of TiO_2 NPs was synthesized by the sol-gel hydrolysis of titanium(IV) ethoxide (6.25 mL, technical grade, Aldrich) in HNO_3 (0.1 M, 37.5 mL) [Lot08]. Titanium(IV) ethoxide was added dropwise to the acid at room temperature during vigorous stirring in a N_2 atmosphere. The mixture was then heated at 80 °C for 8 h. The subsequent sonication (Elmasonic S100/H, 37 kHz) of the sol allowed obtaining NPs with a hydrodynamic diameter in the range between 7 nm and 15 nm.

Preparation of SiO_2 Suspension SiO_2 colloids (hydrodynamic diameter 6 nm to 10 nm) were purchased from Sigma-Aldrich (LUDOX SM-30, 30 wt% in H_2O) and diluted with distilled water using a ratio of 1:5. The Particle size distribution of the precursor TiO_2 and SiO_2 suspensions was analyzed using dynamic light scattering photocorrelation spectroscopy (Malvern Nano ZS Zetasizer) at 20 °C. The crystalline nature of the TiO_2 powder calcined at 350 °C for 1 h was confirmed by X-ray diffraction (Bruker D8 Discover).

PC Assembly Thermoresponsive PCs were assembled by sequential deposition of TiO_2 and SiO_2 suspensions on a clean ISO 8037/1 glass side (2.5 × 2.5 cm^2) previously activated by air plasma treatment (Femto, Diener Electronic). To improve the TiO_2 film quality, 2.5 wt% of poly(ethylene glycol) (Mw = 8000 g mol^{-1}) was added for spin coating. Both suspensions were filtered using syringe filters (SPARTAN 13, 0.2 µm) to remove aggregates. Thin layers of TiO_2 and SiO_2 were produced by using the spin-coating technique (Laurell WS-650SZ-6NPP/LITE). The glass slides were covered by 200 µL to 250 µL of TiO_2 suspension and accelerated at 1500 rpm s^{-1} to final rotation speeds ranging from 2500 rpm to 5500 rpm. The total spin-coating process for each layer was completed in 60 s. Afterwards the sample was put into a muffle furnace (Nabertherm, L3/11/B810) for calcination at 350 °C for 30 min.The same procedure was applied to the deposition of the following layers until 8.5 TiO_2/SiO_2 bilayers were assembled.

3.1.4 Fabrication of Dense PCs

The dense TiO_{2-x}/SiO_{2-x} multilayer structure was deposited in a Pfeiffer Vacuum Classic 500 evaporation system at a pressure of $< 2 \times 10^{-6}$ mbar onto soda-lime glass substrates at room temperature starting from the TiO_{2-x} layer. The TiO_{2-x} layers were evaporated by using an electron gun. The SiO_{2-x} layers were evaporated by using resistive heating of SiO_2 from a molybdenum boat. The deposition rate for both materials was approximately $2\,\text{Å}\,\text{s}^{-1}$. The alternation of the layers was achieved by shuttering the flux of the corresponding layer. The oxygen content in the multilayers was reduced because of deposition in vacuum; therefore, further annealing in an oxygen atmosphere for one hour at 450 °C was performed to recover the stoichiometry and optical properties of the multilayers.

3.2 Measurement Setup

A variety of setups have been used to characterize the OLED, OPD and PCs. This section describes each single characterization component, which may in practice be combined so that the simultaneous control of multiple parameter is possible.

3.2.1 Monochromator Measurements

To obtain transmission spectra of the BS in the range of 400 nm to 800 nm, we used a monochromator (Cornerstone260 1/4 m) with a high-pressure arc lamp as a light source and a $10 \times 10\,\text{mm}^2$ calibrated silicon detector connected to a digital lock-in amplifier (Merlin). The sample was mounted in the sample holder and placed before the detector in a closed chamber (the distances "monochromator-sample" and "sample-detector" were 8 cm and 12 cm, respectively). The monochromator was computer controlled using the TracQ software.

3.2.2 Spectroscopic Ellipsometry

The single thin film thickness of TiO_2 and SiO_2 layers was characterized by spectroscopic ellipsometry performed on a Woollam M200D variable angle ellipsometer in the entire spectral range of 190 nm to 1000 nm at angles of incidence of 65°, 70°,

75°. For the data fitting and calculation of the parameters the Cauchy model was used.

3.2.3 Thermo-Optical Analysis

For the measurement of the sample temperature a platinum resistive thermometer with 100 Ω electric resistance (PT100) temperature sensor was attached to the sample close to the optical axis. Peltier elements were mounted, depending on the setup, either on the backside, covering the whole sample or using two Peltier elements with a gap in-between, so that the optical accessibility was granted. The two setups are illustrated in Figure 3.1 and 3.2b. The remaining side of the Peltier element was attached to a passive aluminum cooler using heat conductive paste or foil (graphene) and the sandwich: cooler-Peltier-sample was pressed together with a screw. The

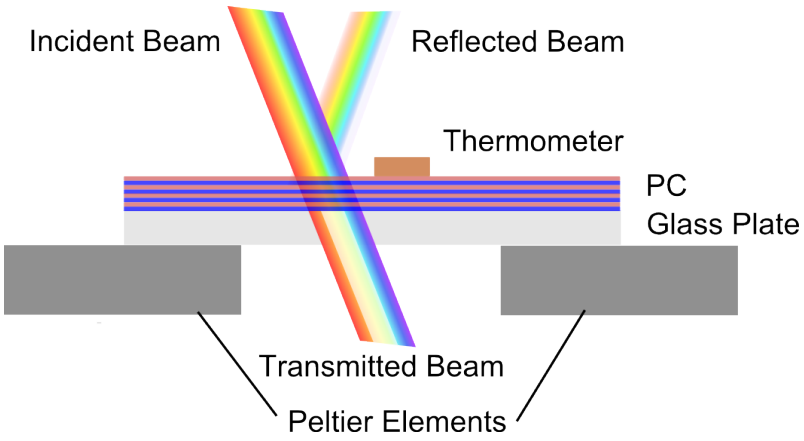

Figure 3.1: Scheme of the experimental setup. The PC transmits parts of the spectrum an reflects the rest. The Peltier elements where placed with a gap to measure the transmitted light.

PT100 and the Peltier elements were both connected to a sourcemeter (Keithley), which was remote controlled by a computer running a LabView program. The computer program calculated the actual temperature of the PT100 element using a lookup table and controlled the Peltier elements using a software proportional-integral-controller to stabilize the desired temperature. The temperature could be varied between 10 °C and 80 °C, the thermal equilibration time, between when the temperature was reached and before the measurement, was one minute. The mea-

sured deviation of the temperature during the measurement was less than 0.1 °C. With the thermo-optical setup the measurements were started automatically by the LabView program. For the monochromator a modified LabView program has been used to take the transmission curves.

3.2.4 Humidity Control Setup

We changed the relative humidity (RH) of the environment by introducing water vapor into the monochromator chamber. The RH was varied between 25% and 80%. The water vapor was produced by a hot bowl of water, where the water temperature determined the RH in the chamber. The RH was tracked using an USB humidity sensor (Hid TEMPerHUM).

3.2.5 Luminance Measurement

For the measurement of the light intensity the calibrated luminance meter "Mavo Spot 2" was used. The sample and the luminancemeter were mounted on an optical table, so that the luminancemeter optical axis was orthogonal to the sample surface, with a distance of 25 cm. Macro lenses were used to focus on this relative short distance. The setup is shown in Figure 3.2b. The luminance meter was remote controlled by a computer with an USB adapter. A LabView program was used to acquire and store the data.

3.2.6 Gas-Gas Flow Setup

For concentrations between 0 and 260 ppm ethanol in nitrogen a gas-gas mass-flow setup was used, meaning that two gases were mixed using mass-flow controllers (Bronkhorst). The test gas contained 260 ppm of ethanol in N_2 and was mixed with the carrier gas which was pure N_2 to the desired concentration. Therefore the maximum ethanol concentration is limited to 260 ppm. The advantage of this setup is the uncomplicated and precise tuning of the concentration. The gas-flow of the gas mixture was kept constant at 200 mL min^{-1} and the two flows were controlled accordingly, so that the desired mixing ratio was achieved.

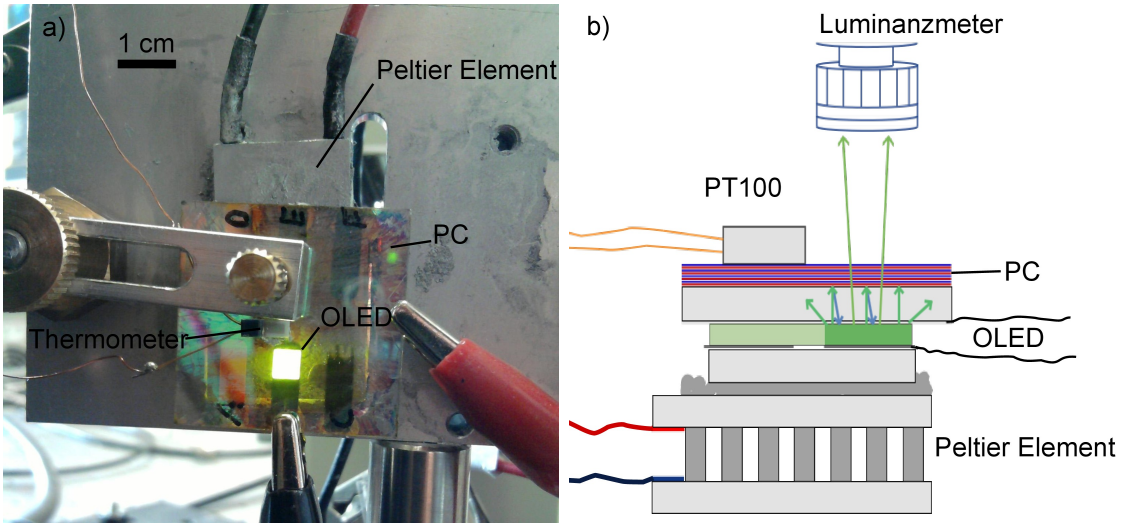

Figure 3.2: (a) Photograph of the sample holder with an emitting OLED-PC couple mounted onto the Peltier element. (b) Scheme of the experimental setup for the luminance measurements.

3.2.7 Gas-Liquid Flow Setup

The gas-liquid flow setup is located at the LMU and can be used for the whole range of mixing ratios, in other words, for an ethanol saturation pressure p/p* between 0% and 100% in N_2. One gas mass-flow controller (Bronkhorst) regulates the N_2 carrier gas flow to constant 200 mL min^{-1}. The second mass-flow controller regulates the ethanol (liquid) flow in the range between 0 g h^{-1} and 2 g h^{-1}. The ethanol is vaporized at a temperature of 150 °C by a liquid evaporation system (Bronkhorst). The two gases are mixed and the ethanol saturation pressure must be calculated according to several process parameters, which are the temperature and pressure of each component and the ambient pressure. The calculations have been done using the software *Fluidat* [FLU13], which takes atmospheric pressure, temperature and pressure of the individual components into account, to determine the partial ethanol pressure (p) and total pressure (p*). The fraction p/p* is the relative ethanol saturation which ranges from 0, for 100% nitrogen, to 1, for ethanol saturated nitrogen vapor. The ratio p/p* can also be expressed on the percentage scale accordingly (0% to 100%). The challenge with this setup is, that the saturation pressure must always be calculated and many parameters can influence the resulting

concentration. Also, the liquid mass-flow is more difficult to stabilize.

3.3 Calculations and Simulations

In this Section general formulas are collected. Simulation details for the COMSOL simulations are presented [COM06].

OLED Parameters The OLED performance can be categorized in several standard parameters, that are calculated from the luminous intensity, power consumption and geometry of the OLED. The current density (CD) gives the current flowing through a defined area and is calculated according to Equation 3.1. The efficiency (Eff) gives the brightness and of the source per current and is calculated in Equation 3.2. The power efficiency (Peff) is the light flux per electric power as calculated in Equation 3.3.

$$CD\ [A\ m^{-2}] = \frac{current\ [A]}{area\ [m^2]} \tag{3.1}$$

$$Eff\ [cd\ A^{-1}] = \frac{luminance\ [cd\ m^{-2}]}{CD\ [A\ m^{-2}]} \tag{3.2}$$

$$Peff\ [lm\ W^{-1}] = \frac{luminance\ [cd\ m^{-2}] \cdot area\ [m^2] \cdot 2\pi}{voltage\ [V] \cdot current\ [A]} \tag{3.3}$$

Normalized Response The normalized response (NR) in the common language of sensors means the response of the sensor with respect to its initial signal. Often sensors do exhibit an offset, which means that the output signal of the sensor, without exposure to an analyte is not zero. For the determination how sensitive the sensor is, the signal response I_r, in comparison with the initial signal I_i, is of interest. Equation 3.4 shows the calculation of the NR in percent.

$$NR[\%] = \frac{I_r - I_i}{I_i} \tag{3.4}$$

COMSOL Multiphysics Simulations Simulatons with COMSOL Multiphysics were carried out using COMSOL 3.2 in the electromagnetic mode for in plane waves [COM06]. The layer structure of the PC was simplified for the simulations, so that only two dimensions were simulated with a width (layer extension) of 1×10^{-6} m

and a height according to the layer numbers and thickness between 1×10^{-6} m and 10×10^{-6} m. Substrates and covering air layers were simulated with a thickness of 1×10^{-6} m. The field excitation was set to $1\,\mathrm{V\,m^{-1}}$ at one side and all boundaries to the outside of the structure were simulated as *matched boundary*. The user interface was used for the construction of the layer setup, which consisted of either the PC only, or the PC on a glass substrate and interfacing layers of air. The simulations with a maximum reflection/transmission of 100% and 0% respectively were the ones that were simulated without glass and air layers, others are simulated with air layers. The readily drawn structure in COMSOL with the simulated electric field distribution is shown in Figure 3.3. The electric field is according to the simulated wavelength oscillating, red and blue areas indicate a higher field strength. In the figure 9 bilayers of TiO_2 and SiO_2 are simulated without substrate and air layers. The wave excitation was applied from the left side of the structure. The simulation details are concluded in Table 3.1.

Parameter	Value	Comment
Mode	in plane TE-waves	electric field Z-component
TiO_2 thickness	45 nm	
TiO_2 RI	1.8743	9 layers
SiO_2 thickness	400 nm	
SiO_2 RI	1.1443	9 layers
Simulated wavelength	600 nm	in Figure 3.3
Wave excitation	$1\,\mathrm{V\,m^{-1}}$	at the left port

Table 3.1: Simulation parameters for the field distribution shown in Figure 3.3.

The drawn structure has been exported to a MATLAB file and was modified to a MATLAB function, that calculates the transmission, with respect to the RI and thickness of two alternating materials with 9 bi-layers. The function is shown in the Appendix A.3.2. With this function it is possible to simulate a set of RI and thickness parameters, without having to redraw the structure and using the MATLAB interface for subsequent calculation and storage.
The "parametric linear" problem solver in COMSOL was used to simulate the S-parameter matrix of the assembled structure in the wavelength range from 300 nm to 900 nm with a step of 1 nm. Subsequently, the real part of the S_{21} parameter, which is given in dB, was taken and the transmission and reflection was calculated

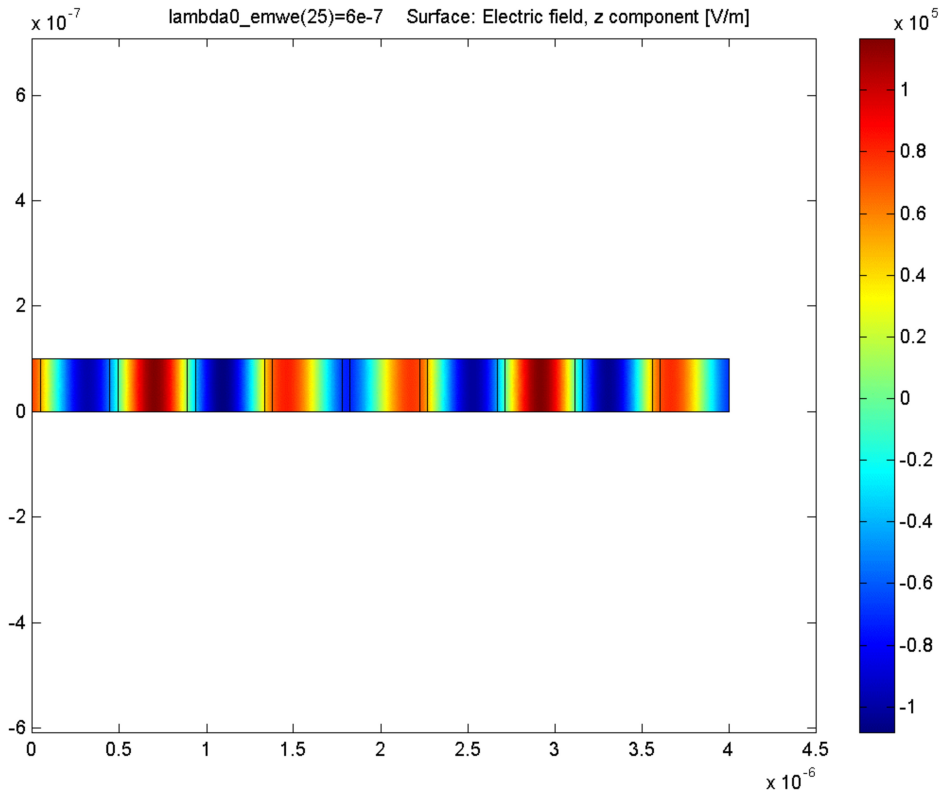

Figure 3.3: Simulation of the electric field distribution of a PC structure with 9 bilayers at 600 nm wavelength. The color indicates the strength of the field with blue and red indicating a high field strength and green low strength of field.

according to Equation 3.5 and 3.6.

$$Transmission\ [\%] = 10^{\frac{S_{21}}{10}} \cdot 100\% \tag{3.5}$$

$$Reflection\ [\%] = 100 - Transmission\ [\%] \tag{3.6}$$

4 Sensor Components

In this chapter, the experimental results and optimization steps of the organic and inorganic sensor components are presented. The organic components, the OLED and OPD, are presented in Section 4.1 and 4.3. The inorganic component, the PC, is presented in Section 4.2. Inorganic sensors that have been used in some experiments, i.e. charge-coupled device (CCD) and CMOS cameras, are not represented here, as they were purchased readily and no engineering was conducted.

4.1 The Organic Light Emitting Diode

Organic light emitting diodes (OLEDs) are used as a light source in the proposed sensors in order to determine the stop-band position. This section provides a general overview of the OLED with respect to the special requirements for the use as a sensor. The OLED fabrication process has been optimized and the electro-optical characteristics are compared with data-sheet values in Section 4.1.1. A detailed investigation of the thermal response is conducted in Section 4.1.2, which delivers the basic knowledge for the design of an integrated IR sensor. The fabrication and measurement procedures are presented in Chapter 3. Two of the fabricated OLEDs are presented in Figure 4.1.

4.1.1 OLED Polymers

From the broad variety of OLED polymers on the market, the polymer PDY-132 (Merck) has been selected due to its good stability and efficiency. The polymer is categorized as dendrimer polymer which are, as mentioned in the introduction, the most advantageous OLED polymers. The benefits of small molecule materials are combined with the ability of solution processability while maintain a high resistance

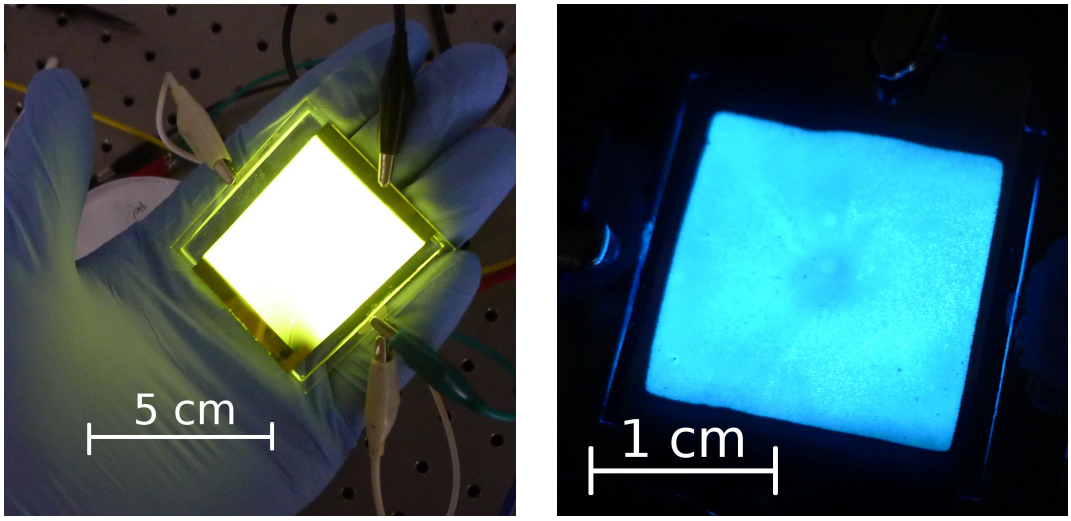

(a) PDY-132 OLED (b) SPB-02T OLED

Figure 4.1: Solution processed OLEDs produced in house from the two luminescent polymers purchased from Merck. Both devices are fabricated via spin-coating of polymer solution on a structured ITO coated glass substrate.

against oxygen and water. As our experiments have shown, the fabricated OLEDs can be operated in ambient conditions without any encapsulation for roughly one minute until, of course, the degradation process inhibits the light emission. The following section introduces the polymer and supports some literature references.

Lumogen Super-Yellow PDY-132

PDY-132 is a solution processable electro luminescent polymer for OLED application, which is commercially available from Merck. According to the data-sheet the lifetime at a light output of $100\,\mathrm{cd\,m^{-2}}$ is more than 220 000 h and the maximum power efficiency reaches up to $10\,\mathrm{lm\,W^{-1}}$. These values have been obtained by using a device stack consisting of ITO as a transparent conductive anode, a 20 nm thick layer of PEDOT:PSS, 80 nm PDY-132 and a cathode composed of 6 nm barium and 150 nm silver. The main difference compared to the devices fabricated in this thesis is the barium electron injection layer, which has been replaced by a 25 nm thick calcium layer due to the better technological experience at the our institute. Using calcium instead of barium is also suspected to be the main reason for the performance differences compared to the datasheet. The band diagram for the OLEDs

fabricated in this thesis is presented in Figure 4.2. The band diagram shows the hole confined at the bilayer interface due to an additional band step to the HOMO of the PDY and an electron right after tunneling through the triangular barrier formed by the biased LUMO of the PDY.

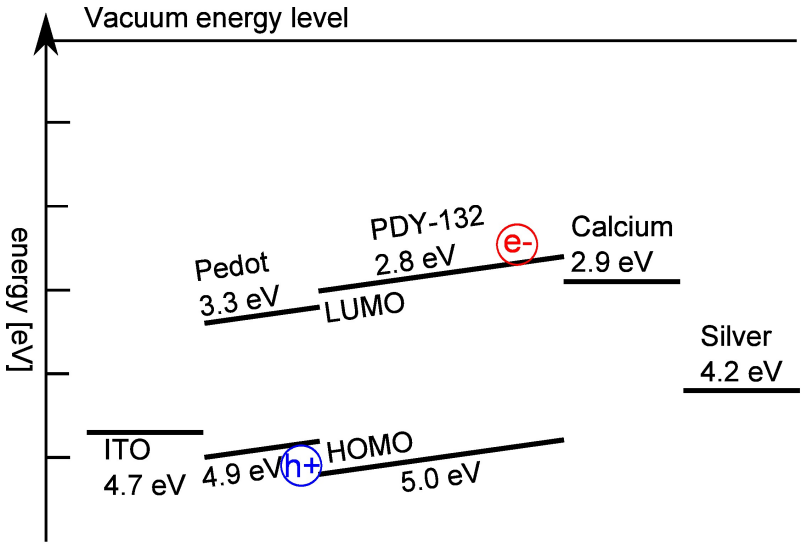

Figure 4.2: Band diagram of a bilayer OLED with PEDOT:PSS and PDY-132 under forward bias, as fabricated in this thesis. The ITO works as a hole (h-) injector and the bilayer confines the holes at the PEDOT-PDY interface in order to enhance efficiency and lifetime. On the cathode side the calcium layer helps to inject electrons (e-) from the silver by bending the workfunction to a lower level of 2.9 eV. Band values for PDY-132 are taken from [Baj10].

OLED Performance Parameters

The OLED has been fabricated with a 80 nm thick PDY-132 layer according to the fabrication procedure given in Section 3.1.1. The OLED features an ITO and PEDOT:PSS 4083 anode and a Ca/Ag cathode. The diode size is $3 \times 3\,\mathrm{mm}^2$.
Herein we compare the fabricated OLED with the data sheet values. For a simple comparison some standard parameters have been calculated from the luminance, current and voltage according to the formulas given in Section 3.3. The results of the electro-optic characterization are presented in Figure 4.3. The values are compared with the the data sheet. Figure 4.3a shows the current density of the

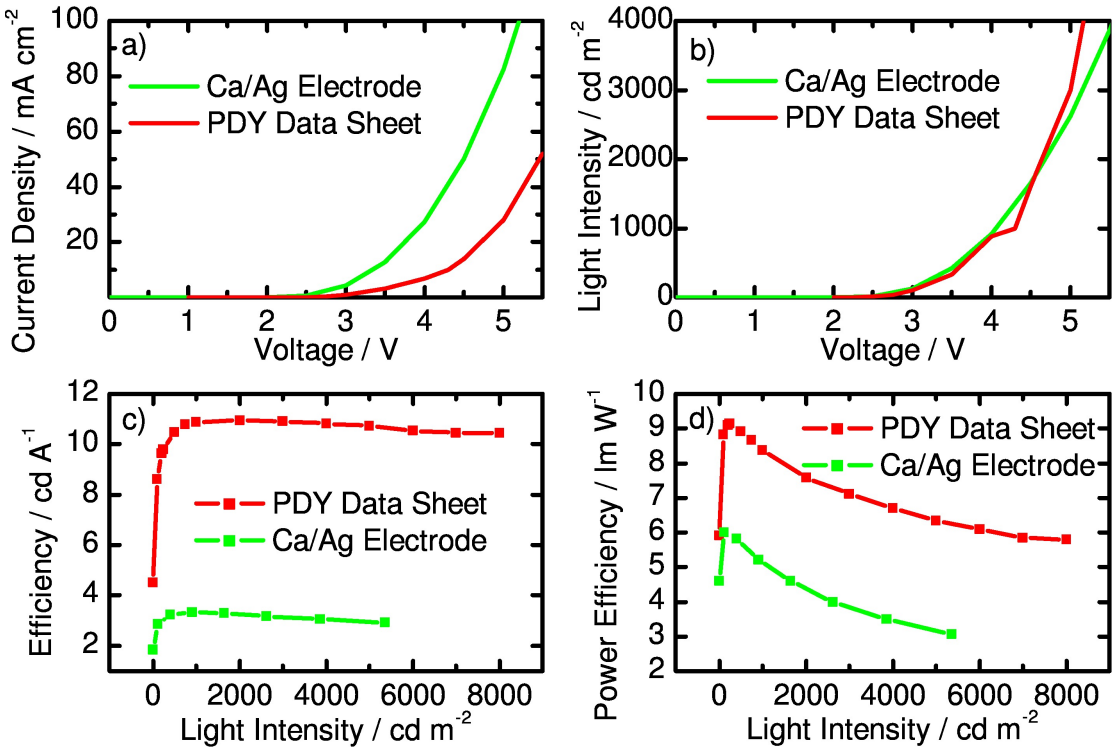

Figure 4.3: Experimental results of a $3 \times 3\,\mathrm{mm}^2$ diode compared to the values given in the PDY-132 data sheet. The devices have been fabricated as described in Section 3.1.1 with a layer sequence ITO-PEDOT:PSS-PDY-Ca-Ag. The devices from the data sheet however where fabricated with a barium layer instead of calcium. (a) Current density of both OLEDs showing no significant leakage current in the non-conducting range ($< 2.5\,\mathrm{V}$) and a roughly three times higher current density in the semi-conducting range compared to the data sheet. (b) The luminance of both devices, which is almost identical throughout the whole voltage range. (c) The efficiency graph shows an approximately four times higher efficiency of the barium devices, compared to the devices with a calcium hole injection layer. Calcium devices achieve approximately a light output of $3\,\mathrm{cd\,A^{-1}}$ for a luminance between $500\,\mathrm{cd\,m^{-2}}$ and $5000\,\mathrm{cd\,m^{-2}}$ (d) The power efficiency of the device is at maximum $6\,\mathrm{lm\,W^{-1}}$ at an intensity of $200\,\mathrm{cd\,m^{-2}}$ and decreases for higher brightness.

OLED which unveils that the current density of our device is roughly three times higher than the device shown in the data sheet. These results show that the injection and transport of charge carriers works even better than in the data sheet, however a look at the light output shown in Figure 4.3b shows that the light output is almost identical. The result from Figure 4.3a and 4.3b together suggest that charge carriers are exchanged between the electrodes without light emission. A possible pathway has been described in Section 2.1.3, where the hole migration via the HOMO level of the polymer is described, which leads to a recombination at the cathode without the emission of light, as the recombination takes place outside of the active polymer. The reason for this could be that the device in the data sheet used barium as electron injector material, which has a workfunction of 2.7 eV, which is slightly lower than the workfunction of calcium. Consequently, the efficiency and power efficiency depicted in Figure 4.3c and d show reduced efficiencies. The efficiency is the ratio between injected charge carriers and light emission, which is not taking into account serial resistances i.e. in the electrodes. The power efficiency in contrast takes into account serial resistances, injection barriers and the threshold voltage of the polymer. From these results we can conclude that the insufficient electron injection is the main reason for the low efficiency. However, as the luminous output is as high as the data sheet value, no further optimization was done and the devices were produced in the present configuration.

OLED Stability and Degradation

Besides the electro-optical performance of the OLEDs, the degradation is an important optimization parameter in order to achieve sufficient long lifetimes for several comparable experiments. Furthermore, the degradation during each experiment has to be much smaller than the observed response.
The degradation of numerous devices has been investigated with respect to the anode and cathode materials. Different encapsulation techniques have been tested and the devices have been characterized without encapsulation in a pure nitrogen atmosphere in order to prevent the glue itself to degrade the polymer. The OLEDs have been fabricated according to Section 3.1.1 and were measured right afterwards. Figure 4.4 shows the results of the first 10 hours of the degradation measurement.

One can see that the light intensity drops significantly within the first 30 min of operation, before degradation turns into an almost linear phase with a lower degradation rate. This drop can not be avoided, therefore all OLEDs have to be operated for at least 30 min before performing experiments in order to keep the degradation constant and low. The degradation rate is calculated in [% h^{-1}] according to Equation 4.1.

$$degradation = \frac{I(t) - I(t+1h)}{I(t)} \cdot 100\% \tag{4.1}$$

$I(t)$ is the measured light intensity at the time. The degradation is calculated for the linear part of the curve 5 h after the start of the measurement. The best performance was ascertained for the device with an ITO anode and a Ca/Ag electrode, however, the least degradation is possessed by the device that has a PEDOT anode and the same Ca/Ag cathode. For our experiments both anode materials are suitable, as the temperature response of the OLED lies around 20%, which is 40 times higher than the degradation of the ITO device and roughly 300 times higher than the degradation of the PEDOT device within one hour. It is worth mentioning that the ITO devices have indeed the better homogeneity since less layers are spin-coated on top of one another.

The encapsulation of the OLED plays a key role for the lifetime of the emitting polymer. Devices without encapsulation in ambient conditions can operate for roughly one minute, before degradation prevents the emission of most photons. To achieve longer lifetimes of several hundred hours, the active polymer has to be protected from oxygen and water by an encapsulation. We tested three different glues to glue the cover glass on top of the OLED and also measured the device in a pure nitrogen atmosphere to verify if the glue itself damages the OLED. The testet glues were (i) a two component epoxy glue, Araldite2011 (Huntsman), (ii) an UV cured glue for organic electronics, 9001-E-V-3.7 (Dymax) and (iii) an UV-hardening acrylate, OP-4-20632 (Dymax). Best performance and lifetime was observed for the encapsulation with Araldite2011, as the other glues degraded the OLED resulting in non-emissive regions, so called dark spots, which were visible to the bare eye. In order to measure the degradation promoted by the glue itself, the OLED lifetime has been measured in a pure N_2 atmosphere – Figure 4.4 (green line). It can be seen that the reference device (red line) does not significantly derive from the curve measured in the

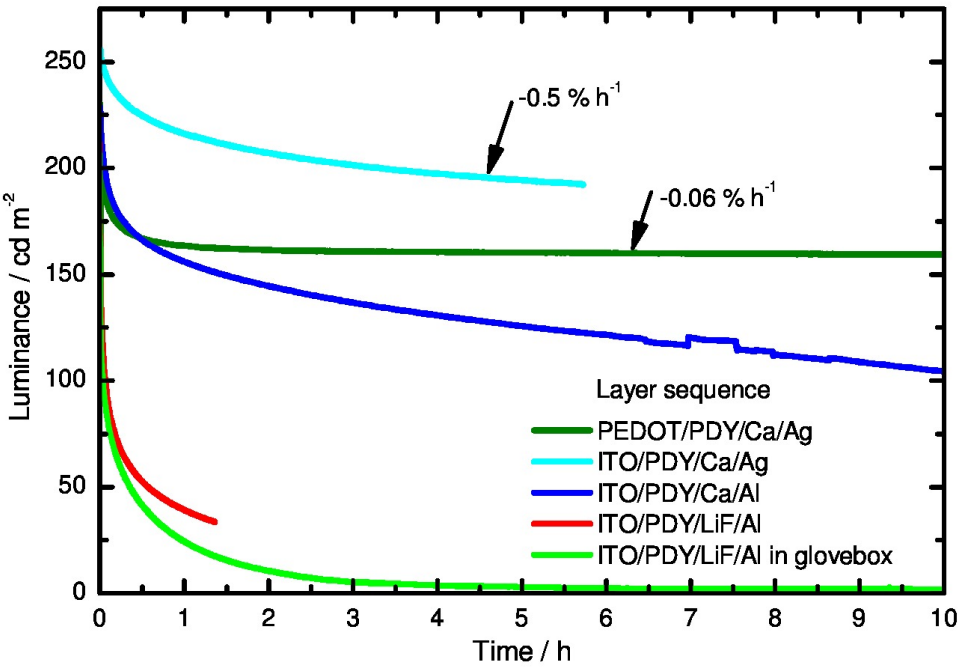

Figure 4.4: Measurement of the OLED operational lifetime for different electrode materials. Investigated were samples with a top electrode (cathode) of (red) 1 nm LiF / 100 nm Aluminum, (blue) 25 nm Calcium / 100 nm Aluminum and (cyan) 25 nm Calcium / 125 nm Silver. Additionally the encapsulation was tested by taking a reference measurement in the pure N_2 atmosphere in the Glovebox (green). For the combination with the best performance (Calcium and Silver, cyan) the anode material ITO has been replaced by the more stable PEDOT:ethylene glycol (EG) (olive). All samples were sourced by a constant current and the current was chosen in a way, that the starting luminance was roughly 250 cd m^{-2}. It was found that the Ca/Ag combination has best lifetime and efficiency results and that the PEDOT:EG electrode features with only $-0.06\,\%\,h^{-1}$, the smallest degradation.

N_2 atmosphere. We can assume that the encapsulation with Araldite2011 does not degrade the device, but protects the OLED physical and chemical damage.
The last degradation mechanism that shall be discussed in here is the intrinsic degradation of the polymer due to a number of processes which can be found elsewhere [Shi03]. Important parameters to keep the intrinsic degradation low are the current flow and the device temperature. High temperatures above 40 °C should be avoided or the exposure time to such temperatures should be kept as short as possible. The second factor is the current density, which promotes electron migration and heating which in turn harms the OLED. In our experiments the current was chosen so that the light output was just above 100 cd m^{-2} which was a good trade-of between measurement noise and degradation.

4.1.2 Temperature Tuning

The OLED has, as all semiconductors, a pronounced sensitivity to temperature. The dominating mechanism is the charge carrier mobility as mentioned in Section 2.1.3. A minor temperature effect is the electron-photon conversion efficiency. Both effects are investigated in the following two sections with respect to the light output and to the emission spectrum. The investigation of these phenomena is important, because in the proposed sensor, the OLED and the PC are coupled via a glass plate, which in turn couples both elements thermally. Since the working principle of the sensor is intensity tuning of light it is important to know how much is contributed by the OLED. All investigated temperature effects are fully reversible. A reference curve which has been taken, but was not plotted, before and after the experiment gave the same performance.

Luminance Tuning

Luminance tuning describes the light intensity changes caused by a variation of temperature. The luminance tuning of the OLED shown in Figure 4.5 has been observed using a Luminance meter (Mavo spot2) and thermo electric heaters as described in Chapter 3. Figure 4.5a shows the luminance of an OLED for voltages between 2 V and 5 V. The curve was taken at various temperatures ranging from 15 °C to 40 °C with an interval of 5 °C. It can be obtained from the graph, that the light inten-

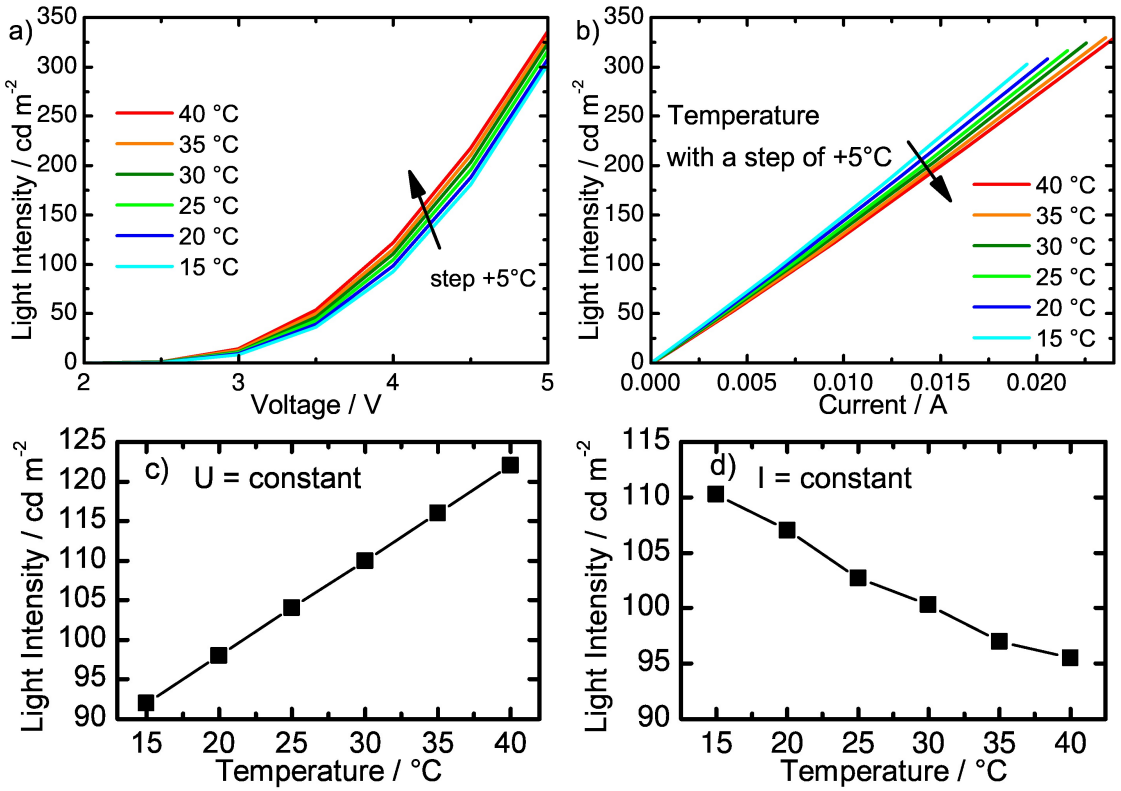

Figure 4.5: The graphs show the luminance of a PDY-132 OLED under different operating conditions. (a) Light intensity of an OLED plotted versus the driving voltage for temperatures from 15 °C to 40 °C. (b) Light intensity of the OLED versus current for different temperatures. (c) Light intensity at 3.9 V, showing a linear increase of intensity with the temperature of dL/dT=1.5 cd K^{-1}. (d) Light intensity for an OLED sourced at 7.5 mA showing a temperature response of dL/dT=−0.9 cd K^{-1}.

sity increases for higher temperatures. The increase in luminance is caused by the improved charge carrier mobility and injection and comes with an increased current density. This has also been reported by several other groups [Bäs11, Baj10]. Figure 4.5b demonstrates the luminous intensity depending on current. Here we observe, in contrast to the voltage driven devices, a decrease of light output as temperature increases. The electro-optical quantum efficiency suffers from the temperature increase lewhading to a decreased light output for the same current. The luminance at a constant voltage of 3.9 V is plotted in Figure 4.5c showing a linear slope throughout the whole temperature range. The slope equals $1.5\,\mathrm{cd\,K^{-1}}$ or as relative sensitivity $1.3\,\%\,\mathrm{K^{-1}}$. The opposing effect can be observed for the OLED sourced at a constant current of 7.5 mA in Figure 4.5d. Here we observe a linear decrease of the light output for increased temperatures. The slope is determined to $-0.9\,\mathrm{cd\,K^{-1}}$ or expressed as sensitivity $-0.55\,\%\,\mathrm{K^{-1}}$.

Spectral Tuning

The spectral tuning of the OLED has to be considered, because the IR sensor utilizes the stop-band shift of the 1DPC for the intensity tuning. This means that spectral shifts of the light source also can affect the light output of the proposed sensor. Again the single contributions of each component have to be investigated, in order to understand the whole device, make reasonable predictions and optimize the sensor. The OLEDs have been fabricated and measured with a monochromator as stated in the Experimental chapter, Chapter 3. The emission spectra of the OLED is plotted in Figure 4.6a to 4.6c for three different temperatures between 15 °C and 40 °C, which were supplied by (a) constant voltage, (b) constant current and (c) constant power. For a better comparison the graphs have been normalized to arbitrary units with the emission peak at 30 °C being 1 and the graphs withe different temperature scaled accordingly. Figure 4.6a shows the emission spectrum of the OLED at a constant voltage of 3.9 V demonstrating the increase of intensity for raised temperatures correlating with the peak intensity (inset) and the increase in luminance investigated in the preceding Section. The peak-wavelength lies around 546 nm at 30 °C and shifts slightly to blue/red for increasing/decreasing temperatures, respectively. Figure 4.6b shows the emission spectrum for the OLED sourced

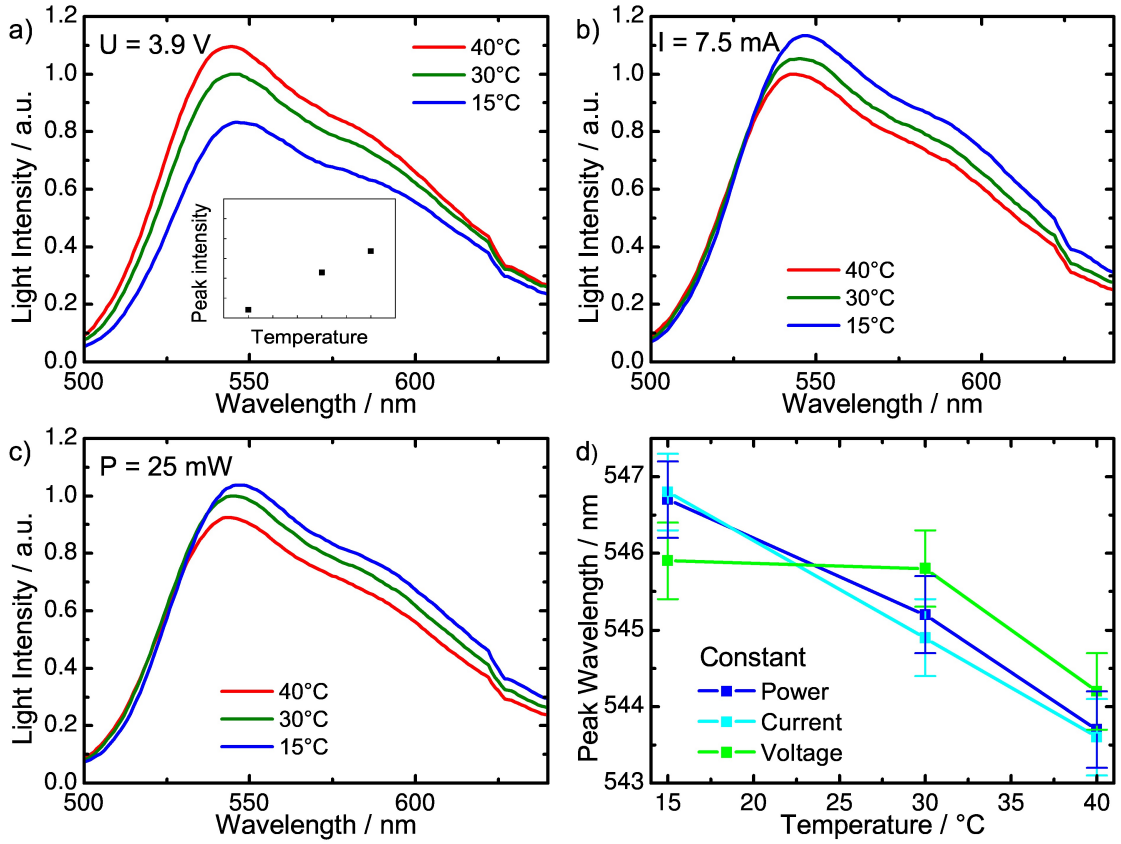

Figure 4.6: Spectral characterization of the OLED for Temperatures between 15 °C and 40 °C and using three different power supply modes. (a) At 3.9 V constant voltage. (b) At a constant current of 7.5 mA and (c) sourced with a constant power of 25 mW. (d) The peak position of all source modes, which has been interpolated to improve the monochromator resolution, showing a shift of $-0.1\,\mathrm{nm\,K^{-1}}$.

with a constant current of 7.5 mA. In accordance with the preceding investigation one can observe a decrease in light output for and increased temperature. Also for the OLED sourced with a constant current a red shift can be observed at increased temperatures. A new source mode has been used for Figure 4.6c where the OLED was sourced with the constant power of 25 mW which was realized with a remote controlled sourcemeter and a computer program that adapted the OLED current so that the power consumption was always 25 mW. It can be seen that also for a constant power the light output decreases for increased temperatures. This can be explained by the decreased efficiency. Simultaneously a red shift is observed for raised temperatures. All peak positions from all source modes have been plotted in Figure 4.6d for comparison. It can be calculated from the graph, that all source conditions result in the same red shift of roughly −2.5 nm for the temperature range between 15 °C and 40 °C or −0.1 nm/K. This information of the spectral shift of the OLED contributes valuable information to the sensor design, a further discussion is presented in Section 5.1.3.

4.1.3 Cavity Emitter

Narrow-band light sources can be of great interest for the application in sensors, as the sensitivity of the sensor can effectively be enhanced by a narrow band light source. In this section a micro-cavity OLED is presented, build from a sputtered 1DPC consisting of SiO_2 and SiN with a stop-band between 550 nm and 650 nm on a transparent glass plate. The reflection spectrum is shown in Figure 4.7c. A PEDOT electrode with a thickness of roughly 110 nm has been applied directly onto the sputtered 1DPC. The conductive PEDOT film served as the anode for the subsequent deposited OLED, experimental details can be found in Section 3. The micro-cavity was formed as depicted in Figure 4.7d between the silver electrode of the OLED and the sputtered 1DPC with a physical cavity length of roughly 210 nm. The optical confinement leads to a resonant cavity and enhances the stimulated emission. The resulting spectrum is plotted in Figure 4.7a showing the emission spectrum of a native OLED without cavity for comparison. Both devices are fabricated in the same way and a voltage of 5 V is applied. The cavity OLED in Figure 4.7a exhibits a cavity mode at 535 nm with an intensity roughly 1.7 times higher than the OLED

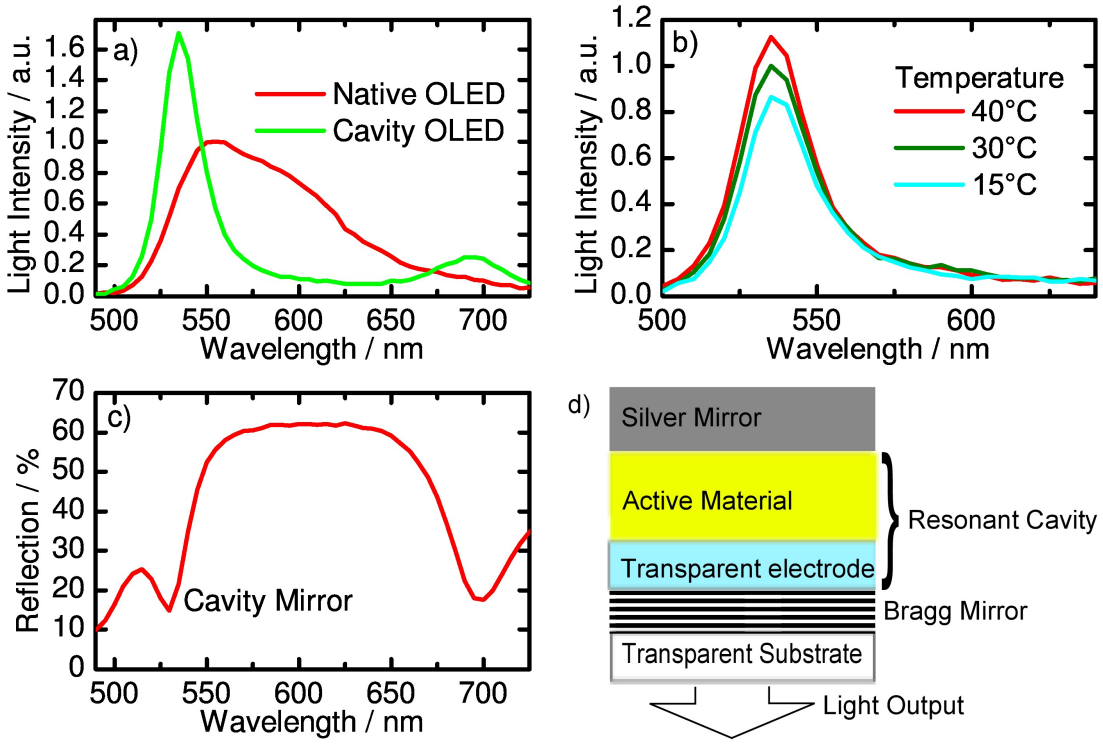

Figure 4.7: Characterization of the cavity-emitting OLED formed between a fully reflecting silver mirror on one side and a semi-transparent PC on the light out-coupling side. The OLED has been fabricated using a transparent PEDOT:EG electrode spin-coated directly on the BS with a thickness of 100 nm. (a) Comparison of the emission spectrum of a native OLED and a cavity OLED. (b) Characterization of the temperature response of the cavity OLED at 5 V. (c) The reflection spectrum of the Bragg mirror that was used. (d) Scheme of the setup showing the layer sequence and the resonant cavity between both mirrors.

at the peak wavelength and 2.5 times more intense than the OLED at the same wavelength of 535 nm. The band width has been determined by measuring the difference in wavelength between the two points on the emission spectrum which have exactly 50% of the peak intensity, the so called full width at half maximum (FWHM). The cavity OLED exhibits a FWHM of 25.5 nm which is only roughly one third of the band-width of the native OLED which is 92.3 nm. The temperature characteristics have been investigated in the range between 15 °C and 40 °C in the spectral range, plotted in Figure 4.7b. It can be seen, that the tuning is comparable to the native OLED from the preceding section, namely the peak intensity is tuned from 80% to 110% of the peak at 30 °C, roughly the same as the native OLED from Figure 4.6a. Now one could argue that the shifted and enhanced peak occurs only due to the filter characteristics depicted in Figure 4.7c. In order to demonstrate the photon confinement photographic images have been taken under monochromatic illumination in Figure 4.8. The OLED, that was used for the above experiments was the one which is shown in the lower left corner of the image. One can see that by illumination with a wavelength of 535 nm a dark field is formed on the area of the OLED (marked area). The reason can be found in the light confinement between the silver mirror and the PC and absorption by the polymer. In contrast Figure 4.8b shows the device under illumination at 525 nm which shows the same sample, but the diode in the lower left corner reflecting the monochromatic light. Instead two other diodes, which have their cavity mode at 525 nm are absorbing the light.

4.1.4 Carbon Nano-Tube Electrodes

The ITO electrode, which is commonly used comes with a series of disadvantages as discussed in Section 2.1.1. As a further step towards fully solution processable OLEDs exhibiting long lifetime and good efficiency, the attempt has been made to fabricate transparent electrodes from CNT solution. The fabrication of the CNT anode film with an underlying gold grid is described elsewhere [Abd12, Abd11]. The OLED was fabricated as described in the experimental section. The current voltage characteristics from Figure 4.9a show an almost linear response with an average resistance of 630 Ω. Though the OLED is emitting light, as the photograph in Figure 4.9b shows, the current of 15 mA is quite high. An explanation for the high

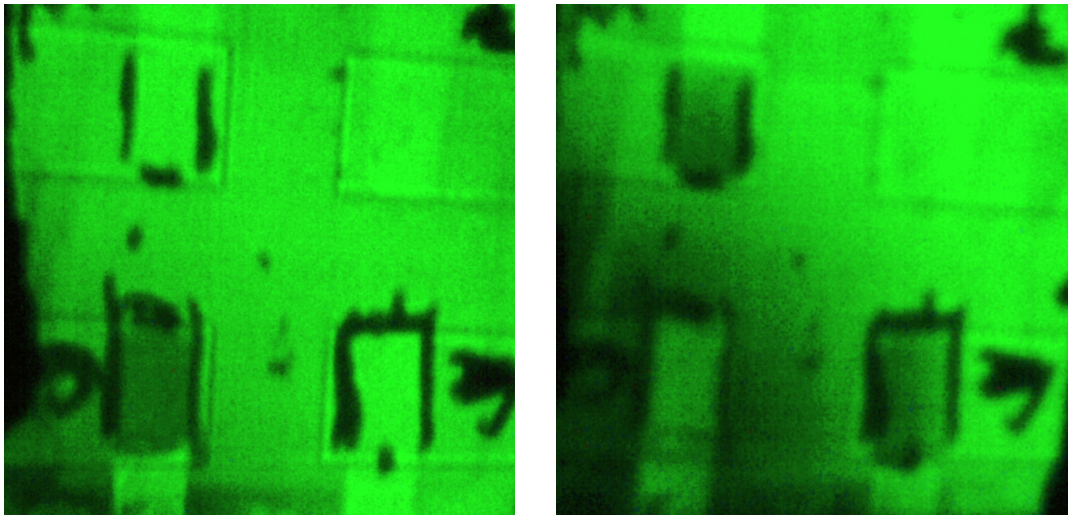

(a) At 535nm (b) At 525 nm

Figure 4.8: Photographic images of the cavity modes under monochromatic illumination by the monochromator (Cornerstone 260, Newport) at (a) 535 nm, showing a resonance of the OLED in the lower left corner, which was used for the spectrum in Figure 4.7 and (b) at 525 nm, with a resonance in the OLED in the upper left and lower right corner but not at the other ones. The images have been taken by projecting the monochromatic light that was reflected from the sample onto a screen.

current is an ohmic resistance in parallel to the OLED. Possibly the hole injection works very well and thus holes are directly conducted via the HOMO level of the polymer to the cathode. Another explanation can be the peak-to-valley roughness of the CNT films which was measured to be up to 60 nm. The rough surface can not be covered homogeneously by the OLED polymers, which short-circuits both electrodes. The investigation of these phenomena can help to optimize the OLED performance. The introduction of a hole blocking layer at the cathode side can help to improve the recombination efficiency and a smooth CNT film can help to reduce short circuits between the electrodes.

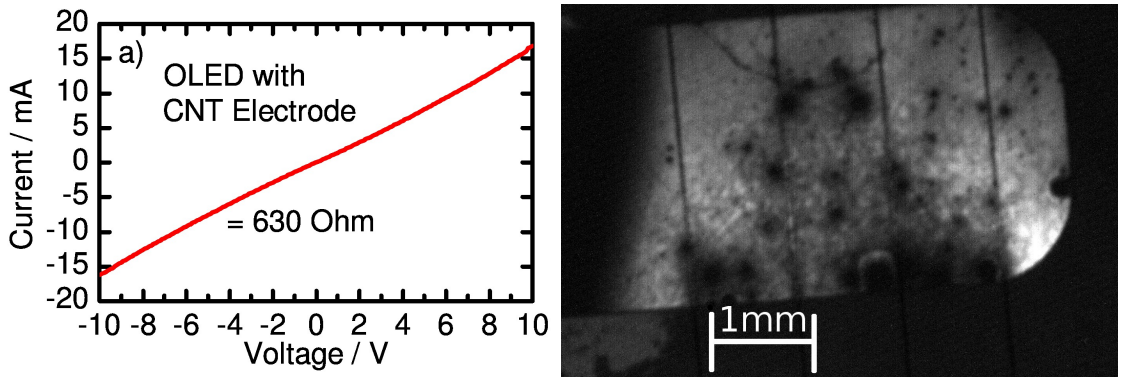

Figure 4.9: Characterization of the OLEDs with a spray coated CNT electrode supported by evaporated gold grid-fingers, instead of the ITO electrode. OLED. (a) U-I Characteristics of the fabricated device showing high leakage currents and a nearly ohmic behavior with a resistance of 630 Ω. (right) Monochrome image of the OLED at 10 Volt bias showing EL and the shadows of the grid-fingers.

4.2 Photonic Chrystals as Tunable Optical Filters

In this Section we shall first have a brief look at the fabrication of porous PC assembled from TiO_2 and SiO_2 nano-particle suspension. The fabrication of 1DPCs in this project was done by the group for functional nano-structures of Prof. Lotsch at the LMU. Three examples of the fabricated PCs are presented in Figure 2.7 showing 1DPCs fabricated with different layer-thickness and therefore a different structural color. Below the photograph the cross-section SEM micrographs are depicted show-

ing the porous nature of the 1DPCs.

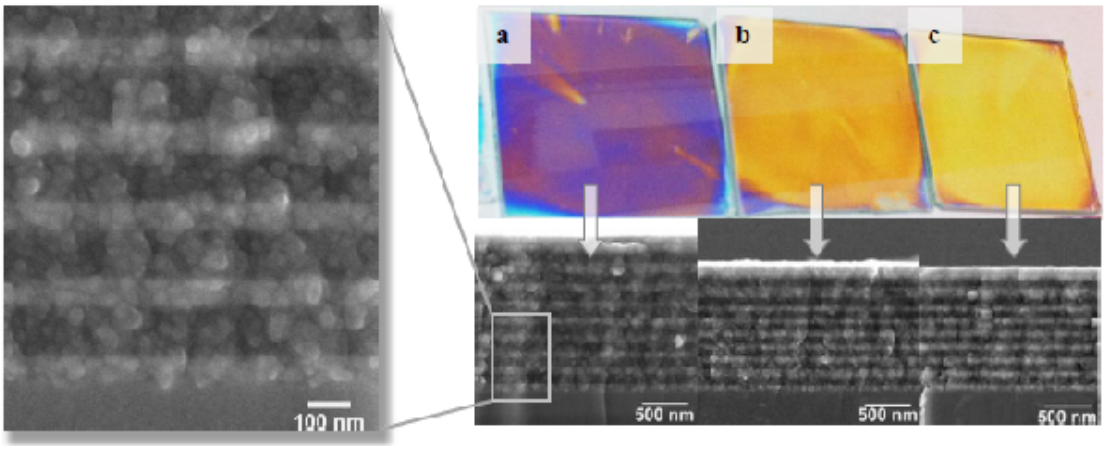

Figure 4.10: SEM images and photographs showing the relationship between the color of the TiO_2/SiO_2 1DPCs and the thickness of the layers spin-coated at (a) 2500 rpm, (b) 4500 rpm, and (c) 5500 rpm with an acceleration of 1500 rpm/s. Left: Magnification of the cross-section image (a) to demonstrate the porous morphology of the layers. The grainy or even blurred appearance is a typical feature of porous structures. Reprinted with permission from [Pav12a]. ©2013 American Chemical Society.

The focus of this section is the optical characterization of the single layers and the fully assembled PCs with respect to the temperature. Different grades of porosity as well as non-porous samples are investigated and the connection between sensitivity and porosity is drawn. The experimental results are accompanied by simulated structures using COMSOL Multiphysics in order to improve the understanding of the 1DPCs used.

4.2.1 Materials

The sol-gel method affords a relatively simple, fast and low-cost synthetic pathway to produce NPs for the assembly of 1DPCs with high optical and structural quality by spin-coating [Col08, Che99]. An intrinsic property of NP-based 1DPCs is the high porosity of the constituent layers, giving rise to versatile and multifunctional multilayer architectures which can be fabricated in a straightforward manner. In particular, BSs built from TiO_2/SiO_2 NP multilayers have already demonstrated

their response to chemical vapor and liquids [Cho06, Kob09, Lee06, Col08, Cal08, Fue08, Fue07]. An additional benefit of these systems stems from their self-cleaning properties provided by the photo-activity of TiO_2 under UV irradiation and the porosity- driven superwetting behavior ensuring the hydrophilic properties of such PCs [Wu07]. However, the impact of ambient conditions such as temperature and humidity on their optical response remains elusive in literature.

4.2.2 Temperature Tuning

The temperature response of single layers of TiO_2 and SiO_2 and the assembled PCs have been investigated in the temperature range from −165 °C up to 60 °C under various ambient conditions. Measurements have been taken in vacuum atmosphere, pure nitrogen and various relative humiditys (RHs) ranging up to 55%. The effect of the porosity of the PC on the temperature tuning has been investigated under various RH conditions to demonstrate the effective pore infiltration by ambient water vapor. The experimental results are accompanied by several simulations with values obtained from single layer characterization measured with an ellipsometer.

Thermo-Optic Coefficient in Vacuum

As it was discussed in Section 2.2 the PC is not olny sensitive to temperature, but also to ambient water vapor along with anything that can penetrate into the porous material. To exclude all effects resulting from infiltration, the PC has been mounted in a cryostat and the temperature characteristics have been taken under high vacuum conditions. Two windows provided the optical axis, so that the transmission could be measured with a monochromator. A sample with 10 bilayers of porous TiO_2 and SiO_2 has been used to measure the shift of the stop-band in the temperature range from −165 °C to 25 °C. The shift of the transmission spectrum is shown in Figure 4.11 in the spectral range from 400 nm to 600 nm. The inset of Figure 4.11 shows a zoom in on the spectral shift, demonstrating a shift of 3.3 nm for a temperature difference of 190 K, which gives an average shift of 17 pm K^{-1}. It can be seen that the shift on the red side of the stop-band (inset) is bigger than the shift of the blue side. This means, that the RI change of the TiO_2 is bigger than the RI change of the SiO_2 (for a more detailed explanation see simulations in Figure 4.17d), which is

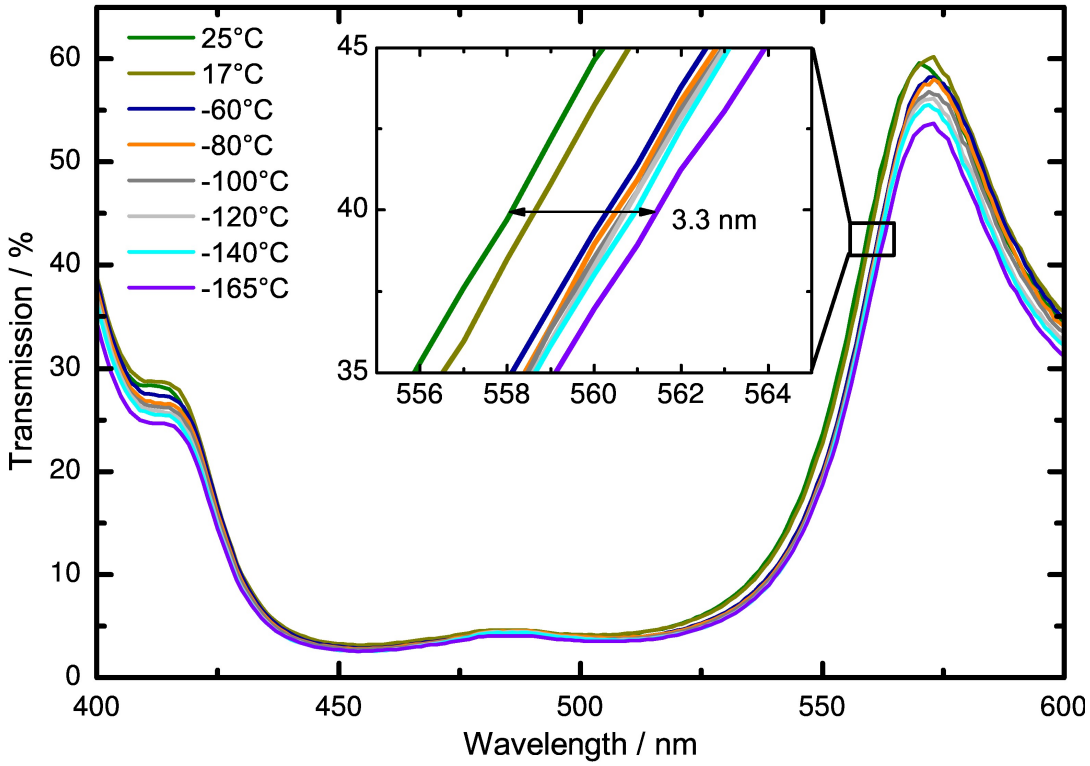

Figure 4.11: Transmission of the PC in a vacuum atmosphere inside the cryostat for the spectral range from 400 nm to 600 nm showing both sides of the stop-band. The inset demonstrates the shift of the photonic stop-band which is 3.3 nm for the whole temperature range of 190 K. The average shift over the whole range is 17 pm K^{-1}. The transmission was measured through two plastic windows of the cryostat. The temperature was measured by a PT100 thermometer glued directly on the sample.

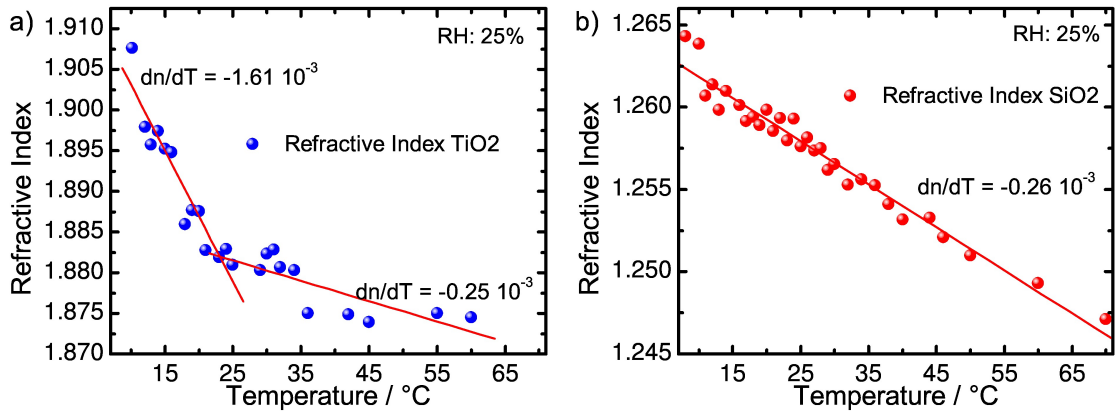

Figure 4.12: RI of a single layer (a) TiO_2 and (b) SiO_2, measured by spectroscopic ellipsometry under ambient conditions at a relative humidity of 25%. (a) the RI changes strongly in the sub-room temperature range from 10 °C to 25 °C, a moderate change can be observed in the temperature range from 25 °C to 60 °C. A slightly different picture is drawn by the RI of (b), the SiO_2 layer. A linear change of RI can be observed throughout the whole range from 8 °C to 70 °C.

in good agreement with the TOC values that we have found in literature. The TOC of TiO_2 is roughly one order of magnitude bigger compared to SiO_2. From these first vacuum measurements we can obtain the pure effect of the TOC in the given temperature range. In the following the influence of ambient conditions on the temperature tuning is investigated.

Thermo-Optic Coefficient in Ambient Conditions

The TOC and the subsequent RI change is the underlying effect of the observed stop-band shift. It is therefore important to characterize the RI changes in order to design a sensitive PC with big and linear response. The investigation of the TOC has been conducted using single films of porous TiO_2 and SiO_2 fabricated from a Sol-gel as described in Section 4.2.1. The RI was determined via spectroscopic ellipsometry as described in Section 3.2.2. Figure 4.12a and 4.12b show the RI for a 66 nm thick film of TiO_2 and and a 111 nm thick film of SiO_2 for a temperature range from 10 °C to 60 °C, respectively. The characterization has been done under ambient conditions at a RH of 25% at 20 °C room temperature. The TOC TiO_2 for temperatures

below 25 °C, is measured to be dn/dT = $-1.61 \times 10^{-3}\,K^{-1}$. The measured TOC is roughly one order of magnitude bigger than the literature value of $-1.77 \times 10^{-4}\,K^{-1}$ [Gül02]. It is noticeable, that the TOC for temperatures above 25 °C is only dn/dT = $-0.25 \times 10^{-3}\,K^{-1}$. The high variations of the TOC are attributed to ambient water vapor which is, adsorbed into the pores as described in Section 2.2.1. For the RI of SiO_2 depicted in Figure 4.12b we observed a linear decrease between approximately 12 °C and 60 °C. The TOC was determined to be $-2.52 \times 10^{-4}\,K^{-1}$. Thus, in contrast to the majority of literature sources that report positive TOC values for SiO_2, we measured a negative TOC. However, Müller et al. also observed a negative TOC of $-1.92 \times 10^{-5}\,K^{-1}$ for SiO_2 in an intermediate buffer layer between Si substrate and a metal oxide film and attributed such behavior to the difference in the TEC of the silicon substrate and amorphous silica [Wie09]. According to the above-mentioned report, the temperature-induced extension of bulk silicon substrate causes stretching of the SiO_2 film, thus, reducing the RI of the film. The TOC of SiO_2 determined in our study has a roughly 13 times higher value, which can be explained by the additional influence of the humidity effect which is described in this section.

Effect of Humidity and Porosity on the Thermal Tuning

The investigation of thermal tuning has been conducted using two PCs consisting of the same materials, TiO_2 and SiO_2, but fabricated differently: (i) a dense, sputtered PC and (ii) a porous PC spin-coated from NP suspension. The sputtered PC does, as SEM pictures have shown, not possess a significant porosity, in contrast, the the spin-coated sample features pores that allow for penetration with water molecules. The sputtered PC is made of 8.5 bilayers of TiO_2 and SiO_2 with a thickness of 60 nm and 90 nm and a RI of 2.41 and 1.55, respectively. The spin-coated sample had 8.5 bilayers of TiO_2/SiO_2 with a layer thickness of 55 nm/90 nm and a RI of 1.92/1.46, respectively. A detailed documentation of the fabrication procedure is given in Section 3.1. Both PCs, possessing a similar photonic stop-band have been tuned in a temperature range from 15 °C to 60 °C and under different atmospheric conditions, see Figure 4.13. It can be seen, that the porous PC (right side) increases the shift for the given temperature range from 1 nm in the absence of humidity and 21.2 nm at a RH of 55%. The shift of the dense PC is, in contrast the porous structure smaller

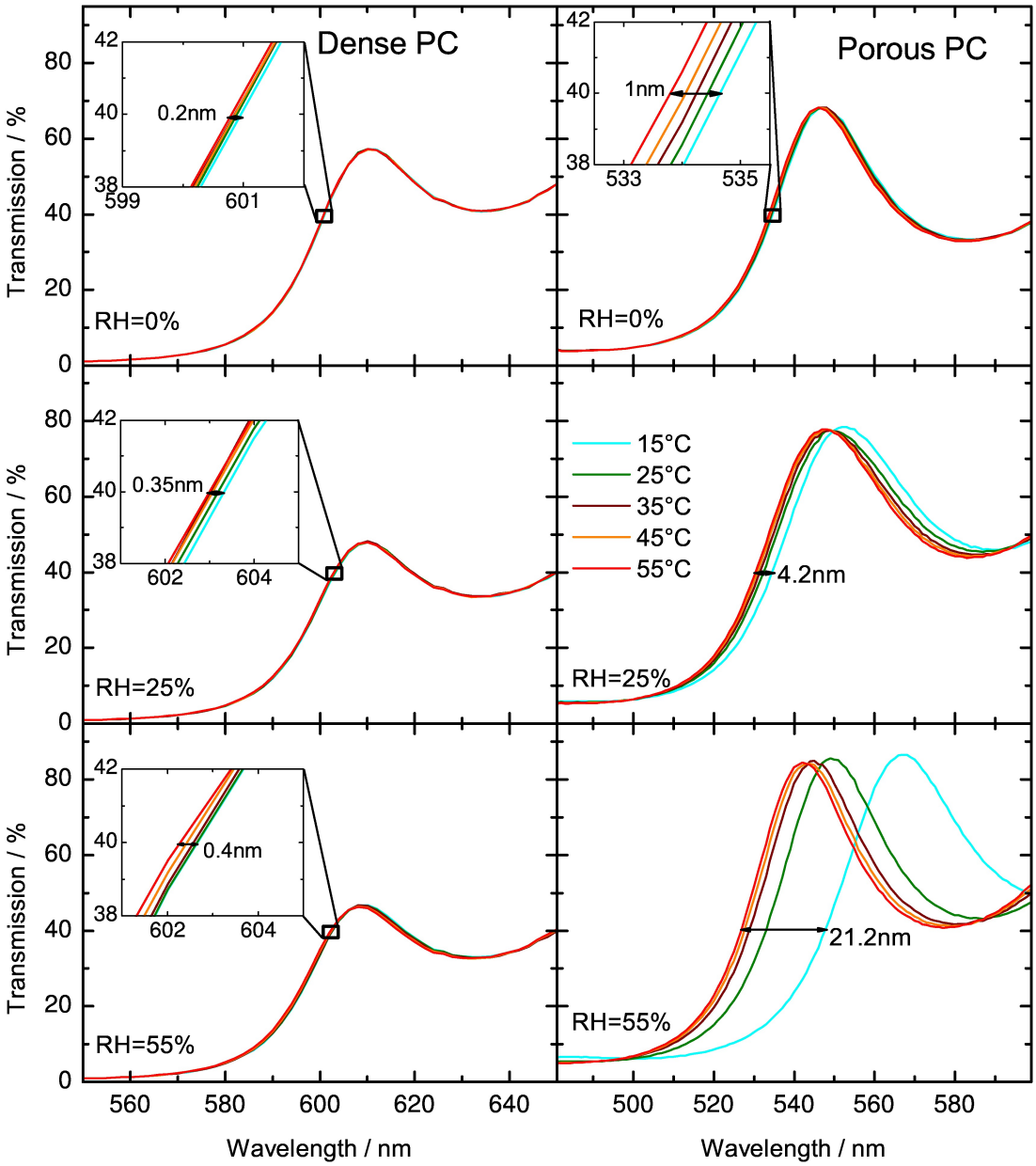

Figure 4.13: Transmission spectrum of two different PCs for temperatures between 15 °C and 55 °C at three different ambient conditions. The graphs on the left side present a sputtered, dense PC which is not penetrated by water molecules. The measurements at 0%, 25% and 55% RH show only slight variations in the photonic stop-band shift from 0.2 nm to 0.4 nm. On the right side the transmission spectrum of a porous PC fabricated from NP suspension is presented. The increase of the photonic stop-band for the variation of the RH from 0% to 55% increases the shift from 1 nm to 21.2 nm.

and less dependent on ambient conditions. The shift is only 0.2 nm in pure nitrogen atmosphere and 0.4 nm at a RH of 55%. These results show that the ambient water vapor increases the shift by water adsorption in the pores. The porosity plays a key role, as it makes the material accessible to humidity.
Figure 4.14 shows the shift of the porous PC under three different humidity conditions. From Figure 4.14 it becomes evident that the temperature response is non-linear as increasingly larger shifts are observed at lower temperatures. It is likely that the shift below 30 °C is dominated by water adsorption since the non-linearity is only observed for porous structures in a humid atmosphere. Above 30 °C the water plays a less important role and the shift is governed predominantly by the TOE. We can therefore describe the thermal tuning of the PC as the superposition of the changes in temperature and RH during heating (cooling) in the regime above 30 °C. The linear approximation of the temperature response in the range between 30 °C and 60 °C gives a shift of −0.05 nm/K, −0.08 nm/K, and −0.12 nm/K for 25%, 45%, and 55% RH, respectively. Below 30 °C we observe a non-linear shift behavior showing stronger response for the experiments conducted with higher humidity. Humidity-enhanced thermal tuning causes shifts of the transmission spectra by up to −1.93 nm/K as compared to 0.35 nm/K calculated for typical non-porous Si/SiO_2 PCs [Ban09]. The dew points are 11 °C for ambient air at 55% RH, 7 °C for 45% RH, and 0 °C for 25% RH.

Hysteresis The assumption of water adsorption in the pores makes us expect a hysteresis when recording the optical response along a full heating and cooling cycle. Therefore, the optical response of a PC with 9 bilayers (TiO_2 (60 nm)/SiO_2 (110 nm)) was studied at 25% RH by cycling the temperature up and down in steps of 2 °C while measuring the transmission value at a constant wavelength (610 nm). After each set-point temperature was reached, the sample was kept at the temperature for 60 s for thermal equilibration before the measurement was taken. As can be seen in Figure 4.15, a hysteresis is indeed observed over more than five cycles. Heating-cooling cycles recorded with longer delay times up to 900 s do not significantly change the shape of the hysteresis, thereby suggesting that the water adsorption/desorption kinetics are fast and not responsible for the observed hysteresis. On the other hand, measurements under nitrogen atmosphere and 0% RH show no hysteresis,

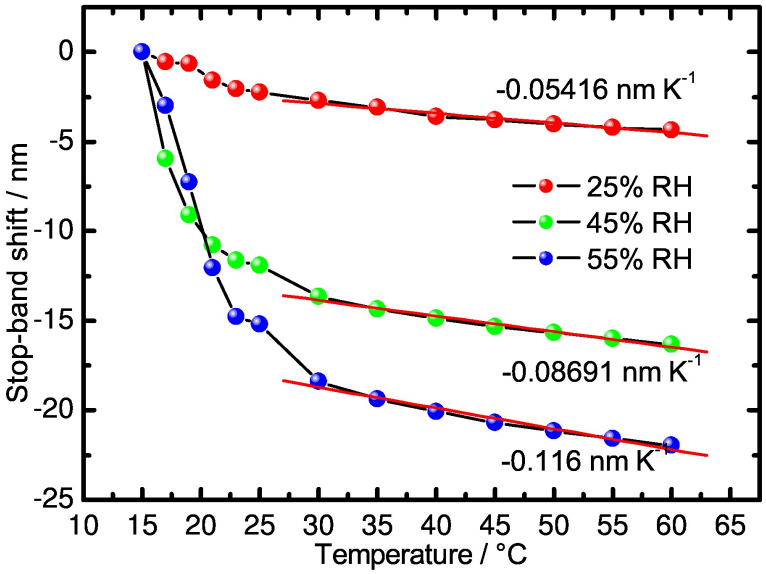

Figure 4.14: Wavelength shift as a function of temperature at different RHs. The shifts were obtained by extracting the wavelength values at 50% transmission from the spectra presented in Figure 3 for the temperatures between 15 °C and 60 °C at various RHs. The shifting behavior is strongly dependent on the RH. For temperatures above 30 °C the temperature response is linear. The linear approximation between 30 °C and 60 °C shows the rate of the shift being equal to −0.05 nm/K, −0.09 nm/K, and −0.12 nm/K for RHs 25%, 45%, and 55%, respectively. Below 30 °C we observe the shift to be non-linear, showing a higher slope of up to −1.93 nm/K.

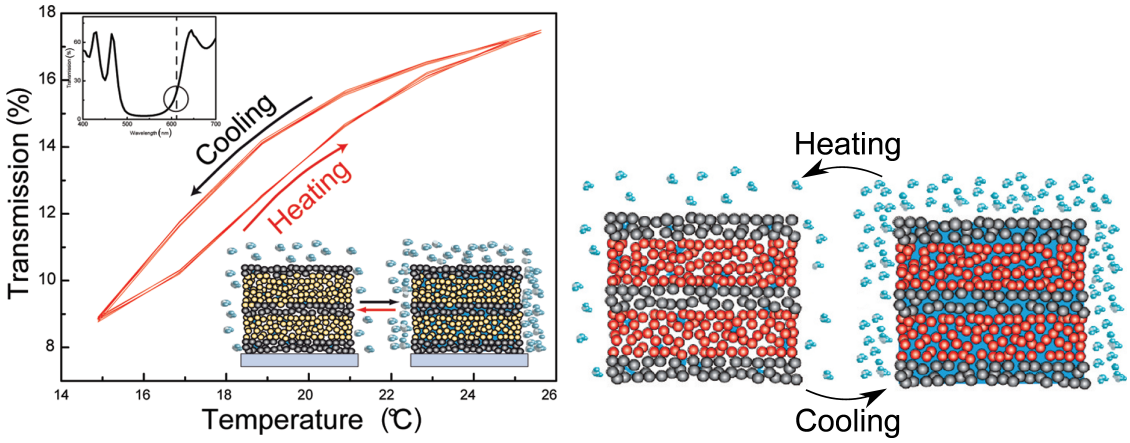

Figure 4.15: Hysteresis of a PC with 9 bilayers of TiO_2 (60 nm) and SiO_2 (110 nm) illuminated with monochromatic light at 610 nm. The heating and cooling curves where recorded at ambient conditions of 25% RH and the temperature was varied between 15 °C and 25 °C. The wavelength was chosen to be at the red side of the photonic stop-band at a transmission of 20%. The temperature was cycled five times with an equilibration time for each temperature of 60 s (red line) and for 900 s (black line). Reprinted adapted with permission from [Pav12c]. ©2013 SAGE Journals.

thus indicating that humidity is required in order for the hysteresis to occur. We assume that the hysteresis is due to capillary condensation of water into the textural meso-pores of the layers resulting from the packing of the NPs, as is observed in similar thin film systems consisting of NPs [Dem10]. In general, however, it can be noted that the maximum opening of the hysteresis loop is only about 1.5% in transmission at 25% RH and hence results in only a moderate, yet reproducible correction of the shifts expected for a purely thermo-optic response. The results, as well as graphs and text are published elsewhere [Pav12b].

Simulation

For a better understanding of the photonic stop-band shift simulations have been conducted and compared with the experimental results. The layer thickness of the fabricated PC was measured with cross-section SEM and the RI was obtained from the previously, in Section 4.2.2, conducted characterization of the single layers. The thickness of the TiO_2 and SiO_2 was measured to be 60 nm and 93 nm, respectively. The RI values where taken from the measurements presented in Figure 4.12. The thermal expansion of the layers was not simulated. We used COMSOL Multiphysics to simulate the PC with 8.5 bilayers and compared to the experimental results in Figure 4.16. A detailed explanation on the simulation procedure can be found in the in Section 3.3. The simulated graph shows a total shift of 5.8 nm for the entire temperature range from 15 °C to 60 °C while the experimental graph (inset) shows only a shift of 4.4 nm in the same temperature range. A better matching between experimental and simulated results is observed in the temperature range from 15 °C to 25 °C with a shift of 2.3 nm for the experimental and 2.4 nm for the simulated shift. These results show that the shifting can be simulated when the response of the single layers is known and all layers are simulated with the single layer response. This implies that all layers are affected by the temperature change and infiltrated by water homogeneously. Thermal expansion, in this case, can be neglected as the TOC and the water adsorption dominate the photonic stop-band shifting process.

In contrast to the previously presented simulation to match the experimental result a more systematic approach has been done in order to understand the photonic

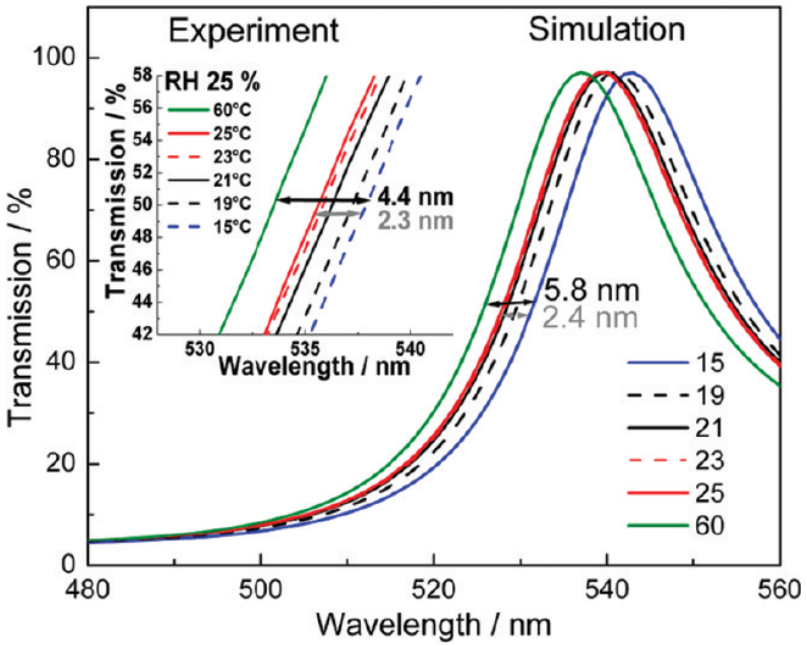

Figure 4.16: Simulated transmission of the PC with 8.5 bilayers of TiO_2 and SiO_2 in the spectral range from 480 nm to 560 nm. The RI has been taken from the single layer characteristics determined by spectroscopic ellipsometry and presented in Figure 4.12. In order to match the results from the measurement shown in the inset, the values of the thickness where measured from the experimental sample using cross-section SEM and found to be 60 nm for TiO_2 and 93 nm for SiO_2, respectively. Reprinted with permission from [Pav12a]. ©2013 American Chemical Society.

stop-band shift and the correlation between the optical parameters of the single layers. We simulated a 1DPC with 9 bilayers of TiO_2 and SiO_2 and varied but one parameter, which was either the RI or the thickness of one of the materials. The simulation was done using the MATLAB script from Appendix A.3.2 and COMSOL as described in Section 3.3. The variation of the layer thickness between 100 nm and 140 nm for SiO_2 and between 70 nm and 110 nm for TiO_2 is presented in Figure 4.17a and 4.17b, respectively. It can be seen from the figure, that the center wavelength of the stop-band moves to the red with increasing thickness of one of the layers. Both slopes, the red and the blue one, are moving simultaneously to the red if the thickness of one of the materials is changed. In both cases the slope on the blue side changes less than the slope on the red side leading to a small change in the width of the stop-band. A different behavior can be observed for the variation of the RI index where not only the optical thickness changes, but also the RI contrast and therefore the transmission and the width of the stop-band. In Figure 4.17c and 4.17d the RI variation between 1.1 and 1.5 for SiO_2 and between 1.7 and 2.1 for TiO_2 are presented. In both cases the stop-band width is reduced by 50% and transmission is decreased by 10%. It is worth mentioning that the RI changes of TiO_2 predominantly effect the red side of the stop-band and changes in the RI of SiO_2 predominantly effect the blue side of the stop-band.

4.2.3 Chemical Tuning

As discussed before the optical thickness of the PC can be altered by adsorption of molecules. As a first demonstration of the sensitive PC a photographic image showing the PCs colorimetric change upon exposure to humidity is presented in Figure 4.18. The PC was fully backlighted with a yellow OLED and two pictures where taken, one in ambient conditions at approximately 25 % relative humidity and the second short after exposure to human breath (approximately 100 % RH). The shift of the stop-band can be seen by the naked eye as a colorimetric change from ruby red to deep green. Circular variations in color and response can be seen that originate from spin coating irregularities. Especially in the center of the PC the response can barely be seen with the presented illumination. However, as the diodes for the detection of the stop-band are located at the side, at a distance of 5 mm from

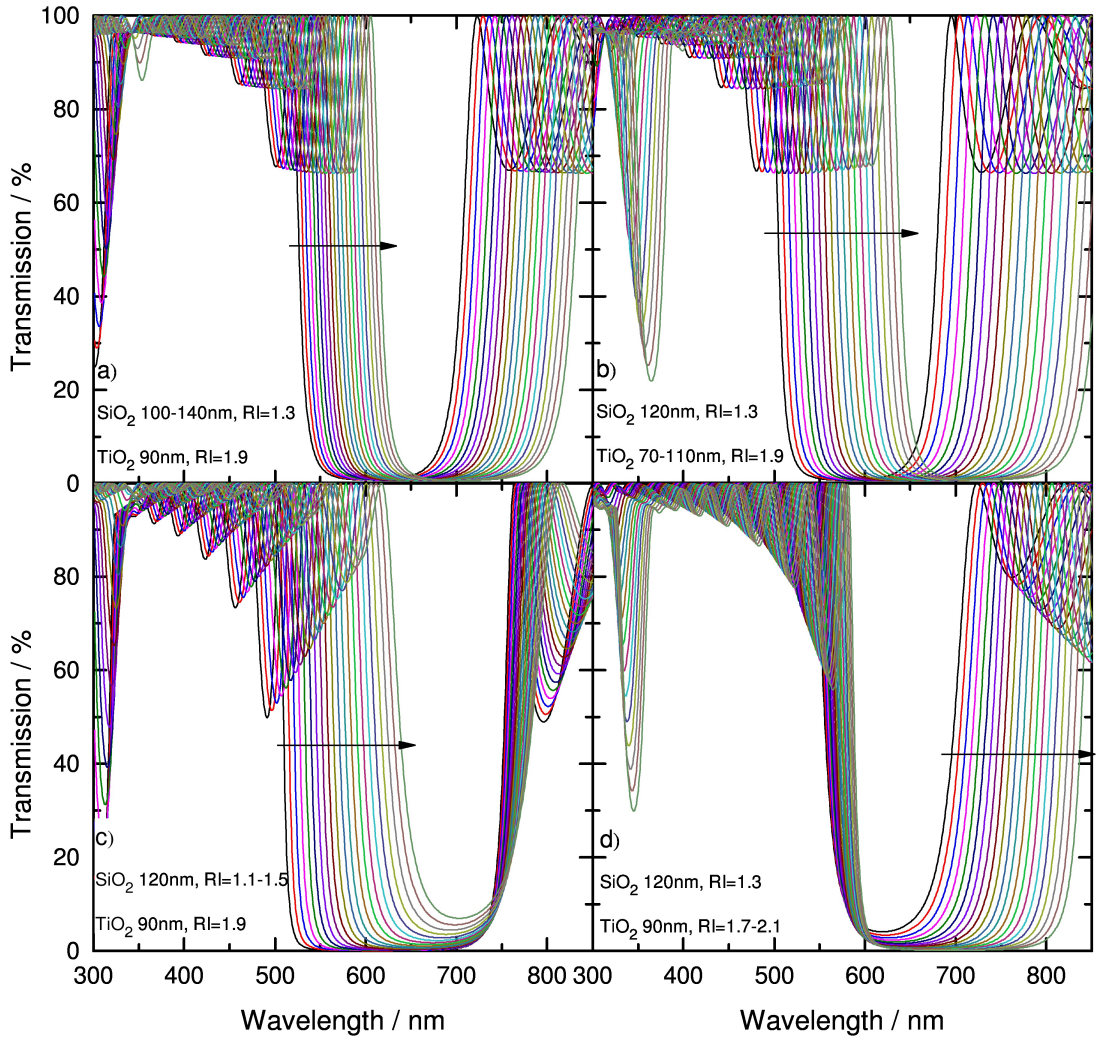

Figure 4.17: Simulated transmission spectra of a PC with 9 bilayers, starting with the TiO_2 layer, and consisting of various combinations of (a) TiO_2 layers of 90 nm/RI = 1.9 and SiO_2 layers with RI = 1.3 and thicknesses varying from 100 nm to 140 nm. (b) TiO_2 layers with RI = 1.9 and thicknesses varying from 70 nm to 110 nm, and SiO_2 layers of 120 nm/RI = 1.3. (c) TiO_2 layers of 90 nm/RI = 1.9 and SiO_2 layers of 120 nm with RI varying from 1.1 to 1.5. (d) TiO_2 layers of 90 nm with RI varying from 1.7 to 2.1, and SiO_2 layers of 120 nm/RI = 1.3. The black arrow indicates the direction of the stop-band shift as the layer thickness or RI increases.

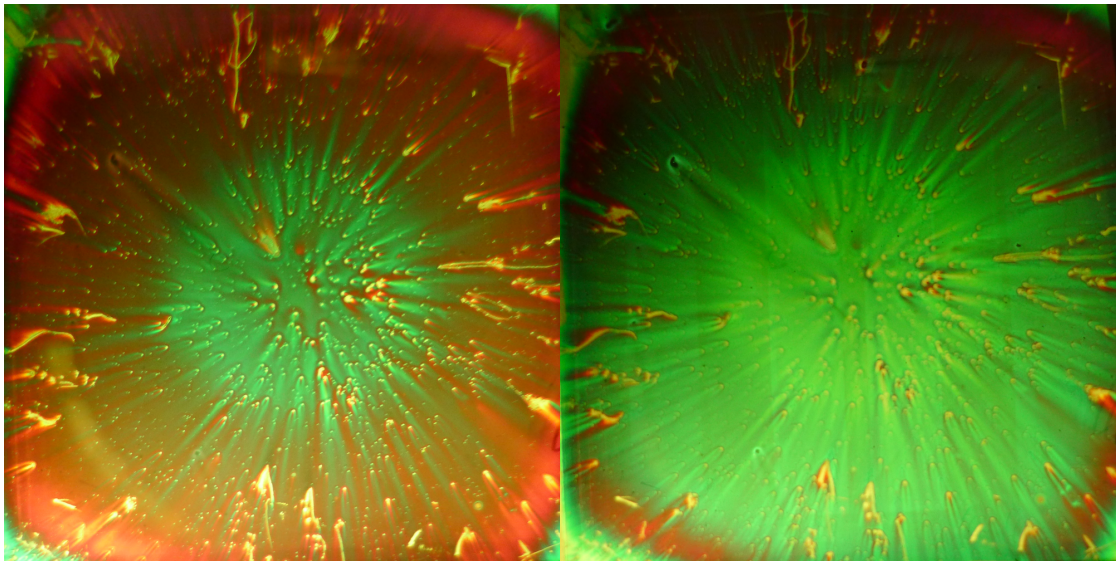

Figure 4.18: Image of the PC with illumination by a yellow OLED from the back, showing the response to humidity under ambient conditions. (a) at a RH of approximately 25 % and (b) after breathing on the surface withe a RH of approximately 100 %. The transformation of the two states happens within seconds.

the border a clear response can be expected for the integrated sensor described in Section 5.2.

The reflection spectrum of the photonic stop-band upon exposure to ethanol vapor in nitrogen gas mixture at various ethanol concentrations is shown in Figure 4.19a. As predicted, the photonic stop-band shifts to the red because the pores, that were formerly filled with nitrogen are now filled with ethanol instead. The nitrogen which has a RI of approximately 1 was replaced by ethanol having a RI of 1.36 which causes all layers to increase their optical thicknesses. The ethanol concentration p/p* has been calculated according to Section 3.2.7. The measured overall shift between pure nitrogen (p/p*=0%) and ethanol saturated nitrogen (p/p*=100%) exposure was measured to be 23.4 nm. Figure 4.19a shows the stop-band when exposed to different ethanol concentrations performing a shift of 23.4 nm. Another effect that can be observed is the decrease in reflectivity for increasing ethanol concentrations. The decrease of reflectivity originates from a decreasing RI contrast between the TiO_2 and SiO_2 layers due to either a different grade of porosity or an unbalanced

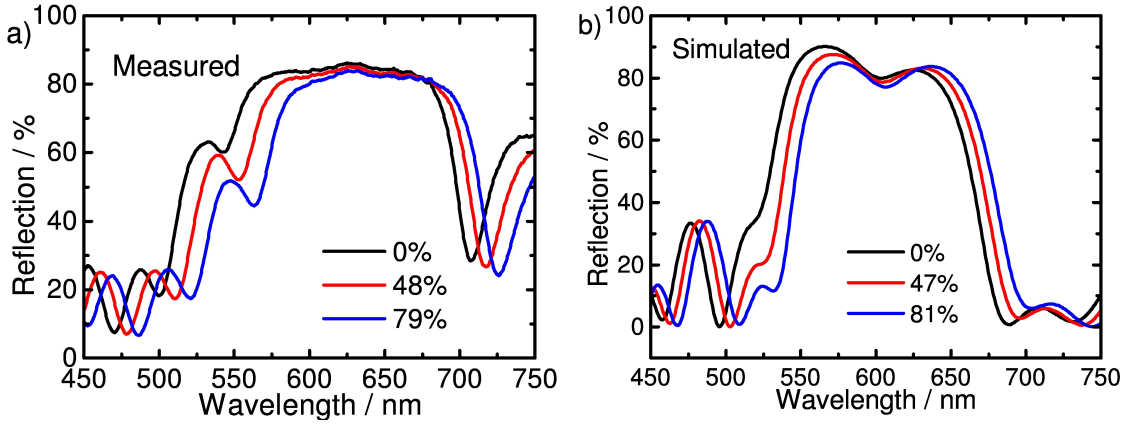

Figure 4.19: Transmission spectrum of the PC with 6 bilayers of SiO_2 and TiO_2 for different ethanol saturations p*. (a) The transmission curve measured with a spectrometer. (b) The Simulated transmission, for RI values obtained by spectroscopic ellipsometry.

filling with ethanol. From ellipsometry measurements we know that the RI index of SiO_2 increases more pronounced compared to TiO_2 which decreases the RI contrast. The RI values of the SiO_2 and TiO_2 at the ethanol vapor saturation of 0%, 47% and 81% have been determined by spectroscopic ellipsometry and the thickness has been measured using SEM micrography. Figure 4.19b shows the simulation of a 6 bilayer SiO_2/TiO_2 structure on a glass substrate performing a shift of 19.4 nm for an ethanol saturation (p/p*) of 81%. The value is comparable to the shift of 23.2 nm we measured for an ethanol saturation of 79%. The measurements where taken under slightly different process conditions, which resulted in slightly different saturation ratios for the same mass flow. However, from these results we can draw the conclusion that all layers are fully infiltrated by the ethanol after being exposed for 60 seconds. Other simulations have shown, that a partial infiltration decreases the shift. The magnitude of the shift decreases by roughly 50% for a halv infiltrated PC, i.e. only the first 3 bilayers are infiltrated.

4.3 Organic Photodetector

The OPDs presented herein can be used to detect the stop-band position of the PC by measuring the transmitted light from the OLED. Organic semiconductors are

generally sensitive to temperature as the charge carrier transport phenomena (discussed in Section 2.1.3) are partially temperature induced processes. For the future integration in sensing devices, especially for IR sensing, the temperature response of the OPD must be known in order to produce a good sensor design. The OPDs were fabricated as stated in Section 3.1.2. A general electro-optic characterization of the OPD is provided in Section 4.3.1 and an analysis of the temperature sensitivity is conducted in Section 4.3.2.

4.3.1 Electro-Optic Characteristics of the OPD

Basic electro-optic studies where conducted to demonstrate the OPDs sensitivity to light with respect to the applied voltage and wavelength of irradiation. In Figure 4.20a the current-voltage characteristics are given under illumination and in darkness. The sample was irradiated with a halogen lamp at a distance of 40 cm

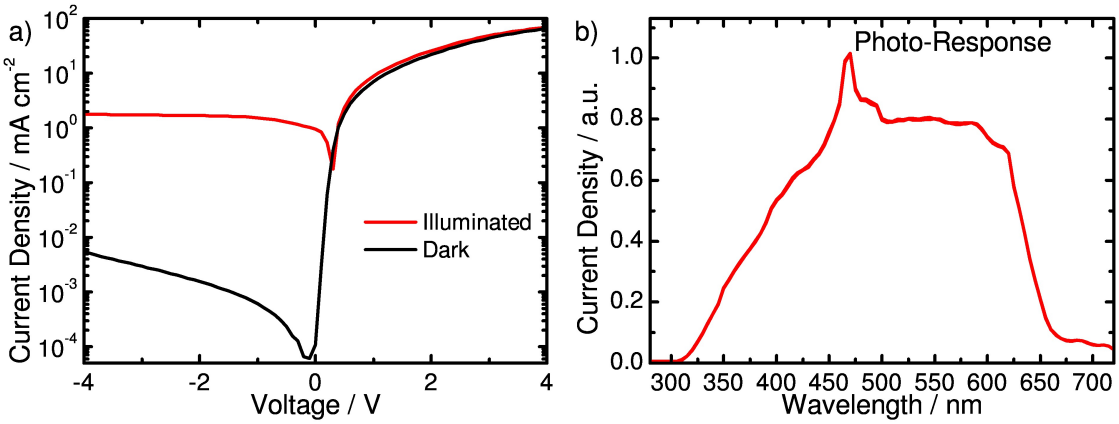

Figure 4.20: Response of the OPD fabricated from P3HT/PCBM blend. (a) current-voltage characteristics in darkness and under illumination with a halogen lamp of 100 mW cm^{-2} between −4 V and 4 V. (b) Spectral response of the photo induced current at −2 V bias in the wavelength range from 250 nm to 750 nm. The peak at 470 nm is caused by the Hg-arc lamp, since the spectrum was not calibrated for this measurement.

with a light intensity of 100 mA cm^{-2} resulting in an on-off ratio (the ratio of the photo-current under illumination vs. leakage current in darkness) of roughly 350. The spectral response of the OPD is given in Figure 4.20b showing a broad sensitivity between 350 nm and 650 nm. The curve has been taken at a bias of −2 V and

the monochromatic light has been obtained from the monochromator.

4.3.2 Temperature Sensitivity of OPDs

For the characterization of the temperature sensitivity, current-voltage curves have been taken at temperatures between 15 °C and 40 °C with intervals of 5 °C. The procedure has been repeated under the common illumination of 100 mA cm^{-2} and in darkness in Figure 4.21a. The current density has been plotted for the illuminated and for the dark case at −3.8 V bias with respect to the temperature in Figure 4.21b and 4.21c. It can be seen in Figure 4.21, that the current density increases with the temperature for the illuminated and the dark case. These results are in agreement with the theory that an increase of temperature leads to increased conductivity. The effect of the better conductivity has a huge impact for on the sample in darkness as the current density increases from 4 mA to 8.5 mA, an increase of more than 210 %. In the same temperature range the sample under illumination is less sensitive as the increase from 1.73 mA cm^{-2} to 1.76 mA cm^{-2} corresponds only to an increase of 1.7%. These investigations demonstrate that the impact, relative to the total current, of temperature on the OPD decreases under illumination.
In Figure 4.22 the normalized response, calculated according to Equation 3.4, under illumination of 100 mW cm^{-2} is presented. Figure 4.22a shows the response at a constant voltage of −3.8 V performing a current increase of roughly 1.7% for the temperature range from 15 °C to 40 °C. The opposite picture is drawn when a constant current is applied to the OPD, where we see a decrease of voltage for increasing temperature as shown in Figure 4.22b. The overall response in the temperature range from 15 °C to 40 °C shows a decrease of voltage by roughly 17%, 10 times bigger as compared to the voltage driven device. However it is worth mentioning that the supply by constant current is difficult and underlies considerable noise, due to the fact that the currents are very small. Additionally, if an array of photodetectors is required, e.g. for an image sensor, every pixel requires its own current supply. These requirements do not apply to a voltage driven system as a constant voltage can easily be applied to all pixels at the same time.

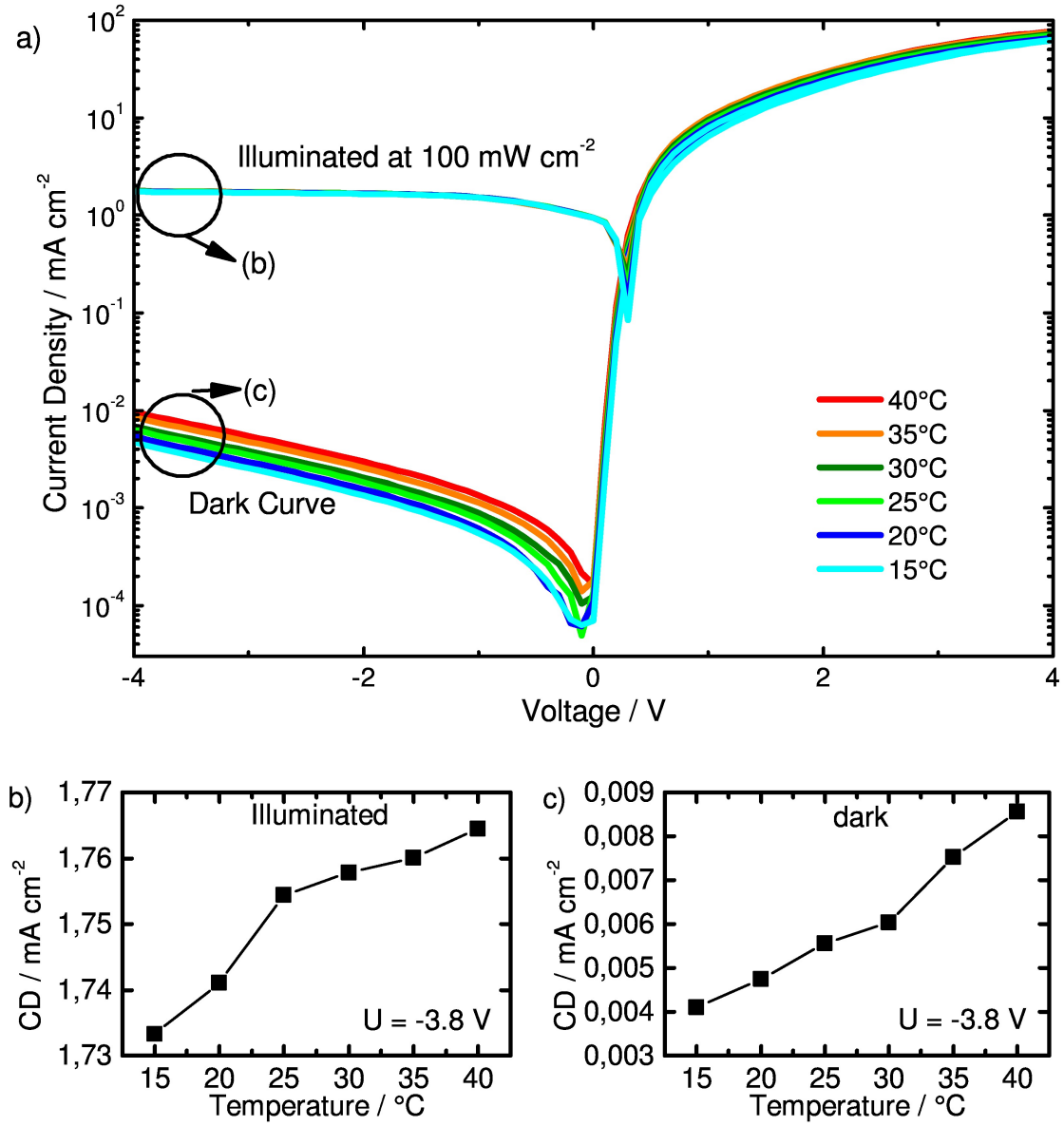

Figure 4.21: Electro-optic characteristics of the OPD at temperatures between 15 °C and 40 °C. (a) Current density under illumination at 100 mW cm^{-2} and in darkness between -4 and 4 V. (b) Current density at −3.8 V and under illumination (c) Current density at −3.8 V without illumination. In both cases the current density increases with the temperature due to the increased mobility of the charge carriers.

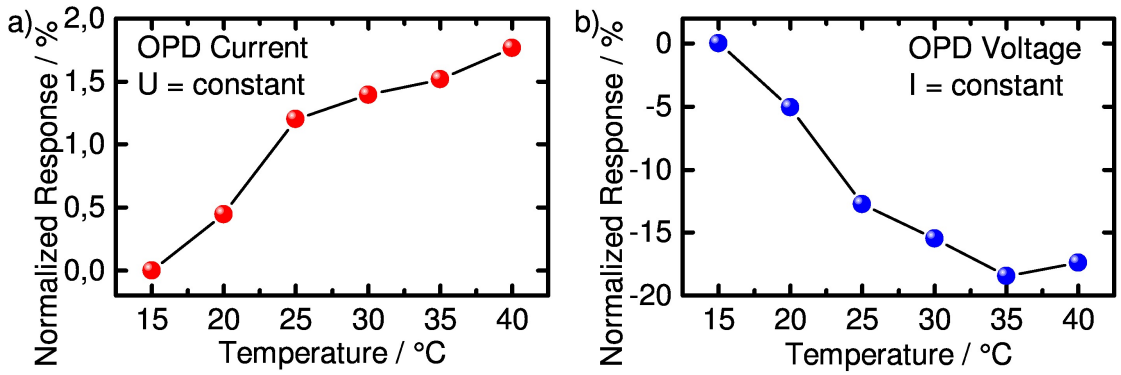

Figure 4.22: Normalized response of the OPD to the temperature under illumination of 100 mW cm^{-2}. For the cases (a) driven at constant voltage of −3.8 V and (b) biased at constant current of roughly 15.5 µA cm^{-2}.

5 Hybrid Organic/Inorganic Optical Sensors

In this chapter we demonstrate an innovative integrated sensing platform for PC based sensors. The detection of the photonic stop-band shift is demonstrated using an inorganic/organic hybrid approach. The detection of IR radiation is discussed in Section 5.1 and the detection of ethanol vapor is demonstrated in Section 5.2.

5.1 Infrared Detection Based on One Dimensional Photonic Crystal Sensors

In this chapter the previously discussed components – the OLED and the 1DPC – are assembled to the proposed thermo-optic sensing platform and the detection of IR radiation based on the thermally tunable 1DPC is demonstrated. In Section 2.4.1 the concept is demonstrated with several setups, to show the contribution of the single components. As the individual components may have a different thermal response, the design guide presented in Section 5.1.3 helps to design a system with a maximum response. The demonstration of the IR sensor, the calibration procedure, the detection of an IR pattern and a time domain analysis is conducted in Section 5.1.4. The results presented in this chapter are partially presented in our recently published article [Exn13].

5.1.1 Working Principle

The proposed sensor is an integrated device featuring a light source, a thermal tunable PC and a detector. The PC serves as sensitive component and translates the

present heat into an optical color. The light source and light detector translate the optical response into an electric current. The proposed concept is illustrated in Figure 5.1. The requirements for the light source are a homogenous light emission

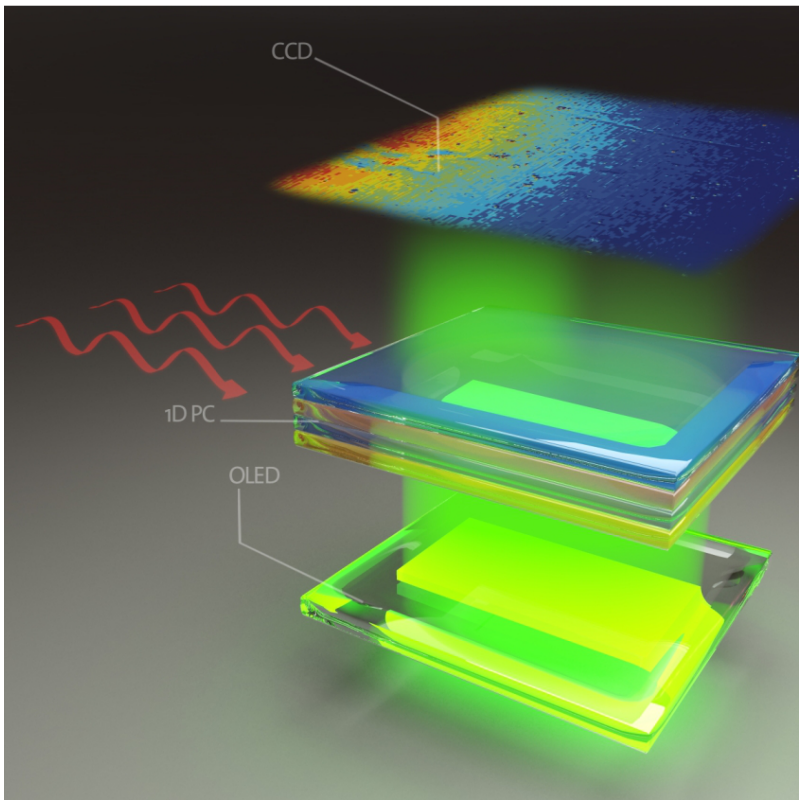

Figure 5.1: Illustration of the proposed IR sensor showing an OLED at the bottom, a PC in the middle and the image of a CCD camera at the top. The IR radiation from the left side heats the PC on one side, so that the transmission is increased. Reprinted adapted with permission from [Exn13]. ©2013 American Chemical Society.

over the whole sensor area, without heating the device and at the same time easy integrable with the rest of the sensor. Herein the OLED was chosen as a light source because of the good power efficiency, low profile and easy to assemble on the same substrate as the PC. The PC was chosen to be a stack of alternating layers of porous TiO_2 and porous SiO_2 exhibiting a high RI contrast and easy to assemble by subsequent spin-coating from solution [Pav12a, Pav12c]. For the detector a CCD camera was chosen in order to achieve a high image resolution. The assembly is shown in

Figure 5.2 on the left side, showing the OLED directly fabricated on the substrate as the PC and the CCD camera in some distance imaging the light output of the hybrid device. On the right side of Figure 5.2 the resulting thermogram, after a short heat-

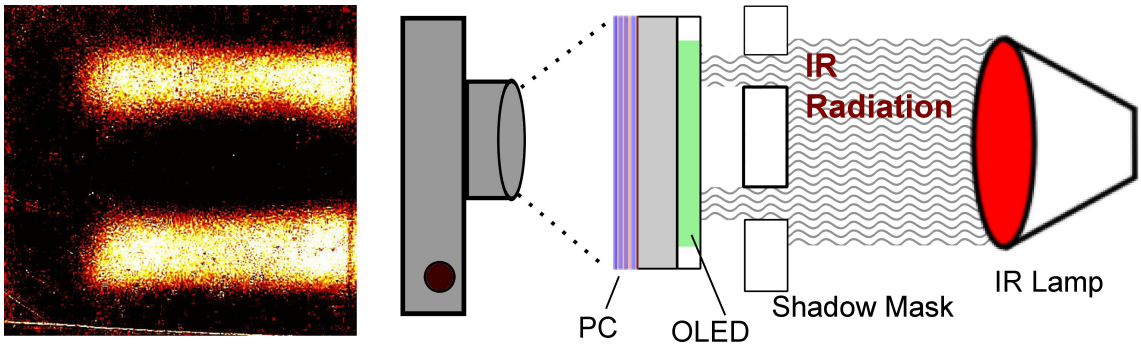

Figure 5.2: The experimental setup of the IR sensor, using an IR lamp and a shadow mask to create an IR pattern. The pattern is absorbed by the sensor and the corresponding image is recorded by the camera. On the left side a calibrated image taken with this setup is shown. The calibration has been done as described in Section 5.1.4.

ing on the left side, is shown. The picture can also be obtained by an array of OPDs fabricated directly on the PC, however in this thesis the image is captured by a CCD.

The intensity variations measured by the CCD can be explained by the change of OLED brightness and by the shift of the PC's stop-band. Figure 5.3 on page 84 demonstrates how the stop-band shift leads to an intensity tuning. The transmission of the wavelength range between 520 nm and 600 nm is increased upon heating. The increased transmission leads to a rise of light intensity, because the OLED spectrum (Figure 5.3b) lies in the same range. It shall be noted, that the transmission at the other side of the stop-band decreases and it is therefore a perquisite that the light source has a distinct color.

5.1.2 Temperature Tuned LED Light

As a first step, the concept is presented by a temperature sensitive PC and a separate steady light source. Therefore, an experiment has been set up where the light source is separated from the PC in order to prevent heating and, thereby, tuning of the

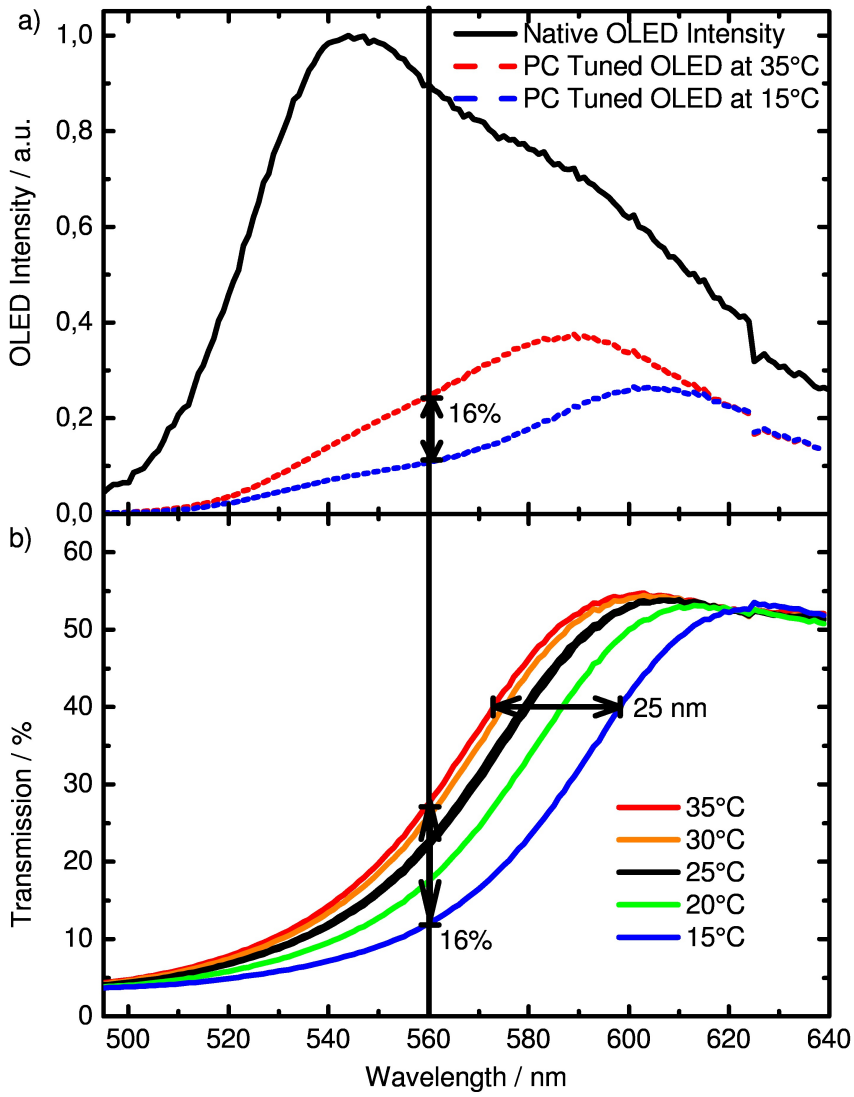

Figure 5.3: IR tuning principle (a) emission of the native OLED and the calculated spectrum of the OLED-1DPC hybrid. (b) the stop-band transmission of the PC for temperatures between 15 °C and 35 °C. The black line at 560 nm indicates the tuning principle: The stop-band shift of 25 nm induces a change of transmitted light of 16% at the exemplary selected wavelength of 560 nm. The OLED light transmission is changed accordingly by 16% less emission at the same wavelength.

light source as well. The LED light has been sent through a monochromator in order to allow a spectral analysis. The focused light beam was then send through a 1DPC of 6 bilayer TiO_2 and SiO_2, which was fabricated and temperature controlled as described in Chapter 3. The stop-band of the PC was chosen so that the LED peak lies on the red side of the photonic stop-band, which leads to an increase of transmitted light upon heating. Figure 5.4 shows the original LED light and the measured tuned light. The intensity tuning of the transmitted light at temperatures

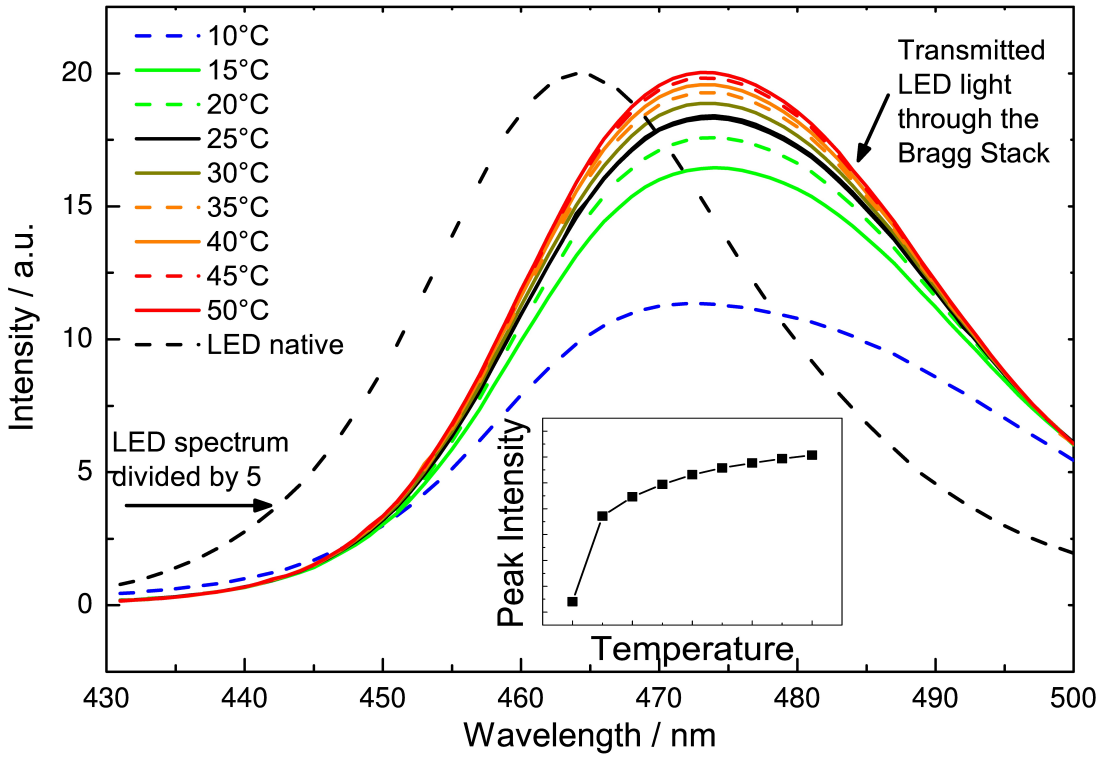

Figure 5.4: Demonstration of a temperature tuned light source. The LED light (black dotted line) is filtered through a temperature tuned 1DPC. The transmitted light intensity increases upon heating from 10 °C to 50 °C. The peak intensity of the tuned light is shown in the inset. The LED temperature, spectrum and light intensity remains constant.

between 10 °C and 50 °C is shown in Figure 5.4. It can be seen, that the transmission increases with the temperature because of the photonic stop-band shift to the blue which acts like a valve for light. As the shift is not linear for low temperatures,

we observe a stronger response for low temperatures as depicted in the inset of Figure 5.4. The light intensity at the peak wavelength is tuned by 200% in the temperature range from 10 °C to 50 °C.

5.1.3 Design Criterion

In this section the information about the temperature response of the individual sensor components is concluded so that a maximum response and sensitivity can be obtained. It is assumed, that the OLED, PC and OPD are thermally coupled, so that the incident IR radiation heats all three elements. If the thermal connection is not present (as it is for some experiments in this section) the respective response of the components that are not heated can be neglected. Figure 5.5 shows the response of the OLED, the PC and the OPD under different conditions so that either a positive response (signal increase with rising temperature) or negative response (signal decrease with rising temperature) is achieved. The response is given as the relative signal change (intensity for the OLED, transmission for the PC and current density for the OPD) with respect to the signal at 15 °C. For a good design, which aims at a maximum sensitivity it is important that the single responses all have the same sign in order to interfere constructively. This prerequisite leaves exactly two constructive scenarios: For the first scenario (i) all responses have a positive sign the setup from Figure 5.5a, 5.5c and 5.5e must be chosen, the OLED and OPD should be sourced with constant voltage, and the stop-band of the PC should be positioned so that the OLED emission lies at the red edge of the stop-band. The second scenario (ii), all responses have a negative sign, can be fabricated using a current sourced OLED and OPD, respectively, with the OLED emission spectrum at the blue edge of the PC. The second scenario produces an inverted response, an increase in temperature leads to a decrease of light intensity. The power supply with a constant current requires a structuring into pixels, of the OLED and the OPD and the supply of each single pixel with a constant current. Because of the very low current for the OPD and other technical aspects, like the number of required current sources, the technical realization becomes unnecessary complicated. For the named reasons the following IR sensors are build according to scenario (i) – constant voltage source and the OLED emitting at the red edge of the stop-band.

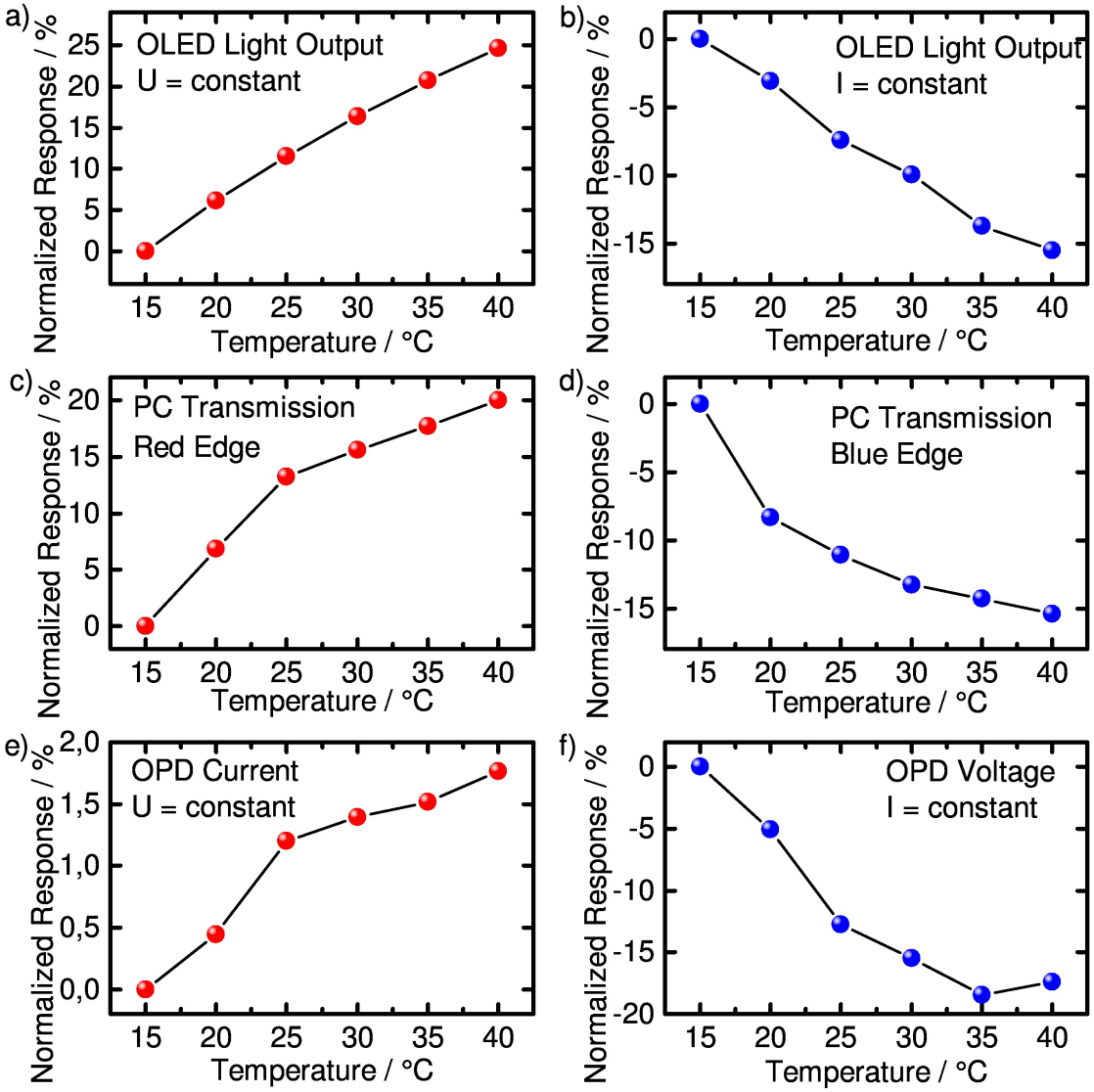

Figure 5.5: Guide for the design of 1DPC based IR sensors. The graphs conclude the response of every single component to temperature under two different boundary conditions. The vertical axis gives the NR, the relative change with respect to the initial response at 15 °C (see Section 3.3. (a) and (b) show the temperature response of an OLED biased at (a) constant voltage and (b) constant current. (c) and (d) show the transmission of the 1DPC at the red side and at the blue side of the stop-band, respectively. (e) and (f) show the photo induced current when biased with (e) constant voltage and (f) a constant current. For a good design the response of all components must have the same sign, either positive or negative. Note, for a constant current supply the OLED and the OPD must be structured into separated pixels and each pixel must be sourced individually.

In order to demonstrate the effect of the above mentioned design criterion and to build a first demonstration of the thermally tuned light source an OLED has been fabricated on the same substrate as a PC. The PC was situated at one side of the glass substrate and an OLED on the opposing site with the emission through the glass substrate. The fabrication procedure is described in Chapter 3. The stop-band of the PC was chosen to be on red edge of the OLED emission spectrum, so that a positive response, as depicted in Figure 5.5c is expected from the PC. The light output has been measured with a luminance meter for two different cases: (i) the OLED sourced with a constant current Figure 5.6a and (ii) the OLED sourced with a constant voltage Figure 5.6b. From scenario (i) (Figure 5.6a) the response of the

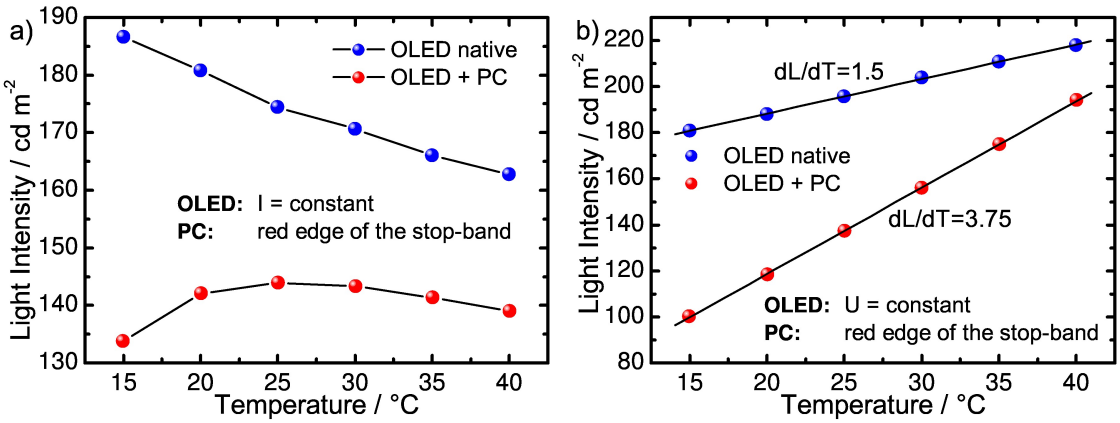

Figure 5.6: Response of the OLED-1DPC hybrid sensor with respect to the temperature. (a) a bad design since the OLED and PC response have opposing signs (Figure 5.5b and 5.5c). Both contributions cancel out the effect of thermal tuning in the single components. (b) a good design since the response of the OLED and PC have the same sign (Figure 5.5a and 5.5c). The response of the native OLED is enhanced from 1.5 cd m^{-2} K^{-1} to 3.75 cd m^{-2} K^{-1}.

OLED has a negative sign and the response of the PC has a positive sign which results in an overall response of 5 cd m^{-2} for the temperature range from 15 °C to 40 °C. The response is non-linear and features a positive slope in the range from 15 °C to 25 °C because of the dominating response from the PC. The range from 25 °C to 40 °C is dominated by the OLED response showing a decrease of luminescence. Figure 5.6b features an example for scenario (ii): both responses have the same

sign (positive) as shown in Figure 5.5a and 5.5c. The response of the native OLED is enhanced from $1.5\,\mathrm{cd\,m^{-2}\,K^{-1}}$ to $3.75\,\mathrm{cd\,m^{-2}\,K^{-1}}$ compared to the OLED-1DPC hybrid. This constellation delivers the best response, the parameters are concluded in Table 5.1 with a comparison to the native OLED. The resolvable temperature

	sensitive area [mm]	temperature response [cd m^{-2} K^{-1}]	resolvable temperature [mK]
OLED	3x3	1.5 ± 0.1	67 ± 3
OLED-PC	3x3	3.8 ± 0.1	27 ± 3

Table 5.1: Performance parameters of the native OLED compared to the OLED-PC hybrid. The resolvable temperature which is commonly noise limited, in this case is limited by the measurement resolution of the luminance meter (MavoSpot2) which was $0.1\,\mathrm{cd\,m^{-2}}$ and calculated according to Equation 5.1.

($T_{resolvable}$) is calculated from the resolution of the luminance meter (MavoSpot2) which was $V_{resolution} = 0.1\,\mathrm{cd\,m^{-2}}$ and the response of the device ΔS to a given temperature change ΔT according to Equation 5.1.

$$T_{resolvable} = \frac{\Delta T}{\Delta S / V_{resolution}} \tag{5.1}$$

The emission spectrum of native OLED and the OLED-PC hybrid with respect to to the temperature is demonstrated in Figure 5.7. The intensity is tuned by the temperature as the previously conducted experiments suggest. It can be seen that the OLED alone has a temperature response, which is investigated in detail in Section 4.1. In Figure 5.7b it can be seen, that the PC enhances the temperature response compared to the response of the native OLED. This experiment is indeed closely related to the tuned LED light of the preceding Section 5.1.2, however in this experiment also the light source simultaneously tunes the light intensity. It is shown that both effects can constructively interfere if a proper design is chosen. The previously mentioned design criterion only consider the intensity change, but the underlying process for the intensity change is the shift of the PC, which could be compensated by the shift of the OLED which was investigated in Section 4.1.2. For a constructive cooperation of both the shift of the OLED and the shift of the PC must be in the opposite direction. The TiO_2/SiO_2 PC that is investigated in this

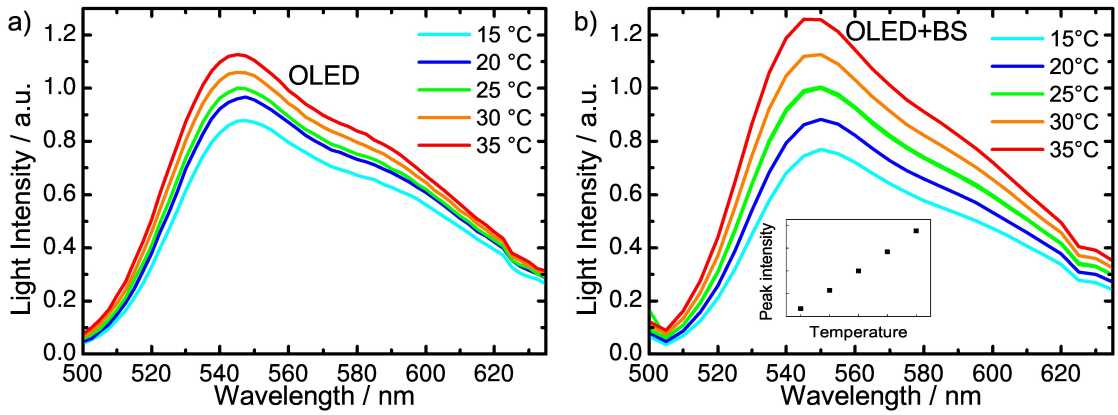

Figure 5.7: Spectral response of (a) the OLED at constant voltage and (b) the OLED-1DPC hybrid at constant voltage and at the red edge of the stop-band. The light intensity has been normalized to the peak intensity of the respective curve taken at 25 °C. It can be seen that the intensity change is more pronounced for the response of the hybrid device (b) compared to the native OLED (a). The peak intensity, depicted in the inset of (b) shows the same linearity as in Figure 5.6a.

thesis always shifts two the blue. The investigated OLED as well shifts to shorter wavelength. However, in the present setup, the shift of the OLED is with 2.5 nm one order of magnitude smaller compared to the shift of the PC which is 25 nm. In the presented setup, the shift of the PC is compensated by roughly 10% due to the fact that the shift of the OLED and the PC are in the same direction.

5.1.4 Demonstration of the Proposed IR Sensor

The single pixel of OLEDs and OLED-PC hybrid sensors have been extensively characterized and the conclusion was drawn, that an OLED-PC system exhibits the best response. In this section we want to demonstrate the feasibility of IR imaging with the proposed OLED-PC hybrid system using IR radiation and simple IR patterns to demonstrate the resolution of the sensor.

We used the previously as a single pixel investigated 3x3 mm OLED-PC system on a glass plate and mounted a CCD camera (µEye) above the device, so that images could be recorded. The OLED was sourced with a constant voltage of 4.5 V and the emission spectrum was situated on the red side of the stop-band, so that a

constructive interference of both tuning effects can be expected according to the design criterion of the previous section.

The camera image of the unexposed sensor is shown in Figure 5.8a and 5.8d, showing a rather homogeneous light distribution with some defects, that originate either from spin-coating defects of the PC or black spots from the OLED. Figure 5.8a shows the original black and white image from the CCD camera and Figure 5.8d shows a colored image for better visibility. The OLED-PC sensor was now exposed to IR light by a hot soldering iron (400 °C) from the side. The soldering iron was approached to the PC surface from the left side and exposed for 3 s, where the sensor was heated from one side and in turn increased the light output correspondingly as shown in Figure 5.8b and 5.8e. After 10 s of equilibration another picture was taken, where the heat is equally distributed over the whole sensor and correspondingly the intensity is homogeneous again, shown in Figure 5.8c and 5.8f. All pictures posses a general irregularity, resulting from intensity irregularities of the OLED and defects on the PC. The visible irregularities can be reduced by an image calibration technique described in the following section.

Image Calibration

The calibration procedure has two major goals: The improvement of image quality and the calibration for the actual temperature. Inhomogeneous dark and bright spots resulting from fabrication inhomogeneities can be removed by the simple subtraction of the background or offset intensity of each pixel. The background or offset intensity describes the light emission without heating. For a background subtraction a reference frame must be taken and subtracted from each subsequent frame. The resulting frame now shows only differences to the background frame and thus, the information about the heat distribution. The calibration for the actual temperature is done by knowing the heat response of the particular system, temperature change per intensity change (dT/dI) according to Equation 5.2.

$$\frac{dT}{dI} = \frac{T_2 - T_1}{\bar{I}_2 - \bar{I}_1} = \frac{33\,°\mathrm{C} - 27\,°\mathrm{C}}{178.8 - 168.4} = 0.58\,°\mathrm{C} \tag{5.2}$$

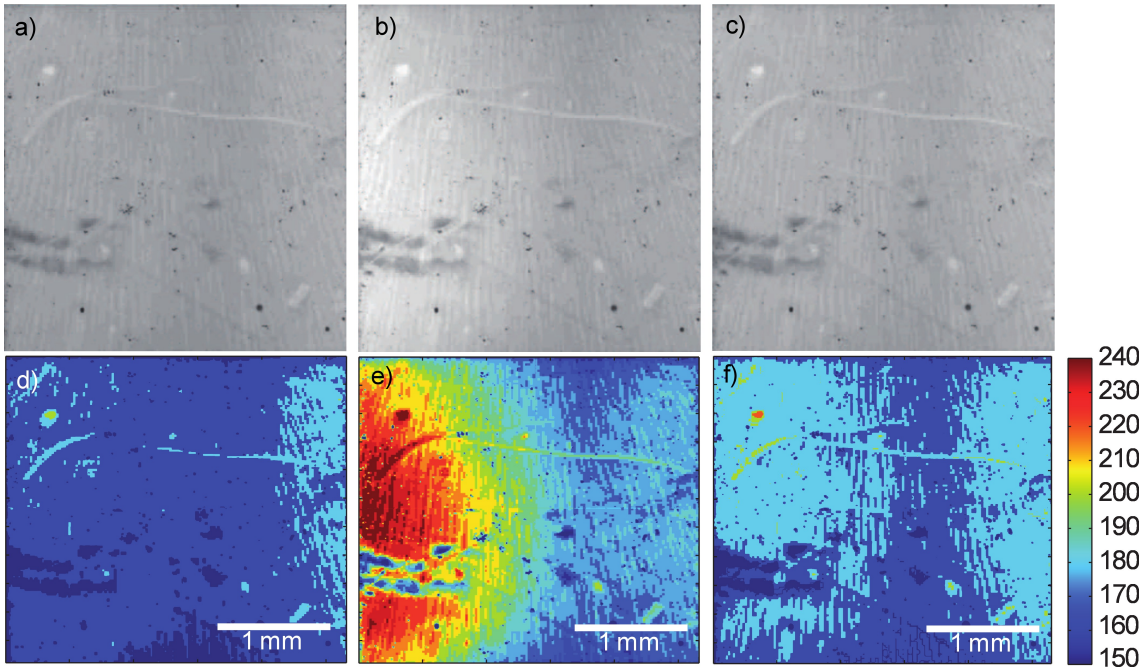

Figure 5.8: (upper row) Optical images demonstrating a thermal detector based on the OLED-1DPC approach. The OLED light is filtered by a thermally tunable 1DPC and the image is recorded by a CCD camera in (a) thermal equilibrium at 27 °C and (b) heated on the left side by a soldering iron. Figure (c) shows the sensor back in equilibrium at 33 °C. (lower row) the same images with temperature encoded pseudo color for better visibility as it is common in IR thermograms.

T_1 and T_2 are two different temperatures of the system, which have to be measured using a calibrated temperature sensor like the PT100. The average pixel intensities, represented $\bar{I}_1$ and $\bar{I}_2$ of the sensor in thermal equilibrium at the respective temperature (T_1 and T_2). To calculate the temperature of each pixel (T_{pixel}) the response from Equation 5.2 must be extrapolated and offset corrected according to Equation 5.3.

$$T_{pixel} = 27\,^{\circ}\mathrm{C} + (I_{pixel} - I_{27})\frac{dT}{dI} \tag{5.3}$$

With 27 °C as the offset temperature, the temperature of the reference frame and I_{pixel} the brightness value of the respective pixel. The linear extrapolation is done on the basis of the linear response of the single pixel sensor demonstrated in Figure 5.6b. The calibrated image is shown in Figure 5.9 showing a peak temperature of 60 °C at the left side of the sensor, the point closest to the soldering iron. And a steady decrease to room temperature to the right side.

IR Image Acquisition with a Shadow Mask

In this section the detection of three different IR pattern is demonstrated using an OLED-PC based IR sensor and a compact camera (DMC-LX5, Panasonic) to record the resulting image. The sensor size has been chosen to be 1.5 × 1.5 cm^2 in order to reduce the alignment effort and increase the image quality. Also the thickness of the glass substrate has been chosen to be 700 µm to achieve a faster response and better image quality. The IR source a 250 W heat bulb was placed in front of the IR shadow mask with a distance of 20 cm. For the patterning of the IR light three different shadow masks were created: (a) a single hole with the diameter of 5 mm, (b) two lines with a width of 4 mm and (c) an array of holes with a diameter of 1 mm. The shadow masks (a) and (b) were fabricated using 10 alternating layers of aluminum foil and paper 80 g m^{-2} which were perforated with a hole puncher and cut with scissors for the hole and line mask, respectively. The array of holes (c) was fabricated by drilling holes into a hard paper circuit-board (having a 2.54 mm grid and a thickness of 1.5 mm) and covering the board with one layer of aluminum foil on both sides. Holes were punched into the aluminum foil using a pen, from both sides. Photographic images of the masks are provided in Figure 5.10 in the upper line. The masks were placed directly on the sensor in order to produce a sharp IR

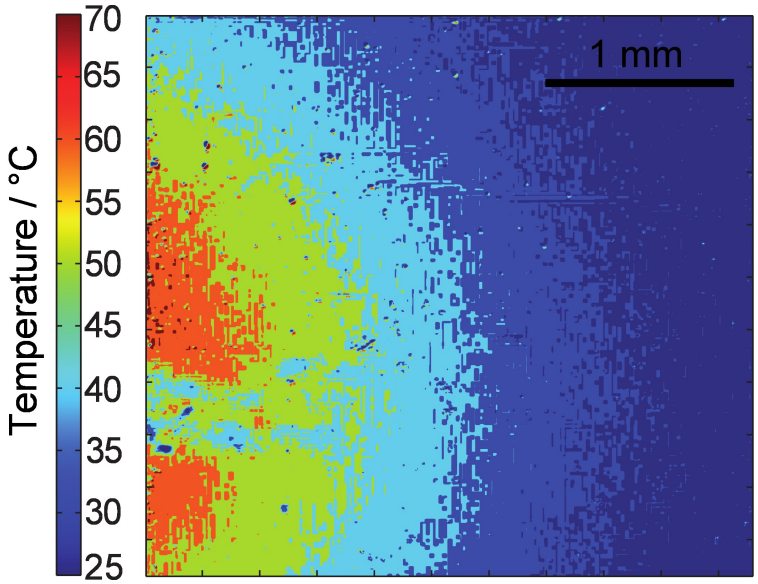

Figure 5.9: Calibrated thermogram obtained from the three images given in Figure 5.8. Image 5.8a and 5.8c have been used for the calibration, as the temperature and intensity for each pixel was known. The obtained data has been extrapolated linearly and the temperature has been calculated using the intensity values from Figure 5.8b. The image displayed in this Figure shows the heat distribution of the OLED-1DPC hybrid short after the heating on the left side. The maximum temperature reaches 60 °C on the left side and decades towards the right side until it reaches approximately room temperature. Reprinted adapted with permission from [Exn13]. ©2013 American Chemical Society.

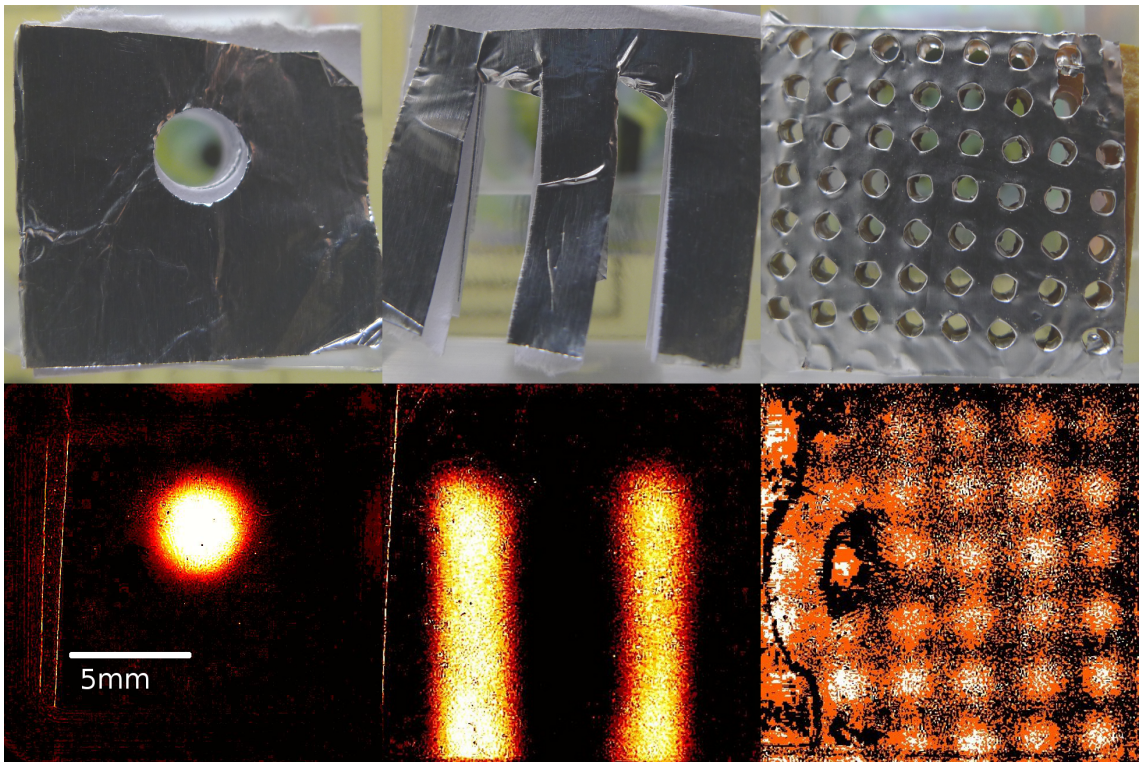

Figure 5.10: Sensor demonstration using an IR light source and a shadow mask to record simple images. (upper row) Three different shadow masks used to create different IR pattern on the sensor. The IR radiation is absorbed and the heat distribution becomes visible (lower row). The IR images are subtracted by a reference frame, so that only heated parts are visible and the rest remains black.

pattern. The sample was assembled with the metal layer of the OLED facing to the IR source and the emission away from the IR source, through the PC and towards the camera. The camera was set in macro mode, which enables sharp pictures down to a focus distance of 1 cm and was placed with an approximately 1.5 cm spacing in front of the sensor. A video was taken at a frame rate of 30 frames per second and a resolution of 720 × 1280 pixels. The obtained video was processed for background subtraction, noise canceling and contrast adaption using the MATLAB script shown in Apendix A.3. For the background subtraction, a reference frame consisting of the average of the first 10 frames was subtracted from the subsequent frames. For noise reduction 10 video frames were averaged and the contrast was adjusted in order to fill the dynamic range of an 8-bit monochrome image which was assigned to a new color-map (*hot* by MATLAB) in order to enhance the visibility and achieve the typical look of IR images. The obtained images after 1.33 s of exposure to the IR light are presented in Figure 5.10 in the lower line. The images show a clear copy of the mask with a gradient at the edges of the mask, due to the heat conduction of the substrate and transmission through the black parts of the mask. The blur is especially visible for the array of dots shown in the right image. With increasing exposure time the and the lack of a sensor cooler, the whole substrate starts to warm up, as can be seen in the time resolved image series from 0 s to 14 s after exposure in Figure 5.11. It can be seen from the figure that, in the first two frames, mostly noise is visible. The visibility of the pattern increases in the subsequent frames. Roughly one second after exposure the two lines are clearly visible, and become continuously stronger. After 5 s of exposure, the response starts to blur out due to the lateral heat conduction of the sensor and possibly also due to heat transmission of the shadow mask.

5.2 Optical Sensing Platform for Chemicals

In this section we demonstrate a chemical sensing platform based on a 1DPC which is responsive to various chemicals. The sensing platform translates a photonic stop-band shift of a PC into electrical currents. The theoretical design and experimental results are accompanied by simulations and a comprehensive investigation of the signal transduction. Using our sensing concept, we demonstrate the detection of

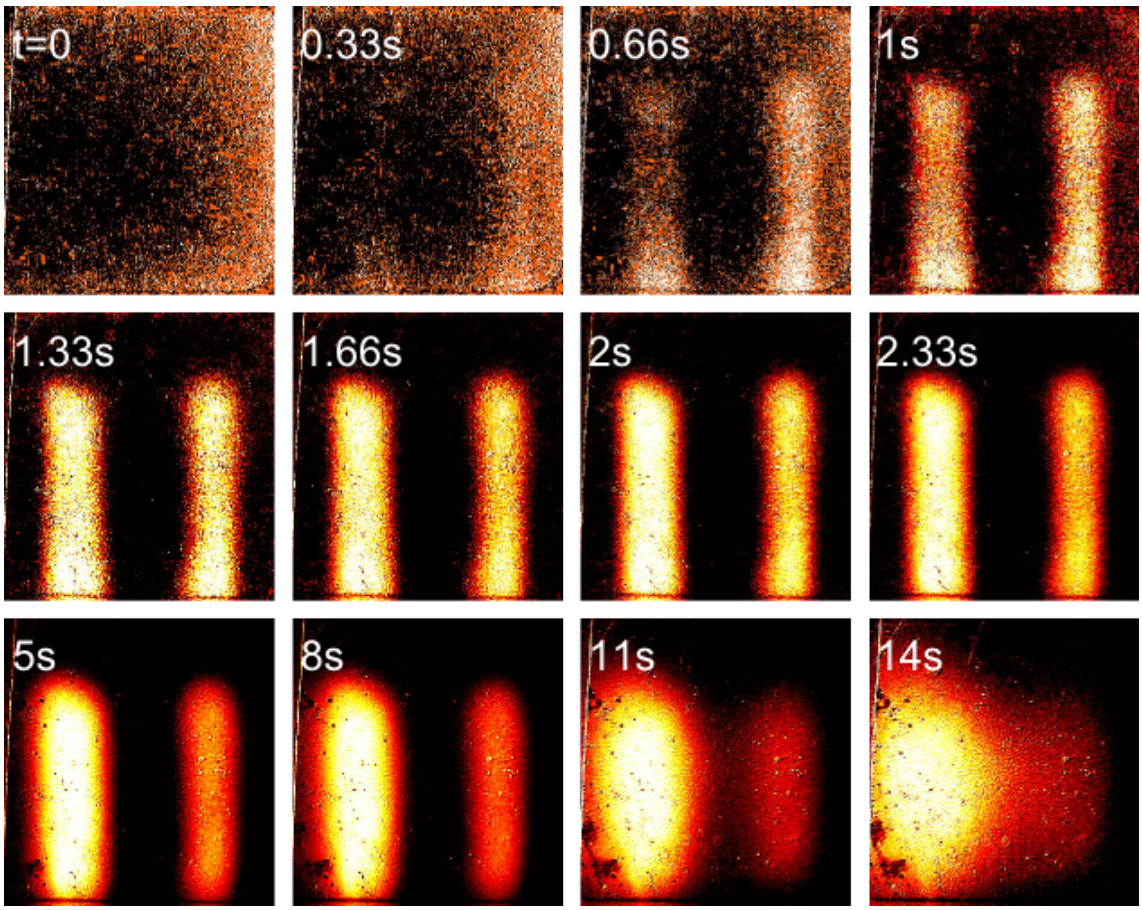

Figure 5.11: IR image of a the shadow mask shown in Figure 5.10 producing a pattern of two lines on the sensor. The series shows the time resolved response with t equal to the time after IR exposure. The lines are fully visible after one second, after that the sensor heats up, until the pattern starts to blur out because of the heat conduction through the sensor and possibly also through the mask after five seconds of exposure.

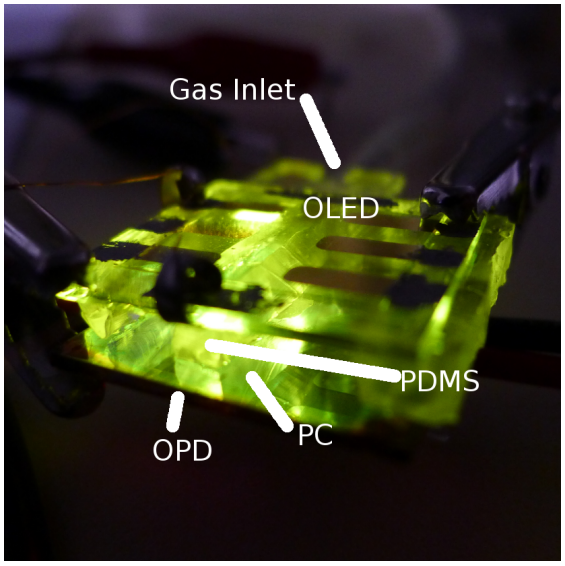

Figure 5.12: Photographic image of the sensor setup, with a PDMS chamber featuring inlet for the analyte gas coming from the gas flow setup.

ethanol concentrations down to approximately 10 ppm in nitrogen, which corresponds to a stop-band shift of 27 pm. The resolution of the proposed platform exceeds the capabilities of the most commercial spectrometers and by far the human eye, while at the same time such sensor is less expensive and less power consuming than a spectrometer.

5.2.1 Design of the PC-Based Sensor

The sensing platform features an organic light-emitting diode (OLED) as a narrowband light source, a sensitive 1DPC as a detector and an OPD as a light sensor. Figure 5.12 shows a photographic image of the setup, which features an integrated polydimethylsiloxane (PDMS) test camber. In the picture the OPD is fabricated on the same substrate as the PC. However, in later experiments we separated both devices on different substrates as it gives more flexibility for the experiments and the PC can be easily exchanged. The porous PC fabricated from SiO_2 and TiO_2 NP suspension exhibits an optical response when exposed to chemicals. Namely the photonic stop-band shifts, which can be measured using an OLED and an OPD.

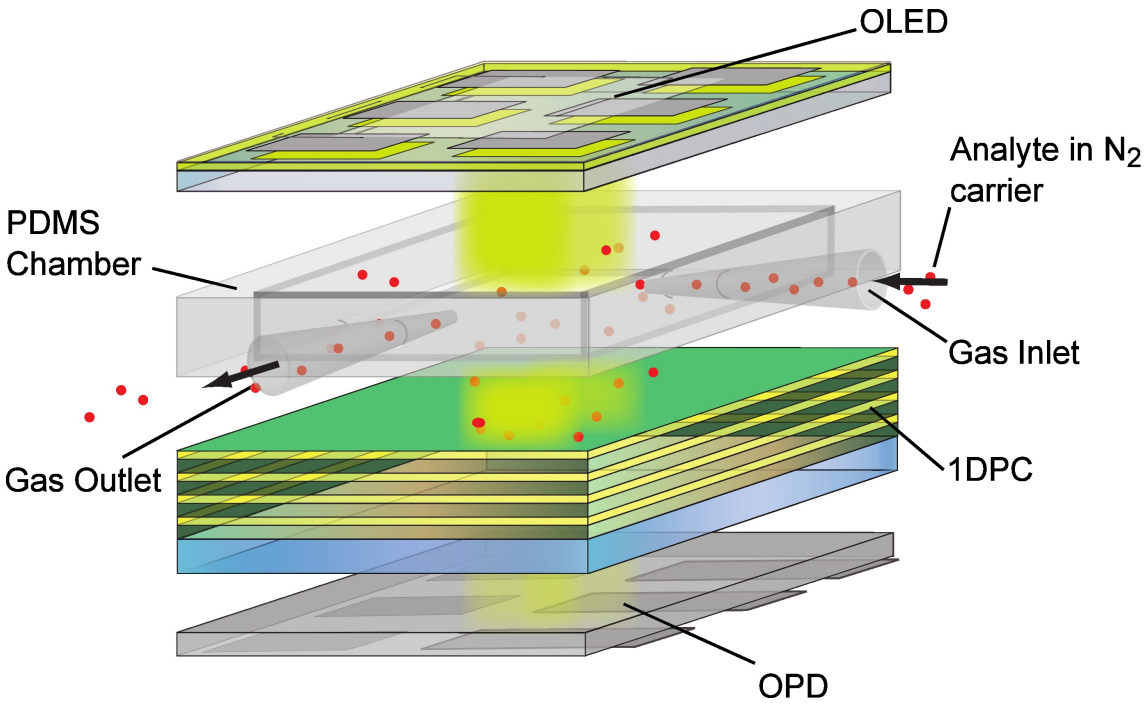

Figure 5.13: Scheme of the PC-based chemical sensor showing the assembly of the components in order to measure the photonic stop-band tuning. The assembly shows the OLED, which emits light in a specific wavelength range and shines trough the PC. The PC tunes the OLED light transmission intensity according to the test gas concentration in the PDMS chamber. For an easy exchange of the test gas the PDMS chamber features an in- and output hole, where one side was connected to the output of the mass flow setup. The tuned light intensity is measured by the OPD located at the bottom of the assembly. Image courtesy of Ida Pavlichenko.

The scheme of the proposed sensing platform in shown in Figure 5.13. The OLED light is filtered through the PC and the transmitted light is recorded by the OPD. With a good design the transmitted light and, thus, the OPD current changes with the analyte concentration.

The OLED has been chosen due to its suitable emission wavelength, small extensions and the generally low power consumption. The emission spectrum can be, if required further tuned using i.e. NP suspensions [MF13]. For this sensor the OLED polymer PDY-132 has been chosen with a peak emission wavelength at 545 nm.

The PC consists of 6 bilayers of porous TiO_2 and SiO_2 which feature, due to their high RI contrast, a pronounced photonic stop-band. The layer thickness of the TiO_2 (70 nm) and SiO_2 (130 nm) was chosen, so that the blue edge of the stop-band lies at 545 nm, where the OLED emission peak is located. For the design of a PC-based sensor two major criteria are important: the position and the shape of the photonic stop-band. The position of the stop-band should be chosen so that the steepest slope lies in the peak-wavelength of the emission spectrum of the light source. The shape should be designed so that the slope is constant over the whole wavelength range of the emitted light. Besides these criteria it is still a mayor challenge to fabricate a PC that exhibits big shifts of the stop-band position which in turn gives rise to a high sensitivity. For the proposed device, we selected the combination of porous TiO_2 and porous SiO_2 to fabricate the PC, via spin-coating of a NP suspension, because of their high RI contrast and their suitable morphology for sensing. Due to the large surface area and voids in the porous PC, the assembly features an inherent broad sensitivity to all materials with a RI greater than one and at the same time is easy to fabricate.

The optical detection has been done using an OPD fabricated from a P3HT/PCBM solution. The OPD was chosen because of the sensitive wavelength range in the visible spectrum from 300 nm to roughly 800 nm and the possibly low cost and large area fabrication. A detailed explanation of the fabrication for the above named components is given in Section 3.1.

5.2.2 The Signal Transduction Scheme

For the demonstration of the signal transduction scheme, we measured the reflection spectrum of the PC upon exposure to various ethanol concentrations with a spectrometer. The shift was extracted from the measurements and plotted in Figure 5.14a. A continuous shift can be seen, which is stronger for lower concentrations and decreases to almost zero for concentrations $p/p* \geq 80\%$ (The calculation of p/p* is described in Section 3.2.7). From this basic characterization of the stop-band shift we go to a simplified readout using the proposed setup with an OLED-1DPC-OPD

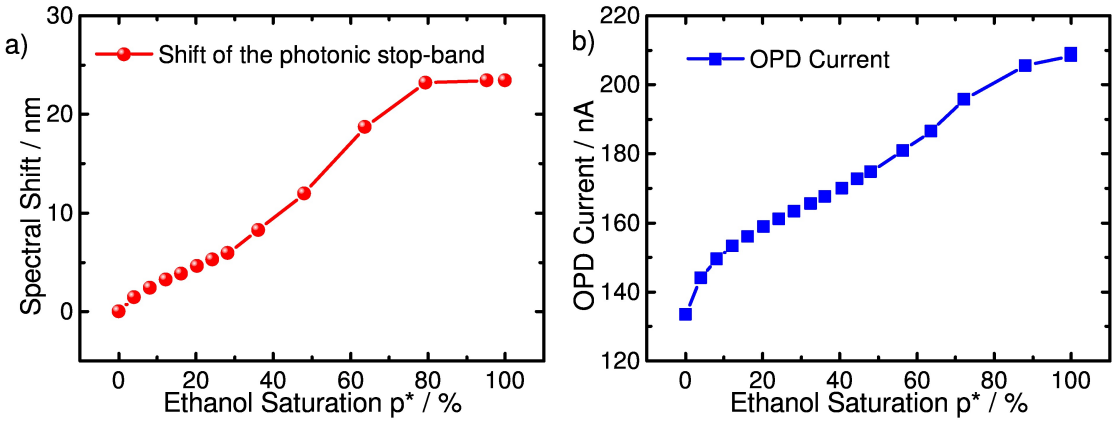

Figure 5.14: Graphs illustrating the coherence of the stop-band shift and the OPD current in the proposed sensing scheme for ethanol concentration in nitrogen from 0% to 100%. (a) The shift of the stop-band. (b) The measured OPD current. The two graphs illustrate the signal transduction, from the optical shift to an electrical signal via the proposed electro-photonic sensing platform.

so that the output signal – an electric current – indicates the ethanol concentration (Figure 5.14b). The OLED-PC-OPD setup has been exposed to roughly the same ethanol concentrations as the PC alone, before. The stop-band shift of 24.4 nm causes the OLED light to be tuned, so that the different light intensities can be recorded at the OPD. Figure 5.14b shows the OPD current for the concentration range from 0% to 100% as it changes from 133 nA to 210 nA. The distinct similarity of the stop-band shift and the OPD current is originated from the linear relation of light intensity and photo-current. The resulting output signal, a DC current, acquired from the intensity measurement of the OPD, represents the stop-band position. As previously mentioned, one is often interested in detecting traces of a gas. The minimum shift that can be detected with this setup can be calculated by knowing the shift of the stop-band and the measurement precision of the OPD current. For low concentrations (p/p* 0% to 4%) the OPD current changes with 7.4 nA nm^{-1}. We know from statistical noise analysis that the root-mean-square (RMS) noise of the OPD current lies in the order of 0.2 nA. These values give a signal-noise-ratio (SNR) of 1 for a shift of only 27pm. Of course better values can be obtained using a more precise setup.

5.2.3 Response Analysis

This very high precision, which indeed exceeds the performance of most spectrometers by one order of magnitude must be demonstrated in a practical detection of an analyte. Therefore, we took a response curve for ethanol concentrations in nitrogen from 10 ppm to 260 ppm and an exposure time of 60 s for each interval. After the exposure interval the chamber has been flushed with nitrogen for another 60 s to show the reversibility of the ethanol response. The response of the OPD current to ethanol originates solely from the adsorption of ethanol molecules in the PC and the resulting stop-band shift, as experiments with the same setup but without PC have shown no response. The response-curve plotted in Figure 5.15a shows a steady increase of the OPD current with rising ethanol concentrations. The nitrogen flush cycles after exposure to ethanol clearly show the fast desorption of the ethanol molecules from the PCs pores. For this response-curve the normalized response (NR) has been calculated according to Equation 3.4 and plotted in Figure 5.15b. It can be observed that the response increases fairly linear to more than 0.9% for a concentration of 260 ppm ethanol molecules in nitrogen, which implies that the measured current under exposure to the ethanol was 0.9% higher than the initial 193.8 nA. A very important parameter besides the NR is the response time of the sensor. Most sensors, including the one proposed, are dependent on diffusion processes. The theoretical response time can be very long, it is therefore feasible to only measure the time for 90% of the response. The response time has been determined as illustrated in Figure 5.15c, which gives a response time $t_{10-90} = 2.6s$ for the ethanol concentration of 100 ppm.

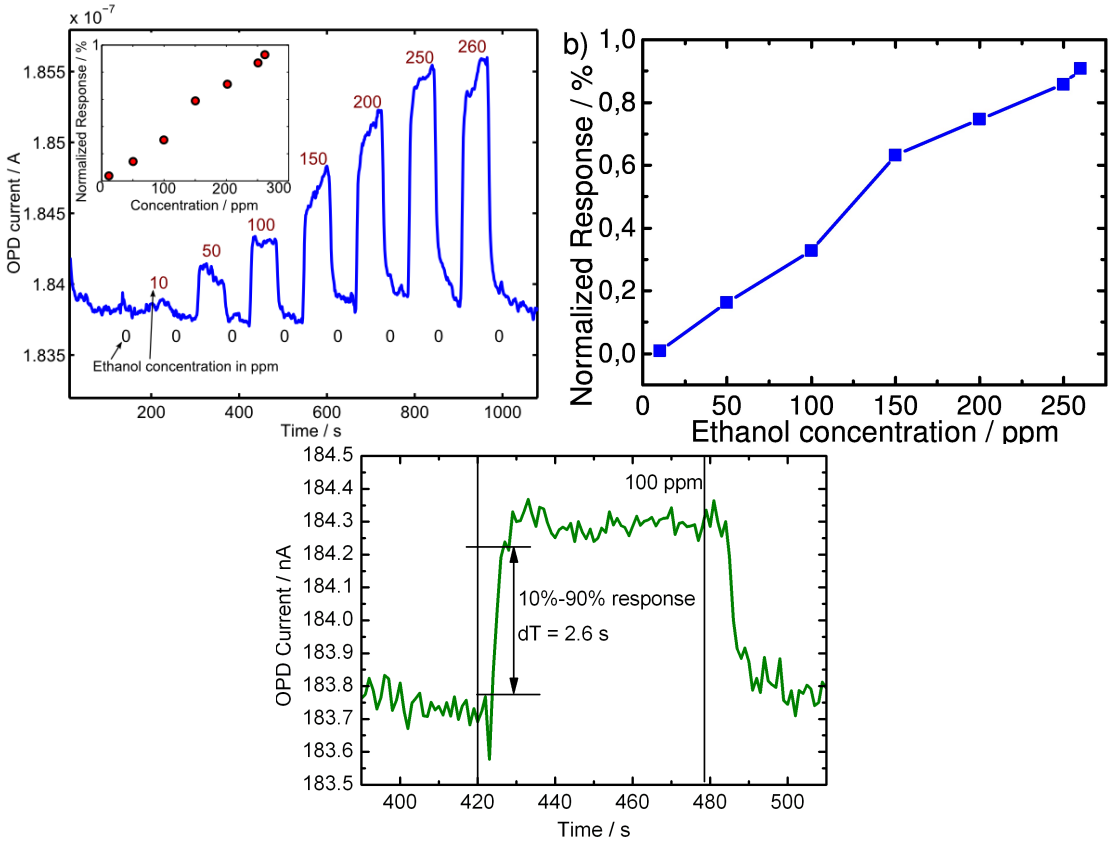

Figure 5.15: Response of the sensing platform under exposure to ethanol concentrations in nitrogen between 0 ppm and 260 ppm. (a) Response over time, with alternating exposure and flushing cycles with a cycle length of 60 s. (b) Calculated NR for each response from (a). (c) Response time analysis at the exposure to 100 ppm ethanol in nitrogen, showing a response time from 10 % to 90 % of the final value of $T_{10-90} = 2.6s$.

6 Conclusion & Outlook

The goal of this thesis, to demonstrate IR imaging with a PC based sensor has been achieved and a detailed analysis of the response and design of such a system has been outlined in Section 5.1 – Infrared Detection Based on One Dimensional Photonic Crystal Sensors. The single device component have been characterized in terms of response to temperature, water vapor and ethanol vapor. We have found that temperature effects all of the components, (i) the OLED, (ii) the PC and (iii) the OPD. (i) The OLED exhibits a temperature dependent light intensity, emission spectrum, electrical conductance and power conversion efficiency. The OLED is not affected by water vapor or nitrogen vapor. (ii) The PC has besides the temperature sensitivity, also a sensitivity to humidity and ethanol. The influence of ambient humidity and the response to ethanol vapor has been investigated. (iii) The OPD temperature characteristics have been investigated along with the spectral sensitivity. Water vapor and ethanol vapor do not affect the OPD response. The results of the sole component investigation have been used to formulate design criterion for the development of a PC based IR sensor. The design guidelines are presented in Section 5.1.3 – Design Criterion.

It has been found, that the control over the morphology of the PC can be used to sensitize the PC for the detection of molecules. The infiltration of molecules into the porous structure of the PC exhibits a colorimetric change. The colorimetric change of the PC is a measure of the analyte concentration it is exposed to. A sensing platform for the simple translation of the colorimetric change into a DC current has been developed and is presented in Section 5.2 – Optical Sensing Platform for Chemicals.

6.1 Major Results

Detailed Analysis of the Effect of Ambient Humidity on 1D Photonic Crystals A detailed investigation of the PCs used in this thesis has been done in Section 4.2. The influence of ambient condition have been explicitly investigated and the results were also presented in a journal publication in 2012 [Pav12a].

The Effect of Different Morphologies on the Photonic Crystals The effect of various morphologies, has been investigated in combination with the influence of ambient conditions. It has been demonstrated that the sensitivity can be tuned by changing the textural porosity. The results can also found in a journal publication from 2012 [Pav12b].

Infrared Detection with Photonic Crystals The influence of temperature on the photonic crystal has been investigated by heating and cooling the sensor via a Peltier element in order to evaluate the tunability of the PC. IR pictures have been taken by heating with a soldering iron or, via an IR beam which was patterned by a shadow-mask. The demonstration of the sensor is published in the journal "Advanced Materials and Interfaces" in 2013 [Exn13].

Development of a Sensing Platform for the Detection of Vaporized Solvents A sensing platform for a simple detection approach of the PC stop-band shift has been designed and demonstrated, based on an OLED and an OPD. The results were presented in Chapter 5.2, showing a detection precision for the stop-band shift of 27 pm at a SNR of 1.

Simulation of the Device The experimental results have been accompanied with simulations made in COMSOL Multiphysics. The influence of the thickness and RI of the PC materials has been investigated and the full infiltration of the PC by ethanol molecules has been proved. Some of the simulated results are published in 2012 [Pav12c].

6.2 Outlook

The main goal and focus of this thesis was the demonstration of PCs as IR and chemical sensors. The next logical step is to analyze the capabilities of the proposed sensors and optimize towards a potential application. The key element of the sensor is the PC, therefore an optimization, towards sensitivity and selectivity would yield significantly better performance of the system. Another important field is the OLED stability, as currently the OLED remains stable for an operational lifetime of approximately 100 h and a longer lifetime would be desirable. The challenge around the OLED lifetime is relatively minimal given there are already OLEDs with more than 10×10^5 h on the market today.

The next step for building an integrated detector would be the integration of an OPD or a CCD sensor directly on the PC. In case of the OPD the fabrication of an active sensor array can be very difficult, however if one uses a CCD sensor chip, and focuses only on the integration of the devices, the required effort is significantly reduced.

A Appendix

A.1 List of Lab Instruments

Instrument	Description
CCD Camera	µEye camera UI-2240-M, IDS. The camera features a monochrome CCD sensor resolving 1280 × 1024 pixels. An Optem Zoom 70XL macro objective has been used giving a field of view of 6.4 × 8.53 mm^2 at the minimum magnification.
Compact Camera	DMC-LX5, Panasonic. The maximum video resolution is 1280 × 720 pixels at 30 frames per second.
Cryostat	Optistat™, Oxford. Using and ILMVAC LaboVac turbo molecular pump.
Glovebox	MB20G LMF, MBraun. Nitrogen glovebox with O_2 and H_2O content smaller than 10 ppm, typically 0.1 ppm.
Luminance Meter	Mavo Spot2.
Monochromator	Cornerstone™ 260 1/4 m, USB - Newport 74125 ser.no. 258; Merlin™ UV silicon Detector (calibrated), 10 × 10 mm^2, 200-1100 nm, Newport ord.no. 70356; Merlin™ digital lock-in radiometry system, Newport 70105 ser.no.184; Arc lamp high pressure Hg 300W.
Plasma asher	Femto, Diener electronics.
PVD system	Univex 350G, Oerlicon Leybold.
Sourcemeter	Sourcemeter 2600 and 2636, Keithley.

A.2 Abbreviations

1DPC	1-dimensional photonic crystal
BS	Bragg stack
CCD	charge-coupled device
CMOS	complementary metal oxide semiconductor
CVD	chemical vapor deposition
DBR	distributed Bragg reflector
EG	ethylene glycol
EL	electroluminescence
FWHM	full width at half maximum
HTL	hole transport layer
IR	infrared
ITO	indium-tin-oxide
LMU	Ludwigs-Maximilians-Universität
NP	nanoparticle
OLED	organic light emitting diode
OPD	organic photodetector
PC	photonic crystal
PDMS	polydimethylsiloxane
PEDOT	poly(3,4-ethylenedioxythiophene)
ppm	parts per million
PVD	physical vapor deposition
PSS	poly(styrene sulfonate)
PT100	platinum resistive thermometer with 100 Ω electric resistance
RI	refractive index
SEM	scanning electron microscope
SNR	signal-noise-ratio
TEC	thermal expansion coefficient
TOC	thermo-optic coefficient
TOE	thermo-optic effect

A.3 MATLAB Code

A.3.1 Video Preparation

The Program reads the first frames of a video file from offset to *offset+boxcar* and averages them for use as a reference frame. The subsequent frames are treated as movie frames which are subtracted by the reference frame so that differences to the reference remain. Also here the number given in *boxcar* determines the number of frames to be averaged. The resulting difference frame is brightness adjusted so that it fills the color-space of an 8 bit image. The frames are stored in .avi format. Observe that both, the input and output codec must be installed on the executing computer.

```
clear all;
 filelist =dir('*.MOV'); %create a file list for all *.MOV files in the folder

for k=1:length( filelist )
    clear mov;
     file =VideoReader( filelist (k).name);%read the next movie

    length=500; %manual length selection if "numberoffframes" does not work
    length=file.numberoffframes %determine the length of the video

    %frame select size in pixel
     xstart =300;
    xstop=800;
     ystart =170;
    ystop=600;

     offset =10; %frames with an index from offset to offset+boxcar are reference frames
    boxcar=10; %number of frames to average
    cmap = hot(256);% colormap, alternative: cmap = gray(256);

    for i=1:boxcar %read the reference frames
        ref (:,:,:, i)=read( file , i+offset );
    end

    refavg=(mean(ref,4)); %averaging the reference frame for noise reduction
```

```
    frameavg=0;                                                                    26
                                                                                   27
    for i=1:floor((length-offset)/boxcar)-1 %loop for the movie frames             28
        clear pic;                                                                 29
                                                                                   30
        for j=(i*boxcar+1):(i*boxcar+boxcar) %reading the movie frames to average  31
            pictemp=read(file,j+offset);                                           32
            pic (:,:,:, j-boxcar*i)=pictemp;                                       33
        end                                                                        34
                                                                                   35
        picavg=(mean(pic,4)); %averaging the movie frame for noise reduction       36
        frm=imadjust(rgb2gray(uint8(picavg-refavg))); %adjust the brightness       37
        frm=flipdim(frm,2); %optional mirroring (vertical)                         38
        mov(i)=im2frame(frm,cmap); %assembling the movie frames                    39
    end                                                                            40
                                                                                   41
    fname=regexprep(file.name,'.MOV','-diff.avi') %creating the new file name      42
    movie2avi(mov,fname,'compression','MSVC','colormap',hot(256),'fps',3); %write file 43
end                                                                                44
clear                                                                              45
```

A.3.2 MATLAB Function for COMSOL Calculations

The following code section shows the MATLAB function that was called to simulate the transmission of a PC with 9 bilayers as drawn in Figure 3.3. The function calls a COMSOL instance and passes the setup and simulation parameters. COMSOL and MATLAB must be started in the *COMSOL with MATLAB* mode. The function returns a 601x2 matrix with the wavelength parameter in the range from 300 nm to 900 nm in the first column and the transmission in the second column. The transmission is given in decibel (dB), the transmission in % can be calculated according to Equation A.1.

$$Transmission[\%] = 10^{\frac{Transmission[dB]}{10}} \tag{A.1}$$

In the present work, the function below was run from a MATLAB script, which sequenced numerous simulations, calculated the transmission in % and stored the results.

```
function [transmission] = bs9dl(si_thickness, ri_si, ti_thickness, ri_ti)

start=300e-9;
step=1e-9;
stop=900e-9;

% COMSOL Multiphysics Model M-file
% Generated by COMSOL 3.2 (COMSOL 3.2.0.222, $Date: 2005/09/01 18:02:30 $)

flclear fem

% COMSOL version
clear vrsn
vrsn.name = 'COMSOL 3.2';
vrsn.ext = '';
vrsn.major = 0;
vrsn.build = 222;
vrsn.rcs = '$Name: $';
vrsn.date = '$Date: 2005/09/01 18:02:30 $';
fem.version = vrsn;

% Constants
fem.const = {'tio2', ti_thickness, ...
  'sio2', si_thickness};

% Geometry
g1=rect2('tio2','1e-7','base','corner','pos',{'0','0'},'rot','0','const',fem.const);
g2=rect2('sio2','1e-7','base','corner','pos',{'tio2','0'},'rot','0','const',fem.const);
garr=geomarrayr(g1,si_thickness+ti_thickness,0,9,1);      %15e-8
[g3,g4,g5,g6,g7,g8,g9,g10,g11]=deal(garr{:});
garr=geomarrayr(g2,si_thickness+ti_thickness,0,9,1);      %15e-8
[g12,g13,g14,g15,g16,g17,g18,g19,g20]=deal(garr{:});

% Descriptions
clear descr
descr.const= {'sio2','Thickness SiO2','tio2','Thickness TiO2'};
fem.descr = descr;
```

```
% COMSOL Multiphysics Model M-file
% Generated by COMSOL 3.2 (COMSOL 3.2.0.222, $Date: 2005/09/01 18:02:30 $)

% Geometry
clear s
s.objs={g1,g2,g4,g5,g6,g7,g8,g9,g10,g11,g13,g14,g15,g16,g17,g18,g19, ...
  g20};
s.name={'R1','R2','R3','R4','R5','R6','R7','R8','R9','R10','R11', ...
  'R12','R13','R14','R15','R16','R17','R18'};
s.tags={'g1','g2','g4','g5','g6','g7','g8','g9','g10','g11','g13', ...
  'g14','g15','g16','g17','g18','g19','g20'};

fem.draw=struct('s',s);
fem.geom=geomcsg(fem);

% Initialize mesh
fem.mesh=meshinit(fem);

% Refine mesh
fem.mesh=meshrefine(fem, ...
                    'mcase',0, ...
                    'rmethod','regular');

% (Default values are not included)

% Application mode 1
clear appl
appl.mode.class = 'InPlaneWaves';
appl.module = 'EM';
appl. assignsuffix  = '_emwe';
clear prop
prop.inputvar='lambda';
appl.prop = prop;
clear bnd
bnd.inport = {0,0,1,0};
bnd.E0 = {{0;0;0},{0;0;0},{0;0;1},{0;0;1}};
bnd.name = {'outer','inner','','',''};
bnd.portnr = {1,1,1,2};
bnd.type = {'M','cont','port','port'};
```

```
bnd.ind =       [3,1,1,2,1,1,2,1,1,2,1,1,2,1,1,2,1,1,2,1,1,2,1,1,2,1,1,2,1,1,       ...
        2,1,1,2,1,1,2,1,1,2,1,1,2,1,1,2,1,1,2,1,1,2,1,1,4];
appl.bnd = bnd;
clear equ
equ.name = {'ti','si'};
equ.matparams = 'n';
equ.n = {ri_ti, ri_si};     %2,1.3
equ.ind =     [1,2,1,2,1,2,1,2,1,2,1,2,1,2,1,2,1,2];
appl.equ = equ;
appl.var = {'nu','1e9'};
fem.appl{1} = appl;
fem.border = 1;
fem.units = 'SI';

% Descriptions
clear descr
descr.const= {'sio2','Thickness_SiO2','tio2','Thickness_TiO2'};
fem.descr = descr;

% Multiphysics
fem=multiphysics(fem);

% Extend mesh
fem.xmesh=meshextend(fem);

% Solve problem
fem.sol=femlin(fem, ...
                      'solcomp',{'Ez'}, ...
                      'outcomp',{'Ez'}, ...
                      'pname','lambda0_emwe', ...
                      'plist',[start:step:stop]);

% Save current fem structure for restart purposes
fem0=fem;
figure(1)
% Plot solution
postplot(fem, ...
             'tridata',{'Ez','cont','internal'}, ...
             'trimap','jet(1024)', ...
```

```
            'solnum','end',   ...                                                    118
            ' title ','lambda0_emwe(25)=6e-7    Surface: Electric field, z component [V/m]' ...
            ' refine ',3,   ...                                                      120
            'axis',[-6.750000E-8,1.417500E-6,-3.970153E-7,4.970153E-7,-1,1]);        121
                                                                                     122
                                                                                     123
figure(2)                                                                            124
% Plot in cross-section or along domain                                             125
postcrossplot(fem,0,[37],   ...                                                      126
              'pointdata','S21dB_emwe', ...                                          127
              ' title ','S-parameter dB (S21)', ...                                  128
              ' axislabel ',{'lambda0_emwe','S-parameter dB (S21)'}, ...             129
              ' refine ',3);                                                         130
                                                                                     131
% [transmission] = aquire(start,step,stop)                                          132
                                                                                     133
en=(stop-start)/step;                                                                134
for j=1:en                                                                           135
I1=postint(fem,'S21dB_emwe', ...                                                     136
           'dl',[37],   ...                                                          137
           'edim',0,   ...                                                           138
           'solnum',j);                                                              139
                                                                                     140
    transmission(j,:)=[start+j*step;real(I1)];                                       141
end                                                                                  142
```

A.4 Copyright Statement

A.5 Acknowledgments

I would like to thank the Institute for Advanced Studies (IAS) and the International Graduate School for Science and Engineering (IGSSE) for the PhD scholarship that i was granted. Their financial support made this work possible.
Prof. Paolo Lugli for the possibility to study at the Institute for Nanolectronics at this interesting and inspiring topic, for his support, for his time for discussions and for his help for my stay abroad.
Dr. Guiseppe Scarpa for his inspiring talent and support for interdisciplinary training.
Dr. Bernhard Fabel for his inspiration, discussions and support for being a great help maintaining the lab.
Morten Schmidt, Rosi Heilman und Rosi Mittermeier for being a good team member in maintaining the lab.
Prof. Bettina Lotsch for extensive discussions and a fruitful collaboration.
Ida Pavlichenko for her tireless work on paper writing and correction and for a fruitful collaboration.
The students who supported this work: Stefan Menacher, Gerald Derondeau and Alena Folger, Peter Zehetmaier and Katalin Szendrei
The proofreaders of this work: Annka Liepold, Erich Wehrle, Henning Exner and Laura Hustwick.
Rita von Grafenstein and Lucia Weik for a good atmosphere. Former and current institute members for a good time: Tobi, Alex, Mario, Daniela, Alaa, Morten, Atyab, Anandi, Francesco, Ahmed, Katharina, Robin, Florin, Edgar, Alpar, Dan, Bodgan and many more.
My family and friends for their motivation and for making the past three years a fantastic good time.

Meiner lieben Mutter

Bibliography

[Abd11] A. Abdellah, A. Yaqub, C. Ferrari, B. Fabel, P. Lugli and G. Scarpa. *Spray deposition of highly uniform CNT films and their application in gas sensing*. In *2011 11th IEEE International Conference on Nanotechnology*, pages 1118–1123, (IEEE2011). ISBN 978-1-4577-1516-7. ISSN 1944-9399. doi: 10.1109/NANO.2011.6144569.

[Abd12] A. Abdellah. *Scalable Thin-Film Manufacturing Technologies for Organic Electronics*. Phd thesis, Technische Universität München, 2012.

[Acc96] J. S. Accetta, D. L. Shumaker and M. C. Dudzik. *The Infrared and Electro-optical Systems Handbook: Electro-optical systems design, analysis, and testing, Volume 4*, (Environmental research institute of Michigan1996).

[Agu06] C. M. Aguirre, S. Auvray, S. Pigeon, R. Izquierdo, P. Desjardins and R. Martel. *Carbon nanotube sheets as electrodes in organic light-emitting diodes*. Applied Physics Letters, **volume 88**(18):183104, 2006. ISSN 00036951. doi: 10.1063/1.2199461.

[Ale12] D. Alemu, H.-Y. Wei, K.-C. Ho and C.-W. Chu. *Highly conductive PEDOT:PSS electrode by simple film treatment with methanol for ITO-free polymer solar cells*. Energy & Environmental Science, **volume 5**(11):9662, 2012. ISSN 1754-5692. doi: 10.1039/c2ee22595f.

[Ars05] A. C. Arsenault, V. Kitaev, I. Manners, G. A. Ozin, A. Mihi and H. Míguez. *Vapor swellable colloidal photonic crystals with pressure tunability*. Journal of Materials Chemistry, **volume 15**(1):133, 2005. ISSN 0959-9428. doi: 10.1039/b410284n.

[Ars11] A. Arsenault, G. A. Ozin and D. P. Puzzo. *Patent US20110164308 - Tunable Bragg Stack*, 2011.

[Azi98] H. Aziz, Z. Popovic, C. P. Tripp, N.-X. Hu, A.-M. Hor and G. Xu. *Degradation processes at the cathode/organic interface in organic light emitting devices with Mg:Ag cathodes.* Applied Physics Letters, **volume 72**(21):2642, 1998. ISSN 00036951. doi: 10.1063/1.121442.

[Bai11a] D. Baierl, B. Fabel, P. Lugli and G. Scarpa. *Efficient indium-tin-oxide (ITO) free top-absorbing organic photodetector with highly transparent polymer top electrode.* Organic Electronics, **volume 12**(10):1669–1673, 2011. ISSN 15661199. doi: 10.1016/j.orgel.2011.06.021.

[Bai11b] D. Baierl, M. Schmidt, G. Scarpa, L. Pancheri, D. Stoppa, G.-f. D. Betta and U. Trento. *Towards a hybrid CMOS-imager with organic semiconductors as photoactive layer.* Organic Electronics, **volume 12**:89–92, 2011.

[Bai12a] D. Baierl. *A Hybrid CMOS-Imager with Integrated Solution-Processable Organic Photodiodes.* Phd thesis, Technische Universität München, 2012.

[Bai12b] D. Baierl, L. Pancheri, M. Schmidt, D. Stoppa, G.-F. Dalla Betta, G. Scarpa and P. Lugli. *A hybrid CMOS-imager with a solution-processable polymer as photoactive layer.* Nature Communications, **volume 3**:1175, 2012. ISSN 2041-1723. doi: 10.1038/ncomms2180.

[Baj10] M. Bajpai, K. Kumari, R. Srivastava, M. Kamalasanan, R. Tiwari and S. Chand. *Electric field and temperature dependence of hole mobility in electroluminescent PDY 132 polymer thin films.* Solid State Communications, **volume 150**(13-14):581–584, 2010. ISSN 00381098. doi: 10.1016/j.ssc.2010.01.001.

[Ban09] A. Banerjee. *Enhanced Temperature Sensing by Using one-Dimensional Ternary Photonic Band Gap Structures.* Progress In Electromagnetics Research Letters, **volume 11**:129–137, 2009. ISSN 1937-6480. doi: 10.2528/PIERL09080101.

[Bao99] Z. Bao, J. Rogers, A. Dodabalapur, A. Lovinger, H. Katz, V. Raju, Z. Peng and M. Galvin. *Polymer light emitting diodes: new materials and devices*. Optical Materials, **volume 12**(2-3):177–182, 1999. ISSN 09253467. doi: 10.1016/S0925-3467(99)00050-6.

[Bäs93] H. Bässler. *Charge Transport in Disordered Organic Photoconductors a Monte Carlo Simulation Study*. physica status solidi (b), **volume 175**(1):15–56, 1993. ISSN 03701972. doi: 10.1002/pssb.2221750102.

[Bäs11] H. Bässler and A. Köhler. *Charge Transport in Organic Semiconductors*. Topics in current chemistry, pages 926–952, 2011. ISSN 0340-1022. doi: 10.1007/128“¨2011“¨218.

[Bec07] E. B. Bechtold, Tamara, Korvink, Jan G., Rudnyi. *Fast simulation of electro-thermal MEMS: efficient dynamic compact models*. In *Fast Simulation of Electro-Thermal MEMS: Efficient Dynamic Compact Models*, pages 65–67, (Springer2007). ISBN 3540346120.

[Ber55] A. Bernanose. *Electroluminescence of organic compounds*. British Journal of Applied Physics, **volume 6**(S4):S54–S55, 1955. ISSN 0508-3443. doi: 10.1088/0508-3443/6/S4/319.

[Ber98] Y. Beregovski, O. Hennig, M. Fallahi, F. Guzman, R. Clemens, S. Mendes and N. Peyghambarian. *Design and characteristics of DBR-laser-based environmental sensors*. Sensors and Actuators B: Chemical, **volume 53**(1-2):116–124, 1998. ISSN 09254005. doi: 10.1016/S0925-4005(98)00301-3.

[Bon09] L. D. Bonifacio, B. V. Lotsch, D. P. Puzzo, F. Scotognella and G. A. Ozin. *Stacking the Nanochemistry Deck: Structural and Compositional Diversity in One-Dimensional Photonic Crystals*. Advanced Materials, **volume 21**(16):1641–1646, 2009. ISSN 09359648. doi: 10.1002/adma.200802348.

[Bur90] J. H. Burroughes, D. D. C. Bradley, A. R. Brown, R. N. Marks, K. Mackay, R. H. Friend, P. L. Burns and A. B. Holmes. *Light-emitting diodes based on conjugated polymers*. Nature, **volume 347**(6293):539–541, 1990. ISSN 0028-0836. doi: 10.1038/347539a0.

[Bur11] I. B. Burgess, L. Mishchenko, B. D. Hatton, M. Kolle, M. Lončar and J. Aizenberg. *Encoding complex wettability patterns in chemically functionalized 3D photonic crystals.* Journal of the American Chemical Society, **volume 133**(32):12430–2, 2011. ISSN 1520-5126. doi: 10.1021/ja2053013.

[Bur12] I. B. Burgess, N. Koay, K. P. Raymond, M. Kolle, M. Lončar and J. Aizenberg. *Wetting in color: colorimetric differentiation of organic liquids with high selectivity.* ACS nano, **volume 6**(2):1427–37, 2012. ISSN 1936-086X. doi: 10.1021/nn204220c.

[Cal08] M. E. Calvo, S. Colodrero, T. C. Rojas, J. A. Anta, M. Ocaña and H. Míguez. *Photoconducting Bragg Mirrors based on TiO2 Nanoparticle Multilayers.* Advanced Functional Materials, **volume 18**(18):2708–2715, 2008. ISSN 1616301X. doi: 10.1002/adfm.200800039.

[Cal11] M. E. Calvo, S. Colodrero, N. Hidalgo, G. Lozano, C. López-López, O. Sánchez-Sobrado and H. Míguez. *Porous one dimensional photonic crystals: novel multifunctional materials for environmental and energy applications.* Energy & Environmental Science, **volume 4**(12):4800, 2011. ISSN 1754-5692. doi: 10.1039/c1ee02081a.

[Che99] K. M. Chen, A. W. Sparks, H.-C. Luan, D. R. Lim, K. Wada and L. C. Kimerling. *SiO2/TiO2 omnidirectional reflector and microcavity resonator via the sol-gel method.* Applied Physics Letters, **volume 75**(24):3805, 1999. ISSN 00036951. doi: 10.1063/1.125462.

[Che01] C. Chen. *Characterizations of VO2-based uncooled microbolometer linear array.* Sensors and Actuators A: Physical, **volume 90**(3):212–214, 2001. ISSN 09244247. doi: 10.1016/S0924-4247(01)00495-2.

[Che08] P.-C. Chen, G. Shen and C. Zhou. *Chemical Sensors and Electronic Noses Based on 1-D Metal Oxide Nanostructures.* IEEE Transactions on Nanotechnology, **volume 7**(6):668–682, 2008. ISSN 1536-125X. doi: 10.1109/TNANO.2008.2006273.

[Chi10] Y.-M. Chien, F. Lefevre, I. Shih and R. Izquierdo. *A solution processed top emission OLED with transparent carbon nanotube electrodes.* Nanotechnology, **volume 21**(13):134020, 2010. ISSN 1361-6528. doi: 10.1088/0957-4484/21/13/134020.

[Cho00] E. Chow, S. Y. Lin, S. G. Johnson, P. R. Villeneuve, J. D. Joannopoulos, J. R. Wendt, G. A. Vawter, W. Zubrzycki, H. Hou and A. Alleman. *Three-dimensional control of light in a two-dimensional photonic crystal slab.* Nature, **volume 407**(6807):983–6, 2000. ISSN 0028-0836. doi: 10.1038/35039583.

[Cho06] S. Y. Choi, M. Mamak, G. von Freymann, N. Chopra and G. A. Ozin. *Mesoporous bragg stack color tunable sensors.* Nano Letters, **volume 6**(11):2456–61, 2006. ISSN 1530-6984. doi: 10.1021/nl061580m.

[Cho11] S. Choi, S.-J. Kim, C. Fuentes-Hernandez and B. Kippelen. *ITO-free large-area organic light-emitting diodes with an integrated metal grid.* Optics Express, **volume 19**(S4):A793, 2011. ISSN 1094-4087. doi: 10.1364/OE.19.00A793.

[Cle13] Clevios (TM). *http://clevios.com*, 2013.

[Col01] V. L. Colvin. *From Opals to Optics: Colloidal Photonic Crystals.* MRS Bulletin, **volume 26**(08):637–641, 2001. ISSN 1938-1425.

[Col08] S. Colodrero, M. Ocaña and H. Míguez. *Nanoparticle-based one-dimensional photonic crystals.* Langmuir, **volume 24**(9):4430–4, 2008. ISSN 0743-7463. doi: 10.1021/la703987r.

[COM06] COMSOL Multiphysics 3.2. *http://www.comsol.com/*, 2006.

[Dem10] A. Demessence, C. Boissière, D. Grosso, P. Horcajada, C. Serre, G. Férey, G. J. A. A. Soler-Illia and C. Sanchez. *Adsorption properties in high optical quality nanoZIF-8 thin films with tunable thickness.* Journal of Materials Chemistry, **volume 20**(36):7676, 2010. ISSN 0959-9428. doi: 10.1039/c0jm00500b.

[Der96] E. L. Dereniak and G. D. Boreman. *Infrared detectors and systems*, (Wiley1996). ISBN 0471122092.

[Dod97] A. Dodabalapur. *Organic light emitting diodes*. Solid State Communications, **volume 102**(2-3):259–267, 1997. ISSN 00381098. doi: 10.1016/S0038-1098(96)00714-4.

[Dri99] R. G. Driggers. *Laboratory measurement of sampled infrared imaging system performance*. Optical Engineering, **volume 38**(5):852, 1999. ISSN 0091-3286. doi: 10.1117/1.602249.

[El 00] Z. El Mandouh. *Physical properties of vanadium pentoxide sol gel films*. Thin Solid Films, **volume 371**(1-2):259–263, 2000. ISSN 00406090. doi: 10.1016/S0040-6090(00)01003-8.

[Emm75] R. B. Emmons, S. R. Hawkins and K. F. Cuff. *Infrared Detectors: An Overview*. Optical Engineering, **volume 14**(1):21–30, 1975. ISSN 0277-786X.

[Exn13] A. T. Exner, I. Pavlichenko, B. V. Lotsch, G. Scarpa and P. Lugli. *Low-Cost Thermo-Optic Imaging Sensors: A Detection Principle Based on Tunable One-Dimensional Photonic Crystals*. ACS Applied Materials & Interfaces, **volume 5**(5):1575–1582, 2013. ISSN 1944-8252. doi: 10.1021/am301964y.

[FLU13] FLUIDAT. *http://www.fluidat.com/*, 2013.

[Fri99] R. H. Friend, R. W. Gymer, A. B. Holmes, J. H. Burroughes, R. N. Marks, C. Taliani, D. D. C. Bradley, D. A. D. Santos, J. L. Bredas, M. Logdlund et al. *Electroluminescence in conjugated polymers*. Nature, **volume 397**(6715):121–128, 1999. ISSN 0028-0836. doi: 10.1038/16393.

[Fue07] M. C. Fuertes, F. J. López-Alcaraz, M. C. Marchi, H. E. Troiani, V. Luca, H. Míguez and G. J. A. A. Soler-Illia. *Photonic Crystals from Ordered Mesoporous Thin-Film Functional Building Blocks*. Advanced Functional Materials, **volume 17**(8):1247–1254, 2007. ISSN 1616301X. doi: 10.1002/adfm.200601190.

[Fue08] M. Fuertes, S. Colodrero, G. Lozano, A. Gonzalez-Elipe, D. Grosso, C. Boissiere, C. Sanchez, G. Soler-Illia and H. Miguez. *Sorption Properties of Mesoporous Multilayer Thin Films*. Journal of Physical Chemistry C, **volume 112**(9):3157–3163, 2008. ISSN 1932-7447. doi: 10.1021/jp710612y.

[Ge07] J. Ge, Y. Hu and Y. Yin. *Highly Tunable Superparamagnetic Colloidal Photonic Crystals*. Angewandte Chemie, **volume 119**(39):7572–7575, 2007. ISSN 00448249. doi: 10.1002/ange.200701992.

[Gho95] G. Ghosh. *Model for the thermo-optic coefficients of some standard optical glasses*. Journal of Non-Crystalline Solids, **volume 189**(1-2):191–196, 1995. ISSN 00223093. doi: 10.1016/0022-3093(95)00247-2.

[Gib83] D. Gibson and P. H. Lissberger. *Optical properties of narrow-band spectral filter coatings related to layer structure and preparation.* Applied Optics, **volume 22**(2):269–81, 1983. ISSN 0003-6935.

[Gon02] X. Gong, M. Robinson, J. Ostrowski, D. Moses, G. Bazan and A. Heeger. *High-Efficiency Polymer-Based Electrophosphorescent Devices*. Advanced Materials, **volume 14**(8):581–585, 2002. ISSN 09359648. doi: 10.1002/1521-4095(20020418)14:8¡581::AID-ADMA581¿3.0.CO;2-B.

[Gül02] G. Gülşen and M. Naci Inci. *Thermal optical properties of TiO2 films*. Optical Materials, **volume 18**(4):373–381, 2002. ISSN 09253467. doi: 10.1016/S0925-3467(01)00176-8.

[Hal99] M. Halim, J. N. G. Pillow, I. D. W. Samuel and P. L. Burn. *Conjugated Dendrimers for Light-Emitting Diodes: Effect of Generation*. Advanced Materials, **volume 11**(5):371–374, 1999. ISSN 0935-9648. doi: 10.1002/(SICI)1521-4095(199903)11:5¡371::AID-ADMA371¿3.0.CO;2-1.

[Han12] T.-H. Han, Y. Lee, M.-R. Choi, S.-H. Woo, S.-H. Bae, B. H. Hong, J.-H. Ahn and T.-W. Lee. *Extremely efficient flexible organic light-emitting diodes with modified graphene anode*. Nature Photonics, **volume 6**(2):105–110, 2012. ISSN 1749-4885. doi: 10.1038/nphoton.2011.318.

[Hin12] F. M. Hinterholzinger, A. Ranft, J. M. Feckl, B. Rühle, T. Bein and B. V. Lotsch. *One-dimensional metal-organic framework photonic crystals used as platforms for vapor sorption.* Journal of Materials Chemistry, **volume 22**(20):10356, 2012. ISSN 0959-9428. doi: 10.1039/c2jm15685g.

[Hoh03] D. Hohlfeld. *A thermally tunable, silicon-based optical filter.* Sensors and Actuators A: Physical, **volume 103**(1-2):93–99, 2003. ISSN 09244247. doi: 10.1016/S0924-4247(02)00320-5.

[Hoh04] D. Hohlfeld and H. Zappe. *An all-dielectric tunable optical filter based on the thermo-optic effect.* Journal of Optics A: Pure and Applied Optics, **volume 6**(6):504–511, 2004. ISSN 1464-4258. doi: 10.1088/1464-4258/6/6/002.

[Hon10] N. Hongsith and S. Choopun. *Enhancement of Ethanol Sensing Properties by Impregnating Platinum on Surface of ZnO Tetrapods.* IEEE Sensors Journal, **volume 10**(1):34–38, 2010. ISSN 1530-437X. doi: 10.1109/JSEN.2009.2035746.

[Hsi06] K. Hsiao, V. Chodavarapu, A. Titus and A. Cartwright. *Colorimetric porous photonic bandgap sensors with integrated CMOS color detectors.* IEEE Sensors Journal, **volume 6**(3):661–667, 2006. ISSN 1530-437X. doi: 10.1109/JSEN.2006.874021.

[Hu10] L. Hu, J. Li, J. Liu, G. Grüner and T. Marks. *Flexible organic light-emitting diodes with transparent carbon nanotube electrodes: problems and solutions.* Nanotechnology, **volume 21**(15):155202, 2010. ISSN 1361-6528. doi: 10.1088/0957-4484/21/15/155202.

[Hum08] C. J. Humphreys. *Solid-state lighting.* MRS Bulletin, **volume 33**(04):459–470, 2008.

[Ish00] T. Ishikawa, M. Ueno, Y. Nakaki, K. Endo, Y. Ohta, J. Nakanishi, Y. Kosasayama, H. Yagi, T. Sone and M. Kimata. *Performance of 320 x 240 uncooled IRFPA with SOI diode detectors.* Proceedings of SPIE, **volume 4130**(1):152–159, 2000. ISSN 0277786X. doi: 10.1117/12.409857.

[Jia00] X. Jiang, S. Liu, H. Ma and A. K.-Y. Jen. *High-performance blue light-emitting diode based on a binaphthyl-containing polyfluorene.* Applied Physics Letters, **volume 76**(14):1813, 2000. ISSN 00036951. doi: 10.1063/1.126174.

[Joa08] J. D. Joannopoulos. *Photonic Crystals: Molding The Flow Of Light*, (Princeton University Press2008), 2nd edition. ISBN 0691124566.

[Kal04] J. Kalinowski. *Organic Light-Emitting Diodes: Principles, Characteristics & Processes (Optical Science and Engineering)*, (CRC Press2004). ISBN 0824759478.

[Kan02] E.-S. Kang, T.-H. Lee and B.-S. Bae. *Measurement of the thermo-optic coefficients in sol-gel derived inorganic-organic hybrid material films.* Applied Physics Letters, **volume 81**(8):1438, 2002. ISSN 00036951. doi: 10.1063/1.1501448.

[Kel11] T. L. Kelly, A. Garcia Sega and M. J. Sailor. *Identification and quantification of organic vapors by time-resolved diffusion in stacked mesoporous photonic crystals.* Nano Letters, **volume 11**(8):3169–73, 2011. ISSN 1530-6992. doi: 10.1021/nl201385p.

[Kim99] S.-S. Kim, S.-Y. Choi, C.-G. Park and H.-W. Jin. *Transparent conductive ITO thin films through the sol-gel process using metal salts.* Thin Solid Films, **volume 347**(1-2):155–160, 1999. ISSN 00406090. doi: 10.1016/S0040-6090(98)01748-9.

[Kim12] E. Kim, S. Y. Kim, G. Jo, S. Kim and M. J. Park. *Colorimetric and Resistive Polymer Electrolyte Thin Films for Real-time Humidity Sensors.* ACS Applied Materials & Interfaces, **volume 4**(10):5179–87, 2012. ISSN 1944-8252. doi: 10.1021/am3011115.

[Kob09] J. Kobler, B. V. Lotsch, G. A. Ozin and T. Bein. *Vapor-sensitive bragg mirrors and optical isotherms from mesoporous nanoparticle suspensions.* ACS nano, **volume 3**(7):1669–76, 2009. ISSN 1936-086X. doi: 10.1021/nn800911c.

[Kra02] K. Krapels, R. Driggers, R. Vollmerhausen and C. Halford. *Minimum resolvable temperature difference (MRT): procedure improvements and dynamic MRT*. Infrared Physics & Technology, **volume 43**(1):17–31, 2002. ISSN 13504495. doi: 10.1016/S1350-4495(01)00115-3.

[Kru80] P. Kruse and R. Keyes. *Optical and Infrared Detectors - Topics in Applied Physics*. In *Optical and Infrared Detectors*, volume 19, pages 5–69, (Springer Berlin / Heidelberg1980). ISBN 978-3-540-10176-5. doi: 10.1007/3540101764“¨10.

[Kru01] P. W. Kruse. *Uncooled thermal imaging: arrays, systems, and applications*, (SPIE Press2001). ISBN 0819441228.

[Kus07] B. Kuswandi, Nuriman, J. Huskens and W. Verboom. *Optical sensing systems for microfluidic devices: a review*. Analytica chimica acta, **volume 601**(2):141–55, 2007. ISSN 1873-4324. doi: 10.1016/j.aca.2007.08.046.

[Lam01a] S. Lamansky, R. C. Kwong, M. Nugent, P. I. Djurovich and M. E. Thompson. *Molecularly doped polymer light emitting diodes utilizing phosphorescent Pt(II) and Ir(III) dopants*. Organic Electronics, **volume 2**(1):53–62, 2001. ISSN 15661199. doi: 10.1016/S1566-1199(01)00007-6.

[Lam01b] G. Lammel. *Microspectrometer based on a tunable optical filter of porous silicon*. Sensors and Actuators A: Physical, **volume 92**(1-3):52–59, 2001. ISSN 09244247. doi: 10.1016/S0924-4247(01)00539-8.

[Lav06] N. V. Lavrik, D. Grbovic, S. Rajic, P. G. Datskos, D. Forrai, E. Nelson, J. Devitt and B. McIntyre. *Uncooled infrared imaging using bimaterial microcantilever arrays*. Proceedings of SPIE, **volume 6206**(1):62061K, 2006. ISSN 0277786X. doi: 10.1117/12.666125.

[Lee99] S. T. Lee, Z. Q. Gao and L. S. Hung. *Metal diffusion from electrodes in organic light-emitting diodes*. Applied Physics Letters, **volume 75**(10):1404, 1999. ISSN 00036951. doi: 10.1063/1.124708.

[Lee06] D. Lee, M. F. Rubner and R. E. Cohen. *All-nanoparticle thin-film coatings.* Nano Letters, **volume 6**(10):2305–12, 2006. ISSN 1530-6984. doi: 10.1021/nl061776m.

[Li09] J. Li and D. Liu. *Dendrimers for organic light-emitting diodes.* Journal of Materials Chemistry, **volume 19**(41):7584, 2009. ISSN 0959-9428. doi: 10.1039/b901618j.

[Lop08] M. A. Lopez, J. C. Sanchez and M. Estrada. *Characterization of PEDOT:PSS dilutions for inkjet printing applied to OLED fabrication.* In *2008 7th International Caribbean Conference on Devices, Circuits and Systems*, pages 1–4, (IEEE2008). ISBN 978-1-4244-1956-2. doi: 10.1109/ICCDCS.2008.4542640.

[Lot08] B. V. Lotsch and G. A. Ozin. *Photonic clays: a new family of functional 1D photonic crystals.* ACS nano, **volume 2**(10):2065–74, 2008. ISSN 1936-086X. doi: 10.1021/nn800375e.

[Mac76] H. Macleod and D. Richmond. *Moisture penetration patterns in thin films.* Thin Solid Films, **volume 37**(2):163–169, 1976.

[Mac86] H. A. Macleod. *Thin-Film Optical Filters*, (IOP Publishing Ltd1986). ISBN 0750306882. doi: 10.1887/0750306882.

[Mei12] L. Mei, J. Deng, X. Yin, M. Zhang, Q. Li, E. Zhang, Z. Xu, L. Chen and T. Wang. *Ultrasensitive ethanol sensor based on 3D aloe-like SnO2.* Sensors and Actuators B: Chemical, **volume 166-167**(null):7–11, 2012. ISSN 09254005. doi: 10.1016/j.snb.2011.06.054.

[MF13] F. Maier-Flaig, J. Rinck, M. Stephan, T. Bocksrocker, M. Bruns, C. Kübel, A. K. Powell, G. A. Ozin and U. Lemmer. *Multicolor Silicon Light-Emitting Diodes (SiLEDs).* Nano Letters, **volume 13**(2):475–80, 2013. ISSN 1530-6992. doi: 10.1021/nl3038689.

[Moo02] E. Moons. *Conjugated polymer blends: linking film morphology to performance of light emitting diodes and photodiodes.* Journal of Physics:

Condensed Matter, **volume 14**(47):12235–12260, 2002. ISSN 0953-8984. doi: 10.1088/0953-8984/14/47/301.

[Mue06] K. Muellen and U. Scherf. *Organic Light Emitting Devices*, (Wiley-VCH2006).

[Mul13] S. Mulani, M. Xiao, S. Wang, Y. Chen, J. Peng and Y. Meng. *Structure properties of a highly luminescent yellow emitting material for OLED and its application*. RSC Advances, **volume 3**(1):215, 2013. ISSN 2046-2069. doi: 10.1039/c2ra21951d.

[Nai10] R. V. Nair and R. Vijaya. *Photonic crystal sensors: An overview*. Progress in Quantum Electronics, **volume 34**(3):89–134, 2010. ISSN 00796727. doi: 10.1016/j.pquantelec.2010.01.001.

[Naz10] Y. Nazirizadeh, U. Bog, S. Sekula, T. Mappes, U. Lemmer and M. Gerken. *Low-cost label-free biosensors using photonic crystals embedded between crossed polarizers*. Optics Express, **volume 18**(18):19120, 2010. ISSN 1094-4087. doi: 10.1364/OE.18.019120.

[Ngu03] T. Nguyen, P. Le Rendu, N. Dinh, M. Fourmigué and C. Mézière. *Thermal and chemical treatment of ITO substrates for improvement of OLED performance*. Synthetic Metals, **volume 138**(1-2):229–232, 2003. ISSN 03796779. doi: 10.1016/S0379-6779(02)01292-4.

[Nik01] F. Niklaus, E. Kälvesten and G. Stemme. *Wafer-level membrane transfer bonding of polycrystalline silicon bolometers for use in infrared focal plane arrays*. Journal of Micromechanics and Microengineering, **volume 11**(5):509, 2001. ISSN 0960-1317. doi: http://dx.doi.org/10.1088/0960-1317/11/5/310.

[Pav12a] I. Pavlichenko, A. T. Exner, M. Guehl, P. Lugli, G. Scarpa and B. V. Lotsch. *Humidity-Enhanced Thermally Tunable TiO2/SiO2 Bragg Stacks*. The Journal of Physical Chemistry C, **volume 116**(1):298–305, 2012. ISSN 1932-7447. doi: 10.1021/jp208733t.

[Pav12b] I. Pavlichenko, A. T. Exner, G. Logvenov, G. Scarpa, P. Lugli and B. V. Lotsch. *Nanomorphology tuning of the thermal response of TiO2/SiO2 Bragg stacks*. Canadian Journal of Chemistry, **volume 90**(12):1069–1077, 2012. ISSN 0008-4042. doi: 10.1139/v2012-081.

[Pav12c] I. Pavlichenko, A. T. Exner, P. Lugli, G. Scarpa and B. V. Lotsch. *Tunable thermoresponsive TiO2/SiO2 Bragg stacks based on sol-gel fabrication methods*. Journal of Intelligent Material Systems and Structures, 2012. ISSN 1045-389X. doi: 10.1177/1045389X12453970.

[Pel88] S. Pellicori and H. Hettich. *Reversible spectral shift in coatings*. Applied Optics, **volume 27**(15):3061–3062, 1988.

[Pfi77] G. Pfister. *Hopping transport in a molecularly doped organic polymer*. Physical Review B, **volume 16**(8):3676–3687, 1977. ISSN 0556-2805. doi: 10.1103/PhysRevB.16.3676.

[Pop63] M. Pope, H. P. Kallmann and P. Magnante. *Electroluminescence in Organic Crystals*. The Journal of Chemical Physics, **volume 38**(8):2042, 1963. ISSN 00219606. doi: 10.1063/1.1733929.

[Puz11] D. P. Puzzo, M. G. Helander, P. G. O'Brien, Z. Wang, N. Soheilnia, N. Kherani, Z. Lu and G. A. Ozin. *Organic light-emitting diode microcavities from transparent conducting metal oxide photonic crystals*. Nano Letters, **volume 11**(4):1457–1462, 2011. ISSN 1530-6992. doi: 10.1021/nl104036c.

[Qiu06] X. J. Qiu, X. W. Tan, Z. Wang, G. Y. Liu and Z. H. Xiong. *Tunable, narrow, and enhanced electroluminescent emission from porous-silicon-reflector-based organic microcavities*. Journal of Applied Physics, **volume 100**(7):074503, 2006. ISSN 00218979. doi: 10.1063/1.2355536.

[Ray12] K. P. Raymond, I. B. Burgess, M. H. Kinney, M. Lončar and J. Aizenberg. *Combinatorial wetting in colour: an optofluidic nose*. Lab on a chip, **volume 12**(19):3666–9, 2012. ISSN 1473-0189. doi: 10.1039/c2lc40489c.

[Reg08] P. Regoliosi, M. Guehl, G. Scarpa, P. Lugli, L. Persano, P. D. Carro, A. Camposeo, R. Cingolani, D. Pisignano, S. Bietti et al. *Thermal tunability of monolithic polymer microcavities*. Applied Physics Letters, **volume 92**(25):2008–2010, 2008. doi: 10.1063/1.2953069.

[Ren07] K. Ren, Z.-Y. Li, X. Ren, S. Feng, B. Cheng and D. Zhang. *Three-dimensional light focusing in inverse opal photonic crystals*. Physical Review B, **volume 75**(11):115108, 2007. ISSN 1098-0121. doi: 10.1103/PhysRevB.75.115108.

[Rog02] A. Rogalski. *Infrared detectors: an overview*. Infrared Physics & Technology, **volume 43**(3-5):187–210, 2002. ISSN 13504495. doi: 10.1016/S1350-4495(02)00140-8.

[Rog03] A. Rogalski. *Infrared detectors: status and trends*. Progress in Quantum Electronics, **volume 27**(2-3):59–210, 2003. ISSN 00796727. doi: 10.1016/S0079-6727(02)00024-1.

[Rog05] A. Rogalski. *HgCdTe infrared detector material: history, status and outlook*. Reports on Progress in Physics, **volume 68**(10):2267–2336, 2005. ISSN 0034-4885. doi: 10.1088/0034-4885/68/10/R01.

[Sas13] H. Sasabe and J. Kido. *Development of High Performance OLED for General Lighting*. Journal of Materials Chemistry C, 2013.

[Sax84] S. G. Saxe, M. J. Messerly, B. Bovard, L. Desandre, F. J. Van Milligen and H. a. Macleod. *Ion bombardment-induced retarded moisture adsorption in optical thin films*. Applied Optics, **volume 23**(20):3633, 1984. ISSN 0003-6935.

[Sca08] G. Scarpa, P. Lugli, P. Regoliosi, F. Clever, J. Michalski and S. Hirschsteiner. *Device for Imaging and Method for Producing the Device*, 2008.

[Sed98] S. Sedky, P. Fiorini, M. Caymax, A. Verbist and C. Baert. *IR bolometers made of polycrystalline silicon germanium*. Sensors and Actua-

tors A: Physical, **volume 66**(1-3):193–199, 1998. ISSN 09244247. doi: 10.1016/S0924-4247(98)00007-7.

[Shi03] J. Shinar. *Organic Light-Emitting Devices*, (Springer2003). ISBN 0387953434.

[Shi08a] J. Shi, V. K. Hsiao, T. R. Walker and T. J. Huang. *Humidity sensing based on nanoporous polymeric photonic crystals.* Sensors and Actuators B: Chemical, **volume 129**(1):391–396, 2008. ISSN 09254005. doi: 10.1016/j.snb.2007.08.037.

[Shi08b] J. Shinar and R. Shinar. *Organic light-emitting devices (OLEDs) and OLED-based chemical and biological sensors: an overview.* Journal of Physics D: Applied Physics, **volume 41**(13):133001, 2008. ISSN 0022-3727. doi: 10.1088/0022-3727/41/13/133001.

[Smi68] R. A. Smith. *Detection and Measurement of Infrared Radiation (Monographs on the Physics & Chemistry of Materials)*, (Oxford University Press1968). ISBN 0198513240.

[Smi01] E. P. G. Smith, K. J. Winchester, C. A. Musca, J. M. Dell and L. Faraone. *A simplified fabrication process for HgCdTe photoconductive detectors using CH 4 /H 2 reactive-ion-etching-induced blocking contacts.* Semiconductor Science and Technology, **volume 16**(6):455–462, 2001. ISSN 0268-1242. doi: 10.1088/0268-1242/16/6/306.

[SN10] A. H. Safavi-Naeini, T. P. M. Alegre, M. Winger and O. Painter. *Optomechanics in an ultrahigh-Q two-dimensional photonic crystal cavity.* Applied Physics Letters, **volume 97**(18):181106, 2010. ISSN 00036951. doi: 10.1063/1.3507288.

[Sno99] P. A. Snow, E. K. Squire, P. S. J. Russell and L. T. Canham. *Vapor sensing using the optical properties of porous silicon Bragg mirrors.* Journal of Applied Physics, **volume 86**(4):1781, 1999. ISSN 00218979. doi: 10.1063/1.370968.

[Su12] S.-J. Su, C. Cai, J. Takamatsu and J. Kido. *A host material with a small singlet-triplet exchange energy for phosphorescent organic light-emitting diodes: Guest, host, and exciplex emission.* Organic Electronics, **volume 13**(10):1937–1947, 2012. ISSN 15661199. doi: 10.1016/j.orgel.2012.06.009.

[Tia08] E. Tian, J. Wang, Y. Zheng, Y. Song, L. Jiang and D. Zhu. *Colorful humidity sensitive photonic crystal hydrogel.* Journal of Materials Chemistry, **volume 18**(10):1116, 2008. ISSN 0959-9428. doi: 10.1039/b717368g.

[Tsc06] C. Tschamber. *Ladungstransport in Organischen Leuchtdioden*, (Shaker; Auflage: 12006). ISBN 3832250182.

[Uma02] P. Umadevi. *Preparation and characterisation of transition metal oxide micro-thermistors and their application to immersed thermistor bolometer infrared detectors.* Sensors and Actuators A: Physical, **volume 96**(2-3):114–124, 2002. ISSN 09244247. doi: 10.1016/S0924-4247(01)00776-2.

[vF12] G. von Freymann, V. Kitaev, B. V. Lotsch and G. A. Ozin. *Bottom-up assembly of photonic crystals.* Chemical Society reviews, 2012. ISSN 1460-4744. doi: 10.1039/c2cs35309a.

[Wan11] R. Wang, D. Liu, H. Ren, T. Zhang, X. Wang and J. Li. *Homoleptic tris-cyclometalated iridium complexes with 2-phenylbenzothiazole ligands for highly efficient orange OLEDs.* Journal of Materials Chemistry, **volume 21**(39):15494, 2011. ISSN 0959-9428. doi: 10.1039/c1jm10757g.

[Wie09] S. Wiechmann and J. Müller. *Thermo-optic properties of TiO2, Ta2O5 and Al2O3 thin films for integrated optics on silicon.* Thin Solid Films, **volume 517**(24):6847–6849, 2009. ISSN 00406090. doi: 10.1016/j.tsf.2009.05.040.

[Wik13a] Wikipedia. *http://en.wikipedia.org/wiki/Conjugated_polymers*, 2013.

[Wik13b] Wikipedia. *http://en.wikipedia.org/wiki/Dendrimer*, 2013.

[Woo01] R. A. Wood, P. Capper, C. T. Elliott, A. F. W. Willoughby and R. Hull. *Infrared Detectors and Emitters: Materials and Devices*, (Springer US, Boston, MA2001). ISBN 978-0-7923-7206-6. doi: 10.1007/978-1-4615-1607-1.

[Wu07] Z. Wu, D. Lee, M. F. Rubner and R. E. Cohen. *Structural color in porous, superhydrophilic, and self-cleaning SiO2/TiO2 Bragg stacks.* Small (Weinheim an der Bergstrasse, Germany), **volume 3**(8):1445–51, 2007. ISSN 1613-6829. doi: 10.1002/smll.200700084.

[Wu10] J. Wu, M. Agrawal, H. a. Becerril, Z. Bao, Z. Liu, Y. Chen and P. Peumans. *Organic light-emitting diodes on solution-processed graphene transparent electrodes.* ACS nano, **volume 4**(1):43–8, 2010. ISSN 1936-086X. doi: 10.1021/nn900728d.

[Xie09] H. Xie, F. Ng and X. Zeng. *Spectroscopic ellipsometry study of thin film thermo-optical properties.* Thin Solid Films, **volume 517**(17):5066–5069, 2009. ISSN 00406090. doi: 10.1016/j.tsf.2009.03.159.

[Yam05] H. Yamamoto, J. Wilkinson, J. P. Long, K. Bussman, J. A. Christodoulides and Z. H. Kafafi. *Nanoscale organic light-emitting diodes.* Nano Letters, **volume 5**(12):2485–8, 2005. ISSN 1530-6984. doi: 10.1021/nl051811+.

[Yu05] K. Yu. *Characterization of MEMS optical bandpass filters with narrow transition bands.* Proceedings of SPIE, **volume 6021**:60212R, 2005. ISSN 0277786X. doi: 10.1117/12.637438.

[Zha06] Z. Zhang, P. Zhao, P. Lin and F. Sun. *Thermo-optic coefficients of polymers for optical waveguide applications.* Optical Engineering, **volume 47**:4893–4896, 2006. doi: 10.1016/j.polymer.2006.05.035.

[Zho06] L. Zhou, A. Wanga, S.-C. Wu, J. Sun, S. Park and T. N. Jackson. *All-organic active matrix flexible display.* Applied Physics Letters, **volume 88**(8):083502, 2006. ISSN 00036951. doi: 10.1063/1.2178213.

[Zho11] C. Zhong, C. Duan, F. Huang, H. Wu and Y. Cao. *Materials and Devices toward Fully Solution Processable Organic Light-Emitting Diodes*. Chemistry of Materials, **volume 23**(3):326–340, 2011. ISSN 0897-4756. doi: 10.1021/cm101937p.